Accuracy of High Order Density Based Compressible Methods in Low Mach Vortical Flows *

Sanjeev Shanmuganathan

Submitted for the Degree of Master of Science by Research

Department of Engineering Physics
School of Engineering
Cranfield University
Cranfield
Bedfordshire MK43 0AL
United Kingdom

2013

Accuracy of High Order Density Based Compressible Methods in Low Mach Vortical Flows *

Sanjeev Shanmuganathan

Supervisor:
Dr. Ben Thornber

This thesis is submitted in fulfilment of the requirements for the Degree of Master of Science by Research

in the

Department of Engineering Physics
School of Engineering
Cranfield University
Cranfield
Bedfordshire MK43 0AL
United Kingdom

2013

*Contains material © British Crown Copyright 2013/AWE

Abstract

A new, well posed, two-dimensional two-mode incompressible Kelvin–Helmholtz instability test case has been chosen to explore the ability of a compressible algorithm, Godunov-type scheme with the low Mach number correction, which can be used for simulations involving low Mach numbers, to capture the observed vortex pairing process due to the initial Kelvin–Helmholtz instability growth on low resolution grid. The order of accuracy, 2^{nd} and 5^{th}, of the compressible algorithm is also highlighted.

The observed vortex pairing results and the corresponding momentum thickness of the mixing layer against time are compared with results obtained using the same compressible algorithm but without the low Mach number correction and three other methods, a Lagrange remap method where the Lagrange phase is 2^{nd} order accurate in space and time while the remap phase is 3^{rd} order accurate in space and 2^{nd} order accurate in time, a 5^{th} order accurate in space and time finite difference type method based on the wave propagation algorithm and a 5^{th} order spatial and 3^{rd} order temporal accurate Godunov method utilising the SLAU numerical flux with low Mach capture property.

The ability of the compressible flow solver of the commercial software, ANSYS Fluent, in solving low Mach flows is also examined for both implicit and explicit methods provided in the compressible flow solver.

In the present two dimensional two mode incompressible Kelvin–Helmholtz instability test case, the flow conditions, stream velocities, length-scales and Reynolds numbers, are taken from an experiment conducted on the observation of vortex pairing process. Three different values of low Mach numbers, 0.2, 0.02 and 0.002 have been tested on grid resolutions of 24×24, 32×32, 48×48 and 64×64 on all the different numerical approaches.

The results obtained show the vortex pairing process can be captured on a low grid resolution with the low Mach number correction applied down to 0.002 with 2^{nd} and 5^{th} order Godunov-type methods. Results also demonstrate clearly that a specifically designed low Mach correction or flux is required for all algorithms except the Lagrange-remap approach, where dissipation is independent of Mach number. ANSYS Fluent's compressible flow solver with the implicit time stepping method also captures the vortex pairing on low resolutions but excessive dissipation prevents the instability growth when explicit time stepping method is applied.

Acknowledgements

It would not have been possible to write this thesis without the help and support of the kind people around me, to only some of whom it is possible to give particular mention here.

Foremost, I would like to express my sincere gratitude to my supervisor, Dr Ben Thornber, for his continuous support of my research, for his patience, motivation, valued guidance, enthusiasm, and immense knowledge. His guidance helped me throughout the whole time of my research and writing of this thesis. I could not have imagined having a better mentor for my research.

Besides my mentor, I would like to thank the rest of my thesis committee: Prof. David Youngs and Dr. Robin Williams at AWE (UK), for their encouragement, insightful comments and hard questions and also like to acknowledge the financial support of the project from AWE (UK).

In my office I was surrounded by knowledgable and friendly people. My office colleague and friend, Mike Probyn has been a great source of practical information and is someone who has helped and supported me throughout the year. Also my journey to Cranfield and back can be a long haul however whenever Mike joined me our chats made my journey feel shorter which meant a lot as I did this day in and out. I would also like to thank Pierre-Daniel Jameson for his humor. Pierre and Mike kept my long days entertained. I would like to thank Nurhana Rouyan for her delicious Malaysian food. I also take great pleasure in thanking the people whom I shared my time with at Cranfield University, Rukshan Navaratne, Jeremy Appleyard, and Hairol Ali.

Last but not least, I would like to express my deepest gratitude to my wife Gaayatiri, for her patience and support and also my cute newborn little daughter, Sahana Ollivia. Additionally, I would like to thank my aunts, Radha, Surenthiramany and Sulosana and my sister, Kavitha for their role in encouraging and supporting me.

A special thank you to Dr. Jérôme Griffond at CEA (France) for agreeing to be the co-author of my journal paper and also for providing me with his simulation results to be used in this thesis. I would also like to acknowledge the assistance of Dr. Laszlo Konozsy in writing the UDFs for the ANSYS Fluent initialisation.

I would like to dedicate this thesis and present my sincere thankfulness to my deceased father, Shanmuganathan, who passed away during the writing of this thesis, for his great role in my life and the numerous sacrifices he has made for me. He has taught me so much and was my idol growing up.

Sanjeev Shanmuganathan,
March 5, 2012

Contents

List of Figures

List of Tables

Nomenclature

$\bar{U}$	Mean stream velocity
ΔU	Difference of the upper and lower streams
μ	fluid viscosity
ψ	Stream function
ρ	density
Θ	Momentum thickness
A_i	Amplitude
k_1 and k_2	Wave numbers
L	length
u' and v'	Velocity perturbations
U_1	Upper stream velocity
U_2	Lower stream velocity
V_1 and V_2	Velocity amplitudes
`CHOC`	Compressible High-Order Combustion
AUSM	Advection Upstream Splitting Method
CFD	Computational Fluid Dynamics
CFL	Courant–Friedrichs–Lewy
DNS	Direct Numerical Simulation
FVM	Finite Volume Method
HLL	Harten Lax and van Leer
HLLC	Harten Lax and van Leer–Contact
HLLE	Harten, Lax, van Leer and Einfeldt
HLLEM	Harten, Lax, van Leer and Einfeldt Modified
KH	Kelvin–Helmholtz
LES	Large Eddy Simulation
LMC	low Mach Correction

M	Mach number
RANS	Reynolds-Averaged Navier–Stokes
Re	Reynolds number
SGS	Sub Grid Scale
SLAU	Simple low-dissipation AUSM
TKE	Turbulent Kinetic Energy

Chapter 1

Introduction

1.1 Aims and Objectives

In computational fluid dynamics, compressible flow solvers are being used in simulations of incompressible flow test cases. So the question which arises immediately is: What is the importance of computing an incompressible flow test case using a compressible algorithm? One of the main reasons is that in low speed aerodynamics, at high angle of attacks, the domain has both compressible and incompressible flow regions. Incompressible flow consists of low Mach numbers and various articles written in the field of fluid dynamics show the incompressible equations are an approximation of the compressible flow equations.

Simulation of incompressible flows at low Mach numbers using compressible algorithms leads to three well known problems: poor accuracy; stiffness and cancellation. So in order to satisfy the use of compressible flow equations to compute low Mach flows specially designed low Mach capture techniques should be proposed and demonstrated.

A two-dimensional, two mode incompressible Kelvin–Helmholtz instability test case is used to demonstrate that Godunov methods suffer from severe dissipation at lower Mach numbers. This test case is well-posed, consisting of a smooth initial condition, regularised by viscosity, and thus the solution converges with grid refinement.

In the present Kelvin–Helmholtz instability test case, the flow conditions, stream velocities, length-scales and Reynolds numbers, are taken from the experiment by Winant and Browand [4]. The aim of this project is to calculate the evolution of some of the observed large-scale vortical structures for low Mach number flows, an incompressible two-dimensional two-mode Kelvin–Helmholtz instability test case, on a compressible algorithm, 2^{nd} and 5^{th} order accurate in space Godunov scheme with and without the low Mach number correction.

The objective is to explore the ability of compressible methods implemented to resolve vortical structures at high wavenumbers through highly under resolved simulations of the two-dimensional Kelvin–Helmholtz instability growth problem. The Kelvin–Helmholtz instability test case is two-dimensional hence straightforward to compute, and serves to clearly highlight the influence of order of accuracy and choice of method. Coarse grid resolutions are very important, as these are direct representations of the ability of the algorithms to capture vortex development at high wavenumbers in a highly resolved Large-Eddy-Simulation (LES). Furthermore, several compressible turbulent mixing applications require resolution of shocks and vortices simultaneously which motivates the focus on compressible algorithms here.

ANSYS Fluent results obtained for the Kelvin–Helmholtz instability growth test case act as a universally available accessible reference to compare the schemes performance in capturing the Kelvin–Helmholtz instability growth at low Mach number.

1.2 Structure of the Thesis

The thesis starts with the literature review where the vortex pairing process experiment and the Kelvin–Helmholtz instability theory are explained. Numerical studies and experiments carried out in the past on turbulent mixing and vortical structures are also discussed. The scientific challenges in simulating low Mach flows are highlighted. Chapter 2 gives an overview of turbulence and modelling of turbulence, Reynolds-Averaged Navier–Stokes, Direct Numerical Simulation and Large Eddy Simulation.

Chapter 3 contains the governing equations employed and details the numerical methods, Godunov approach with the low Mach correction, Lagrange-remap method, wave propagation algorithm, Godunov method with SLAU numerical flux and commercial software, ANSYS Fluent, used in obtaining the instability growth results. A full description of the initial conditions and boundary conditions for the test case are included in Chapter 5.

The results, observed vortex pairing and momentum thickness against time, are presented in Chapter 6. Finally, the scheme performance of the numerical methods in vortical flows is concluded in Chapter 7.

1.3 Journal Publication

The following paper has been submitted and is currently under review:

Sanjeev Shanmuganathan (Cranfield University, UK), David L. Youngs (AWE, UK), Jérôme Griffond (CEA, France), Ben Thornber (University of Sydney, Australia) and Robin J. R. Williams (AWE, UK). *'Accuracy of high order density based compressible methods in low Mach vortical flows'*, submitted to International Journal for Numerical Methods in Fluids, 2013

Chapter 2

Turbulence

2.1 Introduction to Turbulence

Most environmental fluid flows are turbulent. Turbulent flows occur around us every day and some simple examples are smoke rising from a cigarette and a water tap running at different flow velocities. Figure 2.1 illustrates the turbulent flow clearly and from visualising the same figure, it is clear that initially the smoke starts from the cigarette as a laminar flow for a certain distance and it develops into a turbulent flow and mixing with the surrounding air rapidly. This increase in mixing is a key feature of turbulent mixing.

The other example of turbulent flow, a water tap running at different flow velocities, is shown in figure 2.2. It shows two identical taps dispensing water at different flow velocities. When the water is allowed to flow slowly by opening the tap a little the surface of the jet is smooth and the flow is laminar but as the tap is fully turned on the flow becomes turbulent. In this example the flow turns turbulent when the velocity of the flow increases.

In the two previous examples the flow starts as laminar and turns into turbulent. In another words the flow is changing from an orderly pattern to a chaotic behaviour and this change of character takes place when the flow goes through a zone called transition. But in these two examples of turbulent flows, in one case the flow turns turbulent when the distance increased from the origin of the flow while in the other case increase in the flow velocity played a part to turn the flow turbulent.

The relationship between these two parameters, distance and velocity, which changed the laminar flow into turbulent is given by the Reynolds number as,

$$Re = \frac{\rho U L}{\mu} \tag{2.1}$$

Equation 2.1 shows velocity and distance are directly proportional to the Reynolds number. So one can come to the conclusion that as the Reynolds number increases the flow transitions to turbulent. The flow remains laminar at low Reynolds number and as the Reynolds number increases the flow turns into turbulent. As the flow becomes turbulent the state of motion becomes random and chaotic. In this state of motion changes to the velocity and pressure become continuously varying with time [15].

Figure 2.1: Smoke rising from a cigarette [1]

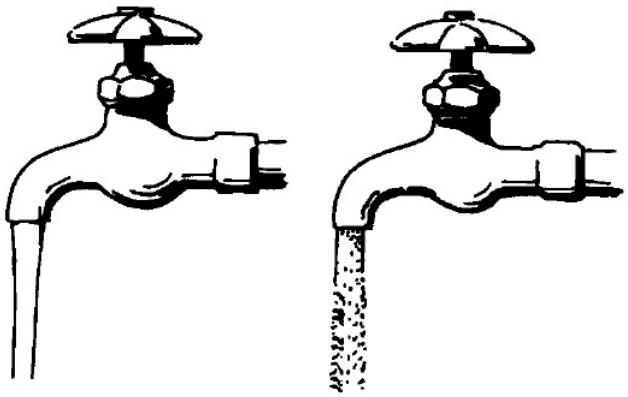

(a) Laminar flow **(b)** Turbulent flow

Figure 2.2: Water flowing from a tap [2]

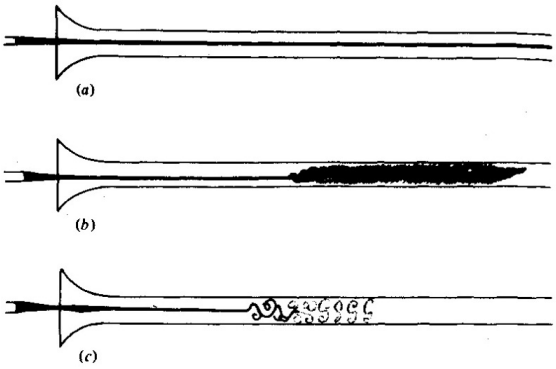

Figure 2.3: Experiment conducted by Osborne Reynolds to demonstrate the transition of laminar to turbulent flow (a) laminar flow (b) turbulent flow (c) turbulent flow observed with an electric spark [3]

The increase in Reynolds number which results in the transition to turbulence in fluid flows was first demonstrated by Osborne Reynolds by an experiment. During the experiment dye was injected into the pipe where the water flowed due to gravity. Figure 2.3 shows at low velocities the streak of dye extended in a straight line along the pipe. Increasing the velocity of the water resulted in the dye mixing with the surrounding water at some point in the pipe.

Fluid move downstream in smooth and regular trajectories in a laminar flow. During this laminar flow there is very little mixing between different layers of fluid. In such a laminar flow each of the fluid particles passes a given certain point in space with exactly the same speed and follows the same flow direction. If honey is poured from a jar it will remain laminar and it is difficult to make it turbulent as the strong viscous force damps out the irregularities in the flow. The high viscosity of honey means honey is typically in a low Reynolds number state [16].

2.2 Turbulence Modelling

A flow of eddies with a wide range of length and time scales appear in the turbulent flow and they act together in a dynamically complex way. In engineering applications it is highly important whether to avoid or promote the turbulent flow. In order to capture the important turbulent effects, numerical methods have been developed with an extensive amount of research work. The following three sections show how these numerical methods are grouped into types.

2.2.1 Reynolds-Averaged Navier–Stokes

The Reynolds-Averaged Navier–Stokes (RANS) approach is used to model the time or ensemble averaged effect of turbulent fluctuations with the computational cost in mind. Using RANS is the least expensive method when it comes to turbulence modelling. A designer is not concerned with a particular eddy in most applications but only with their average effect. So in RANS modelling the concentration is only on mean flow and the effects of turbulence on the mean flow properties. In this method the Navier–Stokes equations are time or ensemble averaged before the application of numerical methods. During the time averaging process extra terms appear in the flow equations. The interaction between various turbulent fluctuations is the reason behind the

appearance of these extra terms and they are modelled with using classical turbulence models such as $k-\epsilon$ and Reynolds stress model [15].

The incompressible continuity equation in 2D is,

$$\frac{\partial u}{\partial x}+\frac{\partial v}{\partial y}=0 \tag{2.2}$$

$$u=\bar{u}+u' \tag{2.3}$$

$$v=\bar{v}+v' \tag{2.4}$$

By time averaging the continuity equation becomes,

$$\frac{\partial \bar{u}}{\partial x}+\frac{\partial \bar{v}}{\partial y}=0 \tag{2.5}$$

The incompressible momentum equations in 2D are,

$$\rho\left(\frac{\partial u}{\partial t}+u\frac{\partial u}{\partial x}+v\frac{\partial u}{\partial y}\right)=-\frac{\partial p}{\partial x}+\mu\left(\frac{\partial^2 u}{\partial x^2}+\frac{\partial^2 u}{\partial y^2}\right) \tag{2.6}$$

$$\rho\left(\frac{\partial v}{\partial t}+u\frac{\partial v}{\partial x}+v\frac{\partial v}{\partial y}\right)=-\frac{\partial p}{\partial y}+\mu\left(\frac{\partial^2 v}{\partial x^2}+\frac{\partial^2 v}{\partial y^2}\right) \tag{2.7}$$

By time averaging the momentum equation the Reynolds average equation of momentum becomes,

$$\rho\left(\frac{\partial \bar{u}}{\partial t}+u\frac{\partial \bar{u}}{\partial x}+v\frac{\partial \bar{u}}{\partial y}\right)=-\frac{\partial p}{\partial x}+\mu\left(\frac{\partial^2 \bar{u}}{\partial x^2}+\frac{\partial^2 \bar{u}}{\partial y^2}\right)-\frac{\partial(u'v')}{\partial y}-\frac{\partial u'^2}{\partial x^2} \tag{2.8}$$

In the above equation, additional Reynolds stresses have appeared after the Reynolds averaging process. The Reynolds stresses are the averaged dissipative effect of the turbulent fluctuations and cannot be resolved. The dissipative effect of the Reynolds stresses are not due to viscosity but produced by the exchange of momentum due to turbulent mixing. This is called the closure problem because one cannot close the RANS system of equations and the Reynolds stresses need to be modelled using realistic models. In order to predict these Reynolds stresses and scalar transport terms, turbulence models have to be developed so the turbulent flows can be computed. The RANS turbulence models depend on the number of extra transport equations, given in table 2.1, which need to be solved beside the RANS flow equations.

Table 2.1: RANS turbulence models [15]

Number of extra transport equations	*Name of the turbulence model*
Zero	Mixing length model
One	Spalart–Allmaras model
Two	$k-\epsilon$ model $k-\omega$ model Algebraic stress model
Seven	Reynolds stress model

2.2.2 Direct Numerical Simulation (DNS)

Direct Numerical Simulation (DNS) is solving the full Navier–Stokes equations numerically, resolving all the scales of motion, without the use of any turbulence models. All scales are resolved both spatially and temporally. Even the smallest turbulent eddies and fastest fluctuations are solved by using a fine spatial mesh with small time steps [15].

Spectral methods based on Fourier series decomposition in periodic directions and Chebyshev polynomial expansions in directions with solid walls, were used in the first DNS [15]. Although these methods are economical and have a high convergence rate, applying this to complex geometries is difficult. Research conducted on transitional flows and turbulent flows still widely use these methods for simple geometries.

Spectral element methods, mainly used for complex turbulent flows, which merge the geometric flexibility of the finite element method with the best convergence properties of the spectral methods, were developed due to the limitations of applying spectral methods in to complex geometries [15].

Higher order finite difference methods are now used extensively for complex geometries paying more attention to the design of the spatial and discretisation schemes when it comes to applying these methods [15]. The reason for this is to make sure that the numerical dissipation does not swamp turbulent eddy dissipation and also to ensure the method is stable.

Computational speed and memory required remains the main challenge in using DNS. As the Reynolds number increases the range of scales in turbulent flows increases quickly. This results in an increase in the size ratio of largest to smallest vortices as the turbulent flow contains wide spectrum of vortices and becomes difficult to accomplish the DNS of turbulent flows at high Reynolds numbers. Most of the practical problems regarding fluid flows in engineering are turbulent, such as a flow around a car, and have a wide range of scales.

2.2.3 Large Eddy Simulation

A very popular method used in simulating turbulent flows is Large Eddy Simulation (LES). One of the reasons for this method is that the computational cost for LES is between RANS and DNS. Also the limitations posed by RANS and DNS are the reason behind the success of LES [17]. The approach used in LES is that the larger eddies are computed for each problem with a time dependent simulation and a compact model captures the activity of the small eddies. In other words the large eddies are computed explicitly while simple models represent the small scale eddies. The larger eddies and smaller eddies are separated by using a spatial filtering operation.

The process of not representing the small scale eddies explicitly lowers the computational cost in LES compared to DNS [18].

The process of filtering decomposes the velocity, $\boldsymbol{U}(\boldsymbol{x}, t)$ into the sum of a filtered component, $\bar{\boldsymbol{U}}(\boldsymbol{x}, t)$and a sub grid scale (SGS) component $\boldsymbol{u}'(\boldsymbol{x}, t)$ The motion of the large eddies are represented by the filtered velocity field which is time dependent and three dimensional.

The most common filters used in the three dimensional LES are:

- Top hat or box filter
- Gaussian filter
- Spectral cutoff

The filtering operation starts with a selection of a filtering function and a cutoff width. The size of eddies which are to be retained and rejected depends on the cutoff width. The filtering removes length scales below a cutoff scale, L_c and timescales, T_c below. The cutoff width can be any size but normally the large eddies to be solved have a length scale greater than the cutoff width. The smaller length scale eddies are destroyed during the spatial filtering information [15]. Increasing the filter width will remove more scales from the velocity field and this will result in an increase of stress contribution [19].

Only a small amount of turbulent kinetic energy (TKE) is resolved by the SGS model. Larger scales contain the most energy and these larger scales are resolved. Since the SGS models do not need to be more accurate.

Some of the important SGS models are:

- Smagorinsky model: This is an eddy viscosity model which uses the Boussinesq approximation and assumes that SGS turbulence is in equilibrium.
- Dynamic model: Uses a fine filter at the mesh width and a coarse filter at a larger width. Works out the decay of TKE with scale and extrapolate to the SGS. Assumes that the coarser filter is in the inertial range.
- Implicit filtering: Computational effort of explicit filtering is not used in this model but the artificial viscosity of the numerical method is used instead.

Considerable computing resources are required for LES. For LES to be used in industries as a general purpose tool in flows with complex geometries it needs additional research and development. LES has proven to be more useful in delivering the valuable information in turbulent flows where laboratories fail to measure the turbulence properties due to the lack of suitable experimental techniques. Hence the use of LES as a research tool guides the development of classical models through comparative studies.

Chapter 3

Governing Equations and Numerical Methods

3.1 Governing Equations

The three-dimensional compressible Euler equations in conservative variables for a Cartesian co-ordinate system can be written as,

$$\frac{\partial \mathbf{U}}{\partial t} + \frac{\partial \mathbf{F}}{\partial x} + \frac{\partial \mathbf{G}}{\partial y} + \frac{\partial \mathbf{H}}{\partial z} = 0 \tag{3.1}$$

where

$$\mathbf{U} = [\rho, \rho u, \rho v, \rho w, E]^T \tag{3.2}$$

$$\mathbf{F} = [\rho u, \rho u^2 + p, \rho uv, \rho uw, u(E + p)]^T \tag{3.3}$$

$$\mathbf{G} = [\rho v, \rho uv, \rho v^2 + p, \rho vw, v(E + p)]^T \tag{3.4}$$

$$\mathbf{H} = [\rho w, \rho uw, \rho vw, \rho w^2 + p, w(E + p)]^T \tag{3.5}$$

and ρ, u, v, w are density and Cartesian velocity components respectively. Throughout this paper it is assumed that the fluid behaves as ideal gas where $\gamma = 5/3$.

The total energy per volume, E is given by,

$$E = \rho \left[\frac{1}{2}(u^2 + v^2 + w^2) + e \right] \tag{3.6}$$

and the internal energy, e, for the perfect gas assumption can be expressed as,

$$e = \frac{p}{\rho(\gamma - 1)} \tag{3.7}$$

The volume fraction multispecies model is used as a passive scalar to track species [20], which substitutes the continuity equation for two conservation equations for species densities multiplied by volume fractions, i.e. ρz_1 and ρz_2 and a quasi-linear volume fraction equation,

$$\frac{\partial z}{\partial t} + u\frac{\partial z}{\partial x} = 0 \tag{3.8}$$

where the volume fraction z is given by,

$$z_1 = z \,\text{and}\;\; z_2 = 1 - z \tag{3.9}$$

and density,

$$\rho = \;\; z_1\rho_1 + \;\; z_2\rho_2 \tag{3.10}$$

The numerical scheme, 2^{nd} and 5^{th} order Godunov scheme with and without low Mach number correction feature, employs this method directly.

3.2 Finite Volume Method

The foundation of a finite volume method is to discretise the integral form of the equations representing the conservation laws over each control volume of the computational domain.

The finite volume method derived below in one dimension is based on the method used by Leveque [21].

In one dimension the advection equation is,

$$\frac{\partial u}{\partial t} + \frac{\partial f}{\partial x} = 0 \tag{3.11}$$

The basic integral form of a conservation law is given by,

$$\frac{\mathrm{d}}{\mathrm{d}t}\int_{x_1}^{x_2} u(x,t)\,\mathrm{d}x = F_1(t) - F_2(t) \tag{3.12}$$

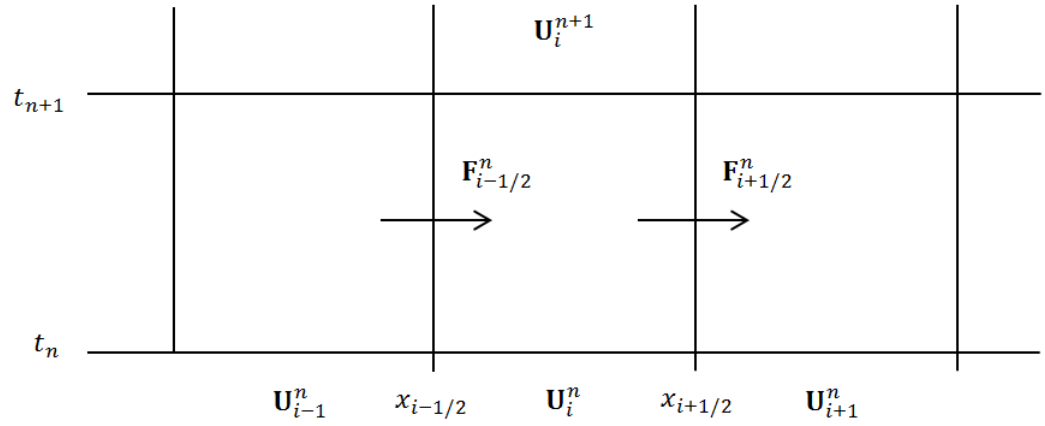

Figure 3.1: Finite volume method illustration for updating the cell average U_i^n at the cell faces in $x-t$ plane

In Figure 3.1 the length of the cell, Δx is given by,

$$\Delta x = x_{i+1/2} - x_{i-1/2} \tag{3.13}$$

Applying the integral form of the conservation law in equation 3.12 for the ith grid cell in Figure 3.1 gives,

$$\frac{\mathrm{d}}{\mathrm{d}t} \int_{x_i-\frac{1}{2}}^{x_i+\frac{1}{2}} u(x,t)\,\mathrm{d}x = f\left[q\left(x_{i-\frac{1}{2}},t\right)\right] - f\left[q\left(x_{i+\frac{1}{2}},t\right)\right] \tag{3.14}$$

The approximation of the average value over the cell, i at time, t_n is given by,

$$U_i^n \approx \frac{1}{\Delta x} \int_{i-\frac{1}{2}}^{i+\frac{1}{2}} u(x,t_n)\,\mathrm{d}x \tag{3.15}$$

Integrating the above equation from t_n to t_{n+1} gives,

$$\int_{x_i-\frac{1}{2}}^{x_i+\frac{1}{2}} u(x,t_{n+1})\,\mathrm{d}x - \int_{x_i-\frac{1}{2}}^{x_i+\frac{1}{2}} u(x,t_n)\,\mathrm{d}x = \int_{t_n}^{t_{n+1}} f\left[q\left(x_{i-\frac{1}{2}},t\right)\right]\,\mathrm{d}t - \int_{t_n}^{t_{n+1}} f\left[q\left(x_{i+\frac{1}{2}},t\right)\right]\,\mathrm{d}t \tag{3.16}$$

Rearranging and dividing the above equation by the length of the cell, Δx gives,

$$\frac{1}{\Delta x}\int_{x_i-\frac{1}{2}}^{x_i+\frac{1}{2}} u(x,t_{n+1})\,\mathrm{d}x = \frac{1}{\Delta x}\int_{x_i-\frac{1}{2}}^{x_i+\frac{1}{2}} u(x,t_n)\,\mathrm{d}x - \frac{1}{\Delta x}\left[\int_{t_n}^{t_{n+1}} f\left(q\left(x_{i+\frac{1}{2}},t\right)\right)\,\mathrm{d}t - \int_{t_n}^{t_{n+1}} f\left(q\left(x_{i-\frac{1}{2}},t\right)\right)\,\mathrm{d}t\right] \tag{3.17}$$

$$U_i^{n+1} \;=\; U_i^n - \frac{\Delta t}{\Delta x}\left(F_{i+1/2}^n - F_{i-1/2}^n\right) \tag{3.18}$$

where the time step size, Δt is given by,

$$\Delta t = t_{n+1} - t_n \tag{3.19}$$

and $F_{i-1/2}^n$ is the approximation to the average flux along the cell interface, $x_{i-1/2}$ is given by,

$$F_{i-1/2}^n \approx \frac{1}{\Delta t}\int_n^{t_{n+1}} u(x_{i-1/2},t)\,\mathrm{d}t \tag{3.20}$$

and similarly $F_{i+1/2}^n$ is given by,

$$F_{i+1/2}^n \approx \frac{1}{\Delta t}\int_n^{t_{n+1}} u(x_{i+1/2},t)\,\mathrm{d}t \tag{3.21}$$

Rearranging equation 3.18 gives,

$$\frac{U_i^{n+1} \;-\; U_i^n}{\Delta t} + \frac{F_{i+1/2}^n - F_{i-1/2}^n}{\Delta x} = 0 \tag{3.22}$$

Equation 3.22 is the finite volume method approximation of the conservation law equation 3.11.

3.3 Explicit and Implicit Methods

Time integration is a technique used in numerical analysis to obtain numerical solution where time is discretised on a finite grid. Using the known positions and their time derivatives the time integration procedure produces the same quantities at a later time. The two most common time integration techniques used in numerical analysis are,

- Explicit time stepping method
- Implicit time stepping method

The explicit method uses the known properties of the past state to calculate the properties at the current state while the implicit method solves a coupled equation with properties of current and past state to calculate the properties at the current state.

Explicit time stepping method imposes a strict time step restriction imposed by the form of,

$$C = \frac{u\Delta t}{\Delta x} < 1 \tag{3.23}$$

3.4 Courant Friedrichs Lewy (CFL) Number

A necessary stability criterion used in the explicit time marching schemes is the Courant–Friedrichs–Lewy condition generally known as the CFL condition or Courant number. The CFL condition was described by Richard Courant, Kurt Friedrichs, and Hans Lewy in 1928.

Courant number is defined as,

$$C = \frac{u\Delta t}{\Delta x} \tag{3.24}$$

In a given time step, Δt, the information, u, travels across a distance given by, $u\Delta t$ over one time step. In order for the information to propagate through one grid cell, $u\Delta t$, at each time step the distance which the information propagates should be less than the distance of the grid size.

This condition is given by,

$$u\Delta t < \Delta x \tag{3.25}$$

Therefore,

$$\frac{u\Delta t}{\Delta x} < 1 \tag{3.26}$$

The CFL condition is given by,

$$C = \frac{u\Delta t}{\Delta x} < 1 \tag{3.27}$$

The above equation shows that the Courant number should not be greater than one in order to satisfy the condition mentioned earlier. If the Courant number is grater than one the information is propagating through more than one grid size at each time step.

The Courant number is a dimentionless quantity and can be written as the ratio of two speeds,

$$C = \frac{u}{\Delta x/\Delta t} = \frac{\text{speed of information}}{\text{speed of mesh}} \tag{3.28}$$

For positive and negative speeds of information, u, the following notation is used [22],

$$u^+ = \max(u, 0) = \frac{1}{2}(u + |u|) \tag{3.29}$$

and,

$$u^- = \min(u, 0) = \frac{1}{2}(u - |u|) \tag{3.30}$$

Based on the positive and negative speed of information the Courant number can be modified as,

$$C = \frac{u^+ \Delta t}{\Delta x} \tag{3.31}$$

and,

$$C = \frac{u^- \Delta t}{\Delta x} \tag{3.32}$$

3.5 Numerical Methods

In order to highlight the scheme performance of vortical, flows the results are obtained for this well posed, two mode, two-dimensional Kelvin–Helmholtz instability test case from two different numerical schemes, 2^{nd} and 5^{th} order Godunov scheme with and without low Mach number correction feature and compressible flow solver of the commercial CFD software, ANSYS Fluent [23] for both implicit and explicit time stepping methods.

The results are non-dimensionalised in each case by velocity difference and wavelength of the 1^{st} mode for the time scales and by wavelength of the 1^{st} mode for momentum thickness.

3.5.1 CHOC

The proposal of low Mach correction by Thornber *et al.* [24] is a simple modification of the finite volume Godunov method to significantly improve performance at low Mach number in turbulent flows. In this modified scheme the dissipation of the numerical scheme becomes constant in the limit of zero Mach number, as opposed to tending to infinity as in the case for the traditional scheme, shown analytically and through numerical test cases in the proposal of this scheme. As described by the authors, the key feature of this numerical scheme is that the reconstruction is modified locally, hence the scheme can capture both shock waves and low Mach number features in the same computational domain using the same formulation of the governing equations. Also,

as the Mach number decreases, this modification recovers the correct scaling of the pressure and density fluctuations.

This simple modification is employed in `CHOC` (Compressible High-Order Combustion) [25], where the compressible Navier-Stokes equations are solved using a 5^{th} order in space [24] MUSCL scheme, explicit 2^{nd} order in time [26] Runge–Kutta method based on finite volume Godunov method in utilising the HLLC Riemann solver detailed in Toro [22]. The scheme is derived for compressible turbulent mixing requiring good resolution of shocks and contact surfaces, and for combustion problems [25].

3.5.2 ANSYS Fluent

Both implicit and explicit temporal discretisation method for compressible flow solver in ANSYS Fluent is chosen in this test case to capture the development of the Kelvin–Helmholtz instability growth. The flow field of the test case is initialised in ANSYS Fluent by using a user defined function (UDF), written in the C programming language, together with an execute at end function to provide the momentum thickness of the mixing layer.

3.5.3 TURMOIL

The vortex pairing process results included in this thesis for Lagrange-remap method simulation are obtained from David Youngs at AWE (UK) [14].

A Lagrange-remap method [27] is used in `TURMOIL` and the gas mixtures are given by a mass fraction advection equation [28]. The changes in velocity and internal energy due to the pressure field are calculated by the Lagrange phase. Density, mass fraction and internal energy are all defined at the cell centres while the velocity components are all defined at the cell corners.

The finite difference approximation used in this Lagrange remap method is 2^{nd} order accurate in space and time, non-dissipative in the absence of shocks and conserves total energy. The use of quadratic artificial viscosity, q provides the dissipation due to shocks. The partial derivatives denote centred differences. In this method there are oscillations after shocks and the handling of shocks is not good compared to the 2^{nd} order Godunov methods. But this method has a very useful property, at low Mach number, near incompressible flow, the irreversible dissipation of kinetic energy is negligible. So this method avoids the problem experienced at low Mach numbers in Godunov methods without the low Mach correction of Thornber *et al.* [24]. In the Lagrange phase all three spatial directions are calculated simultaneously. The remap phase calculates advective fluxes and may be regarded as a mapping of the configuration at the end of the Lagrangian phase back to the original mesh. Alternatively, near-Lagrangian mesh motion can be used in the radial direction to reduce numerical diffusion in implosion problems. A 3^{rd} order monotonic method based on the work of van Leer is used to calculate the advection in separate 1D sweeps and at every time step the order of the sweeps is reversed. Several Lagrange steps can be performed per remap step, considerably increasing the performance of low the Mach number calculations. The method gives exact monotonic behaviour, i.e. fluid variables at the end of the remap phase lie with the range of neighbouring values at the end of the Lagrange phase. Mass, internal energy and momentum are conserved by the remap phase but dissipating the kinetic energy. The simple algebraic technique by DeBar [29] can be used to determine the loss of kinetic energy in the remap phase accurately as a function of position and could be added on to the internal energy in order to recover the total energy conservation. The 'sub-grid' dissipation can

be quantified by using this technique. At steep velocity gradients dissipation occurs and it is negligible in the flow regions which are resolved better. The resulting dissipation is comparable with that obtained with an explicit sub-grid-scale model. In Lagrange-remap method the solution is independent of Mach number hence this method should perform well here.

3.5.4 TRICLADE

The vortex pairing process results included in this thesis for the wave propagation algorithm and Godunov method with SLAU numerical flux simulations are obtained from Jérôme Griffond at CEA (France) [13].

The `TRICLADE` code is a massively parallel code intended to solve turbulent mixing of perfect or stiffened gas in shock-tube applications. It solves the compressible Navier–Stokes equations with additional equations for the mass fractions.

Several different shock capturing numerical methods are implemented into `TRICLADE`. The one mostly used in previous applications [30, 31], hereafter referred as WP5, is of conservative finite difference type based on the wave propagation algorithm of Leveque [32] with high accuracy provided by the corrections due to Daru and Tenaud [33]. Directional splitting is used and uniform time-space accuracy for one-dimensional problems is reached thanks to the kind of generalised Lax–Wendroff procedure of [33]. Time-space accuracy of 5^{th} order is used here and monotonicity preserving (MP) limitation is applied (implemented in `TRICLADE` as described by [33]). Since there is no shock in the present test case, the computation can be performed without any the limitation. However since this thesis focuses on situations where both shock waves and low Mach regions are in the flowfield, the computation must include the ability to treat shock waves in order to be relevant, because it takes the full structure of Riemann solvers (from Toro [22]) into account, the WP5 method is one-step and therefore computationally very efficient. However, the different ways mentioned hereafter to cure the over-dissipation in the low Mach limit are very difficult to adapt in this algorithm.

That is why other methods of `TRICLADE` have also been used for the present test case. Among them, good results have been obtained in the low Mach limit, based on a finite volume scheme with 5^{th} order spatial and 3^{rd} order temporal accuracy (strong stability preserving Runge-Kutta scheme), hereafter referred as M5. The 'accuracy preserving' version of the MP limitation proposed by Suresh and Huynh [34] is employed. Two kinds of tests have been performed with this M5 method,

- using the correction of Thornber *et al* [24], with different classical numerical fluxes
- using numerical fluxes especially intended to treat the low Mach limit, cf Dellacherie [35], Li and Gu [36] or Shima and Kitamura [37]

In accordance with the `CHOC` code, the first approach appears successful. Concerning the second one, the robustness differs depending on the numerical flux. It means that even if all are successful for the present test case, only few are applicable to various configurations. Among them, the SLAU flux of Shima and Kitamura [37] deserves to be cited because of it robustness, accuracy and wide applicability. The finite volume method with the SLAU numerical flux includes the low Mach capture property.

Chapter 4

Literature Review

4.1 Background Theory

Hydrodynamic instability can be described as an unstable reaction due to small perturbations. This instability in laminar flow results in turbulence and Kelvin–Helmholtz instability is a typical example of this.

Kelvin–Helmholtz instability exists in shear layers where there is sufficient velocity difference across the interface between the two fluids resulting in vortex roll ups due to the excess shear in the region of interface. The pairing process of these vortices at moderate Reynolds number is the initial stage in the development of a turbulent shear layer.

During the investigation on vortex pairing, an experiment was carried by Winant and Browand [4] where two streams of water, flowing at different velocities, are brought together to form a mixing layer to observe the vortex roll up. Vortex pairing is a process where interaction of two adjoining vortices results in a single, larger vortex which enhances the turbulent mixing layer growth. The velocity difference between the two mixing layers produce the energy needed for these vortex structures to roll up along the mixing layer and produce a single, larger vortex structure.

Figure 4.1 shows the apparatus used to generate the flow field during the flow visualisation experiment of turbulent mixing-layer growth. A splitter plate was used to separate the two streams of water before they were brought together. The wake generated by the plate was very thin and undetectable $1cm$ downstream of the origin. The boundary layer, previously developed before the two streams brought together, was removed during the experiment by a fine mesh screen attached at the end of the splitter plate. This screen introduced slight flow non-uniformities, 0.5% of the local mean velocity, and disappeared within a few centimetres of the origin. In order to observe the vortical structures dye was injected between the two streams just upstream of the mesh screen.

The test section was $1.5m$ long with a free surface where the probes could be used and had a cross section of $10cm \times 10cm$. A camera was attached on the side of a carriage platform to capture the flow visualisation where the carriage was supported on air bearings and driven above the channel at mean flow velocity along the test section. The quantitative measurements such as mean velocity profiles, the distribution of velocity fluctuations and mixing layer growth were collected by the use of a hot film probe.

During the experiment the upper layer flow velocity was set at $1.44cm/s$ and the lower layer

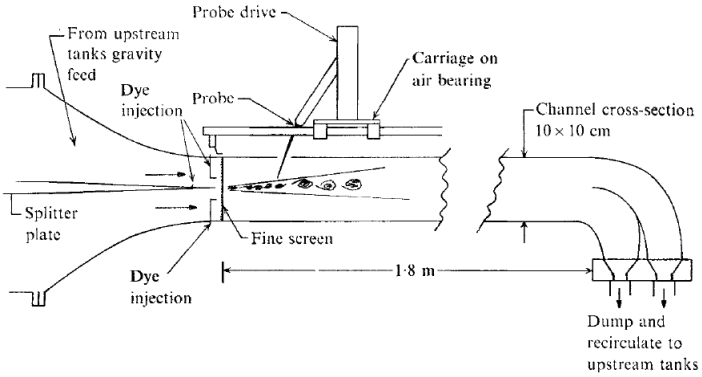

Figure 4.1: Schematic diagram of the apparatus used to generate a flow field during the flow visualisation experiment of turbulent mixing-layer growth at moderate Reynolds number by Winant and Browand (not to scale) [4]

flow velocity at $4.06cm/s$, corresponding to a velocity difference, ΔU, of $2.62cm/s$ and a mean velocity, $\bar{U}$, of $2.75cm/s$. Neighbouring pairs of vortices rolling around each other, forming larger vortical structures with axis perpendicular to the mean flow direction, was observed during the experiment.

The vortex paring process observed in the experiment conducted by Winant and Browand [4] is illustrated in Figure 4.2. The sequence of these photographs were taken by a camera moving at the mean speed, $\bar{U}$. The fluid flows from left hand side to the right hand side in this experiment and the velocity of the lower layer is higher than the velocity of the upper layer. From the photographs the vortex pairing process can be easily identified. The two initial vortices rolled up due to the instability at $t = 10s$ are shown in Figure 4.2(a). As the time progresses the two separate vortices continue to roll up and get closer to each other and start to combine together, illustrated in Figures 4.2(b) and 4.2(c) respectively. The final structure, a large, single vortex formed at $t = 14.5s$ is shown in Figure 4.2(d). The combination of these large scale vortical structures influence the growth of the turbulent mixing layer.

4.2 Kelvin–Helmholtz Instability

The instability which occurs at the interface of two fluids flowing in a horizontal direction is called the Kelvin–Helmholtz instability. The velocity difference between the two fluids produces the Kelvin–Helmholtz instability and is due to the destabilizing effect of shear, which overcomes the stabilizing effect of stratification. Kelvin–Helmholtz instability can be generated in a laboratory by filling a glass tube which has a rectangular cross sectional area with two different coloured liquids of different densities and tilting the tube. This process initiates a current in the lower layer down the plane and also a current in the upper layer up the plane as shown in Figure 4.3 [5].

Figure 4.4 shows a simple shear flow where in the x direction the flow velocities are U and 0 in the regions of $y > 0$ and $y < 0$ respectively. The vorticity is zero everywhere apart from $y = 0$. The concentration of vorticity on the surface $y = 0$ is also referred to as a vortex sheet. The

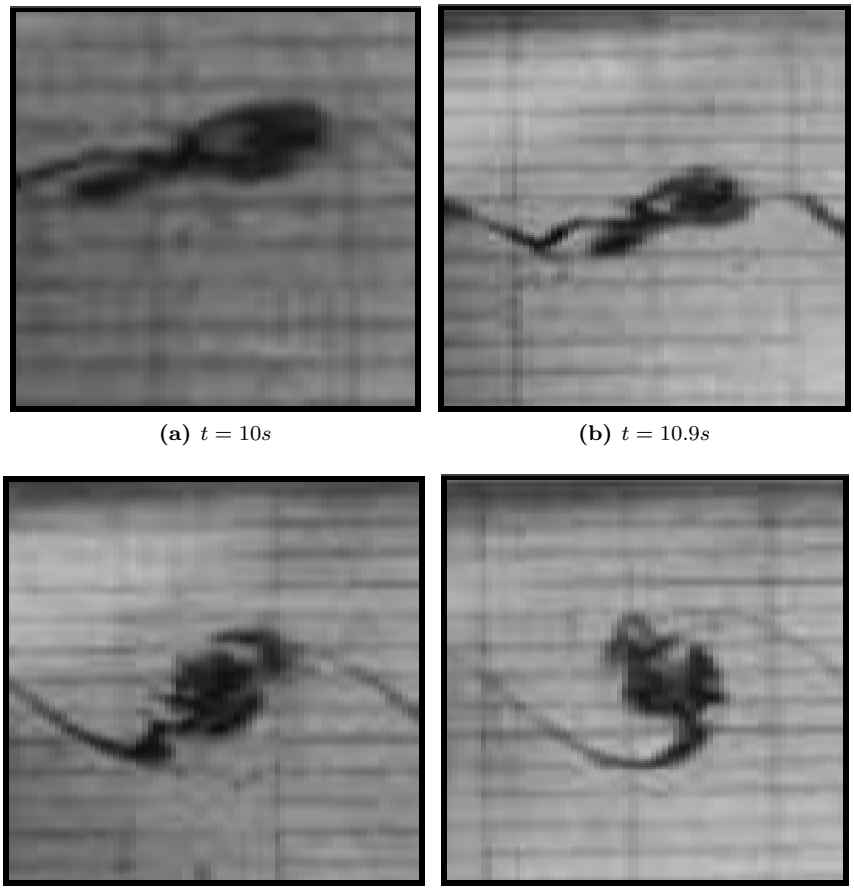

(a) $t = 10s$ **(b)** $t = 10.9s$

(c) $t = 12.7s$ **(d)** $t = 14.5s$

Figure 4.2: Sequence of photographs showing the vortex pairing process observed during the flow visualisation experiment carried out by Winant and Browand [4]

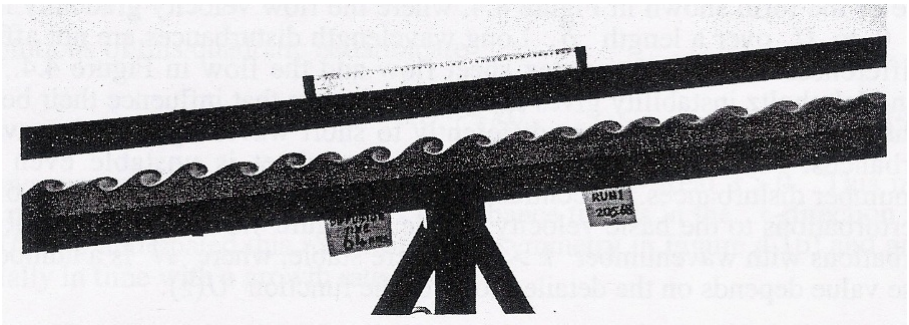

Figure 4.3: Illustration of Kelvin–Helmholtz instability generated in laboratory by tilting a horizontal tube which has two liquids of slightly different densities [5]

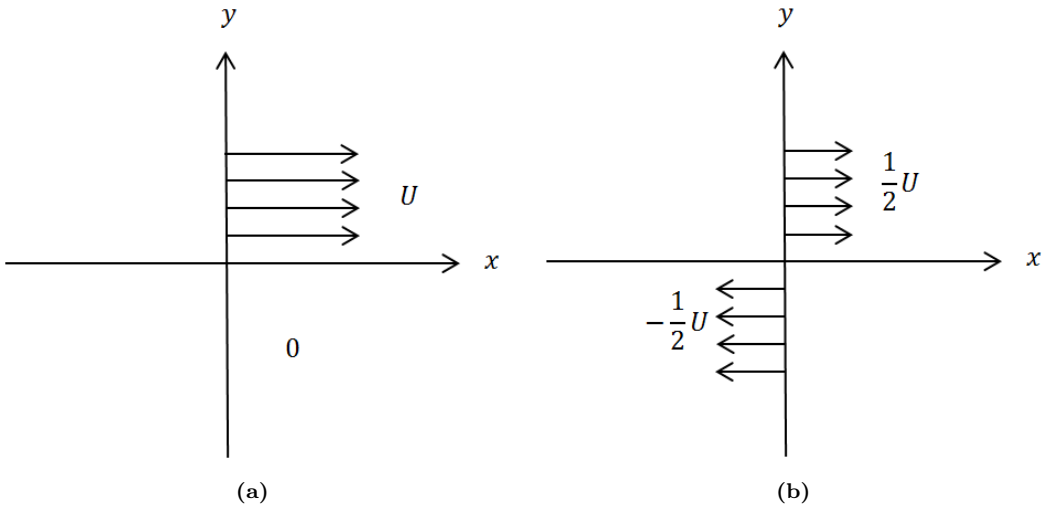

Figure 4.4: Flow profile of a vortex sheet in a reference frame which is (a) stationary (b) moving with a speed of 0.5 U

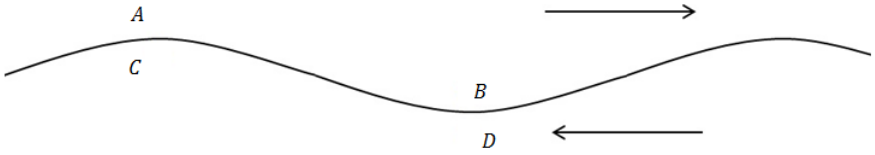

Figure 4.5: The physical representation of Kelvin–Helmholtz instability

Kelvin–Helmholtz instability theory derived below is based on the lecture notes of Dowling [38].

The Kelvin-Helmholtz instability can be explained with a simple physical explanation. The basic flow is symmetric in a frame of reference moving with the average velocity and by symmetry the wave should have no preference between the positive and negative x directions. In Figure 4.5 the streamline converges at points A and D and the flow speed increases over the crests and at points B and C (troughs) the flow speed decreases. The tangential velocity at points A and D are higher than at points C and B. From Bernoulli's equation the pressure at points at A and D should be lower than at points B and C and the fluid should accelerate between points A and C to balance this pressure difference. A similar acceleration occurs between points B and D. These accelerations tend to increase the amplitude of the perturbation and result in the flow being unstable.

The equations of motion can more precisely represent the way in which the unstable flow develops. By considering a linear perturbation which is proportional to $e^{(st+ikx)}$ to the interface between the two flows in Figure 4.6 the position of the interface can be written at time t as, $z = \eta(x,t) = \eta_0 e^{(st+ikx)}$, and for linear disturbances $\eta_0 e^{(st)}$ is small.

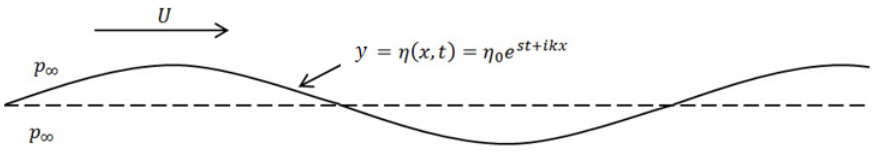

Figure 4.6: Vortex sheet with the linear disturbances

The flow is irrotational in the region $y > \eta(x,t)$ and the velocity potential $\phi(x,t)$ can be written terms of the mean flow and the linear perturbation,

$$\phi(x,t) = Ux + f(y)e^{(st+ikx)} \text{ in } y > \eta(x,t) \tag{4.1}$$

$f(y)$ satisfies the Laplace equation,

$$\bigtriangledown^2\phi = 0 \tag{4.2}$$

So,

$$\frac{\partial^2\phi}{\partial x^2} + \frac{\partial^2\phi}{\partial y^2} + \frac{\partial^2\phi}{\partial z^2} = 0 \tag{4.3}$$

$$-k^2 f(y) + f''(y) = 0 \tag{4.4}$$

The general solution for the above ODE is,

$$f(y) = A_1 e^{(-ky)} + A_2 e^{(ky)} \tag{4.5}$$

Where A_1 and A_2 are constants.

As $y \to \infty$ constant $A_2 = 0$

So,

$$\phi(x,t) = U_x + A_1 e^{(st+ikx-ky)} \text{ in } y > \eta(x,t) \tag{4.6}$$

Similarly as $y \to -\infty$,

$$\phi(x,t) = B_1 e^{(st+ikx+ky)} \text{ in } y < \eta(x,t) \tag{4.7}$$

The y coordinate of the fluid particles which make up the interface is $\eta(x,t)$ and therefore the y velocity is D_η/D_t.

$$\frac{\partial \phi}{\partial y} = \frac{D_\eta}{D_t} = \frac{\partial \eta}{\partial t} + \frac{\partial \phi}{\partial x}\frac{\partial \eta}{\partial x} \text{ on } y = \eta(x,t) \tag{4.8}$$

A_1, B_1 and η are all so small because of the assumption of linearity, their products can be ignored as we are considering small amplitude distances.

$$\frac{\partial \phi}{\partial y} = \frac{\partial \eta}{\partial t} + U\frac{\partial \eta}{\partial x} \text{ on } y = \eta(x,t) \tag{4.9}$$

$$-A_1 k e^{(-k\eta)} = (s + ikU)\eta_0 \tag{4.10}$$

Using the expansion for small $k\eta$,

$$e^{(-k\eta)} = 1 - k\eta + \mathcal{O}(\eta^2) \tag{4.11}$$

The equation simplifies to,

$$-A_1 k = (s + ikU)\eta_0 \tag{4.12}$$

In a similar way for $y < \eta(x,t)$ the argument for $\eta(x,t)$ leads to the second boundary condition,

$$B_1 k = s\eta_0 \tag{4.13}$$

Across the interface the pressure is continuous and Bernoulli's equation for unsteady state shows that,

$$p + \rho\frac{\partial \phi}{\partial t} + \frac{1}{2}\rho|\mathbf{u}|^2 + \rho g y = \text{constant} \tag{4.14}$$

This can be applied to the region $y > \eta(x,t)$,

$$p(x,\eta,t) + \frac{\partial \phi}{\partial t} + \frac{1}{2}\rho\left(\frac{\partial \phi}{\partial t}\right)^2 + \rho g\eta = p_\infty + \frac{1}{2}\rho U^2 \tag{4.15}$$

$$\left(\frac{\partial \phi}{\partial t}\right)^2 = U^2 + 2iUkA_1 e^{(st+ikx-k\eta)} + \text{nonlinear terms} \tag{4.16}$$

By substitution for ϕ and η,

$$p(x,\eta,t) = p_\infty - \rho(s+ikU)A_1 e^{(st+ikx-k\eta)} - \rho g\eta_0 e^{(st+ikx)} \tag{4.17}$$

Using the expansion for small $k\eta$ and neglecting any nonlinear terms,

$$p(x,\eta,t) = p_\infty - \rho(s+ikU)A_1 e^{(st+ikx)} - \rho g\eta_0 e^{(st+ikx)} \tag{4.18}$$

Similarly for region $y < \eta(x,t)$ leads to,

$$p(x,\eta,t) = p_\infty - \rho sB_1 e^{(st+ikx)} - \rho g\eta_0 e^{(st+ikx)} \tag{4.19}$$

Since the pressure must be equal,

$$A_1(s+ikU) = B_1 s \tag{4.20}$$

Substitution for A_1 and B_1 leads to,

$$s^2 + (s+ikU)^2 = 0 \tag{4.21}$$

The solutions for the above quadratic equation are,

$$s = -\frac{1}{2}iUk \pm \frac{1}{2}Uk \tag{4.22}$$

There is an unstable mode for each wavenumber, k with real $s > 0$. This mode leads to,

$$\eta(x,t) = \eta_0 e^{[\frac{1}{2}kUt + ik(x-\frac{1}{2}Ut)]} \tag{4.23}$$

This disturbance travels in the x direction with speed $(1/2)U$ and grows exponentially in time with a growth rate $(1/2)kU$.

4.3 Mixing Layer

Turbulence enhances the mixing of fluids in both nature and industry and due to this, the turbulent mixing layer has been an important research topic in the past and present in fluid dynamics, both numerically and experimentally. During experimental investigations in the past on turbulent mixing, vortical structures were observed. Further investigation revealed amalgamation of neighbouring vortical structures, termed as vortex pairing, formed larger, single vortices downstream of the flow. These large structures played an important role in the mixing layer growth. Experiments were conducted for various Reynolds number, from low to high, fluid flows and also the density effects on the mixing layer were investigated.

To study the density ratio effects on turbulent mixing in incompressible flow and also the large vortex structure in the mixing layer, an experiment was conducted by Brown and Roshko [6]. Two different gases were used in the experiment in order to study the dynamic effects of density non-uniformity. The results from the experiment for flow structures showed that the spacing of the eddies in the laminar instability layer was equal to the wavelength of the initial small disturbance which resulted in the development of the eddies. In the turbulent instability layer, the spacing of the eddies increased as the downstream distance increased. The apparatus used by Brown and Roshko [6] for the mixing layer of the two gases is shown in figure 4.7. According to the authors the apparatus, a high-pressure short-run-time wind tunnel, was designed particularly for the mixing layer experiment with cost of the gas consumption in mind, by operating at high pressure for short flow times.

Browand and Weidman [7] described a technique to measure the largest scales of motion using conditional sampling during an experiment conducted on mixing layer. The results obtained from the conditional sampling showed the association between the vortex pairing process and the Reynolds stress production. The authors also mentioned that over a wide range, the qualitative features of the paired single, large vortex created during the vortex pairing process were insensitive Reynolds number variation, validating the observation by Brown and Roshko [6]. Figure 4.8 shows the apparatus used during the experiment of large scales in the developing mixing layer by Browand and Weidman. This apparatus is similar to the one used by Winant and Browand [4] during the experiment on vortex pairing, where the experimental results are related to this two mode Kelvin-Helmholtz instability test problem.

The appearance of large vortical structures in the mixing layers at high Reynolds numbers were observed experimentally by Dimotakis and Brown [8]. The apparatus used in the experiment is shown in Figure 4.9. The authors observed the vortex pairing process at high Reynolds number as similar to the one observed by Winant and Browand [4] at low Reynolds numbers. But a more violent process was observed at high Reynolds number for the decaying process for the paired large vortex structure. The author described the observed result of a paired large vortex decaying in the mixing layer as tearing, a large vortex structure appeared to be surrounded by or caught between two other structures and broke up into parts as a result of the straining field of the neighbouring structures.

The influence of the initial boundary layer on a turbulent mixing layer growth was experimentally studied by Browand and Latigo [39]. This experiment was carried out for two cases, laminar and turbulent boundary layers prior to the separation. For the turbulent case one of the boundary layers, the high speed side, was made turbulent by using a hot wire. The results showed that the growth of the mixing layer is more rapid for the laminar boundary layer when compared to

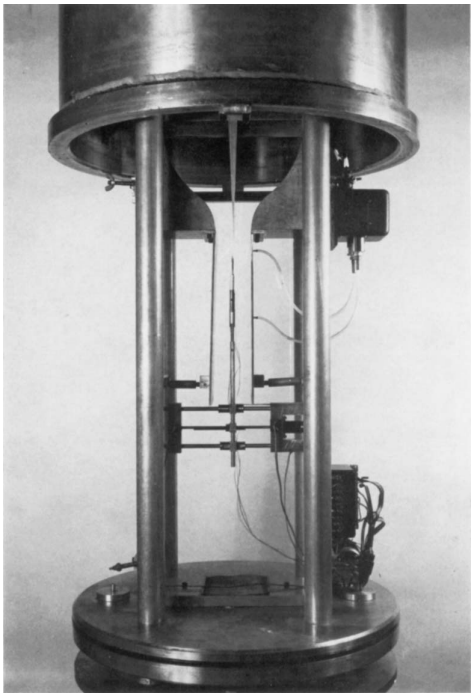

Figure 4.7: Mixing layer apparatus used in the experiment on density effects and large structure in turbulent mixing layers by Brown and Roshko [6]

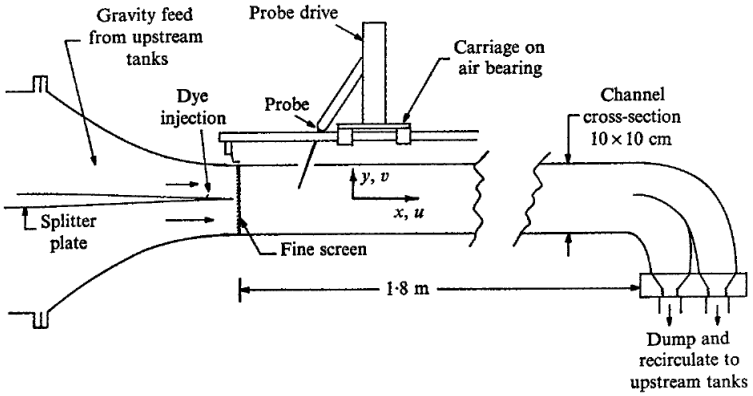

Figure 4.8: Schematic diagram of the apparatus used to generate a flow field during the flow visualisation experiment of turbulent mixing-layer growth at moderate Reynolds number by Browand and Weidman (not to scale) [7]

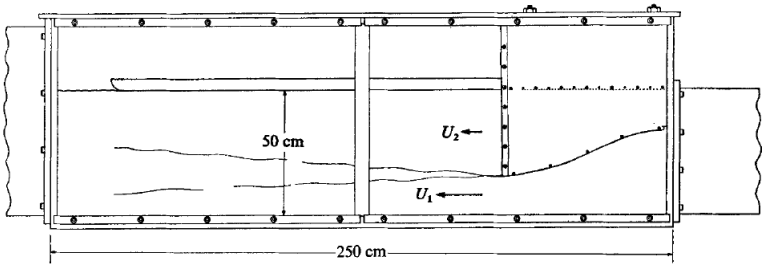

Figure 4.9: Test section of the GALCIT free surface water tunnel used during the experiment, the mixing layer at high Reynolds number: large-structure dynamics and entrainment by Dimotakis and Brown [8]

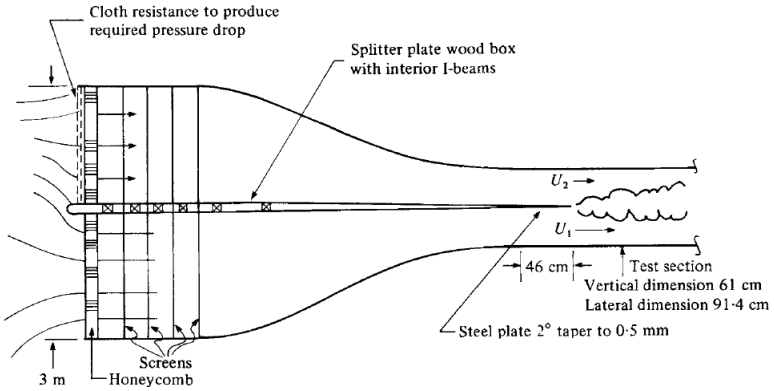

Figure 4.10: Schematic diagram of the wind tunnel used by Browand and Latigo during the experiment on spanwise structure in the two-dimensional mixing layer [9]

the turbulent boundary layer. The authors concluded that the introduction of the small scale turbulence in the boundary layer has prevented the growth of the larger scale structures which promote the mixing layer growth.

In an attempt to solve the problems in turbulent mixing layers, such as the lateral scale linked with the large scale structures and the scale change process of these structures as they move downstream, an experiment was carried out by Browand and Troutt [9]. Figure 4.10 shows the schematic diagram of the wind tunnel, the same wind tunnel used by Browand and Latigo [39], used in this experiment. In this experiment the necessary data were collected by placing a linear array of hot wires across the span of a two-dimensional mixing layer. Six downstream locations, between $4cm$ and $92cm$, were chosen to take the hot wire measurements as shown in figure 4.11. The Reynolds number, based on the velocity difference and the maximum slope thickness of the mixing layer, corresponds to these locations varied from 3300 to 186000. The maximum slope thickness at the downstream distance of $92cm$ was $13cm$ in this experiment. A cloth resistance was added to the upper half of the tunnel to produce a lower velocity. The splitter plate had no tripping device attached to in order to allow the mixing layer to enter transition from initially laminar boundary layer. The velocity ratio, λ was given by,

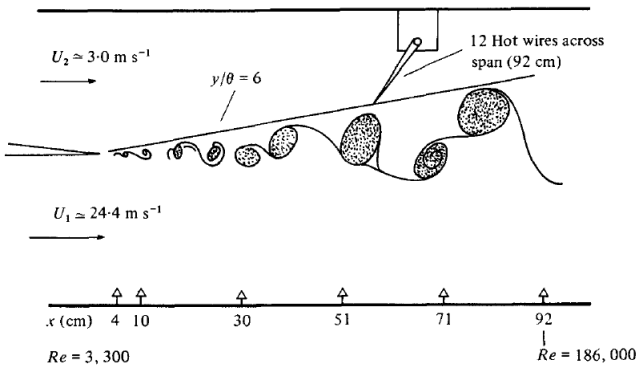

Figure 4.11: Schematic diagram of the test set-up used by Browand and Troutt during the experiment on spanwise structure in the two dimensional mixing layer [9]

$$\lambda = (U_1 - U_2)/(U_1 + U_2) = 0.8 \quad \text{where } U_1 > U_2 \tag{4.24}$$

The results from the experiment by Browand and Troutt [9] showed the local thickness of the mixing layer grew linearly from the origin and the implication of this was that the non-dimensional separation distance of the mixing layer was independent of the downstream position. The non-dimensional distance was the separation distance divided by the local shear layer thickness. The large scale structure observed in the experiment extended across the wind tunnel with spanwise irregularities. The author stated that the pairing interaction between adjacent vortices produced these irregularities.

A numerical study regarding the role of large vortex structures developed in two-dimensional shear layer was carried out by Aref and Siggia [10] using cloud-in-cell algorithm. The authors claimed that the increase in the mixing layer thickness is mainly due to the vortex structures scattered around the interface of the two mixing layers and the vortex pairing process plays a minor role in this. The regular stages of the vortex roll ups are shown in Figure 4.12.

a sequence of pictures showing the initial regular stages of roll-up of a vortex sheet.

During an experimental investigation on the developement of three-dimensional motion in the plane mixing layer by Bernal and Roshko [11], secondary streamwise vortex structures on the superimposed primary spanwise vortex structures were observed. Further investigation were carried out on the features of these secondary streamwise vortex structures. Figure 4.13 shows the sketch of the optical system where Shadowgraph and Schlieren flow-visualisation methods were used in the experiments. A two channel pressurized blowdown tunnel was used for the gas mixing-layer and the working section was confined in a high-pressure vessel, a regulator was used to maintain the pressure at the required level. Helium-nitrogen mixing layer was used to measure the effect of the secondary structure on the spanwise concentration field. From the investigation, measurements taken at several flow conditions revealed the spanwise vortex instability which generated the secondary streamwise vortex structures defined by the critical Reynolds number and the spanwise wavelength and the mean normalized wavelength is independent of velocity

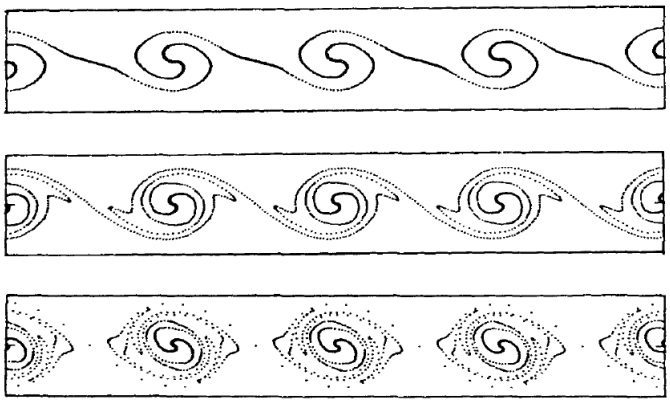

Figure 4.12: Vortical structures captured during the numerical study by Aref and Siggia [10]

ratio, initial shear-layer-profile shape and density ratio but the the critical Reynolds number was dependent of these parameters. A well defined spanwise entrainment pattern was produced by the spatial organization of the secondary structure and these measurements showed that the spanwise scale of the secondary structure increased with downstream distance of the mixing layer.

A three-dimensional stability analysis of a Kelvin-Helmholtz billow observed in a shear layer of two fluids with different densities was performed by Fontane and Joly [12]. Figure 4.15 shows the vorticity field captured during the investigation. Reynolds number was set to 1500 during the numerical simulation. The density contrast, C_ρ, a relevant measure of the inertia effects, was given by,

$$C_\rho = \frac{\Delta\rho}{2\rho_0} \text{ where } \Delta\rho = \rho_{upper} - \rho_{lower} \tag{4.25}$$

where the difference in the density, $\Delta\rho$, across the shear layer is given by,

$$\Delta\rho = \rho_{upper} - \rho_{lower} \tag{4.26}$$

and the mean density, ρ_0, is given by,

$$\rho_0 = \frac{\rho_{upper} + \rho_{lower}}{2} \tag{4.27}$$

4.4 Scientific Challenges

The compressible equations are difficult to solve for low Mach number flows which fall into the incompressible flow category. However according to Gustafsson and Stoor [40], Klainerman and

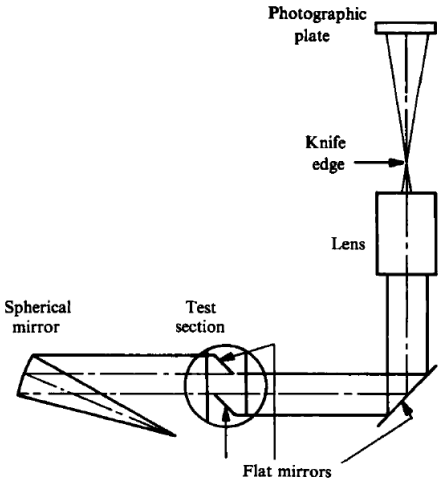

Figure 4.13: Schlieren optical system used by Bernal and Roshko [11] during the experimental investigation on streamwise vortex structure in the plane mixing layers

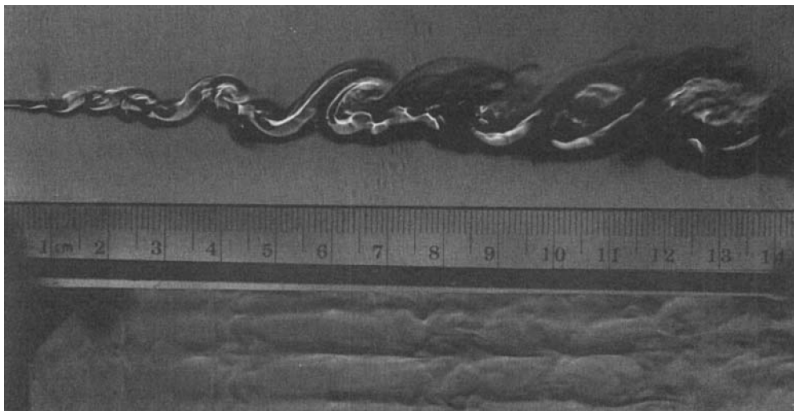

Figure 4.14: Instantaneous Schlieren picture of the helium-nitrogen mixing layer taken during the experimental investigation on streamwise vortex structure in the plane mixing layers by Bernal and Roshko [11]

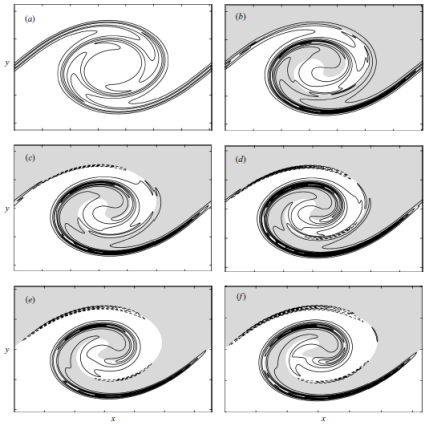

Figure 4.15: Vortical structures observed in the mixing layer with increasing density contrasts, (a) $C_\rho = 0$, (b) $C_\rho = 0.1$, (c) $C_\rho = 0.2$, (d) $C_\rho = 0.3$, (e) $C_\rho = 0.4$, (f) $C_\rho = 0.5$ during the stability analysis of variable density Kelvin–Helmholtz billow by Fontane and Joly [12]

Majda [41] and Kreiss *et al.* [42] the incompressible equations approximate the compressible equations.

Turkel *et al.* [43] explain the reasons for using the compressible equations in low Mach number flows as,

- The existing high order compressible codes can be used for low Mach number problems in complicated geometries
- Local regions with shocks while the flow is in the low Mach region
- In problems where the thermal effect is important and the energy equation is joined with other equations

The challenges in solving incompressible flows using compressible algorithms are mentioned in several journal papers and also the solutions in solving the low Mach flows to achieve accurate results with high order compressible methods. Some of the well known problems in solving low Mach number flows with mixed compressible and incompressible flows mentioned by various authors in their journal papers are summarised below.

Computation of incompressible vortical flows at low Mach numbers using compressible algorithms lead to three well known problems. These are summarised as problems due to poor accuracy, stiffness and cancellation. Stiffness can be addressed by appropriate preconditioning of the system, as detailed in Turkel [44] and subsequent authors. Turkel presents a unified theory of preconditioned methods which generalises the previous methods for both incompressible and slow compressible flows. The cancellation problem has been summarised and tackled in detail by Sesterhenn *et al.* [45] entirely focuses on cancellation of the numerical solution for the low Mach number flow computations by using modern finite volume methods. According to the authors the three operations that leads to cancellation in common finite volume methods for compressible

flows are the time integration, the time computation of the flux-difference and the computation of fluxes. The basic idea suggested in this article to overcome the cancellation problem is to introduce a reference state into the governing equation and calculate the perturbations to this state effectively, without ignoring any terms of the full original equations. Hence challenges with stiffness and cancellation can be met through appropriate preconditioning and organisation of the algorithm.

The accuracy problem is very important in the use of compressible algorithms in mixed compressible/incompressible flows. Volpe [46] showed the problems encountered in low Mach number computations using compressible algorithms. Three, two dimensional compressible algorithms were tested at low Mach numbers through two cases; inviscid steady flow over a circular cylinder, and impulsively started viscous flow over a cylinder. Two of the algorithms have finite volume discretisation along with a multistage time stepping. The difference in these two codes is that one of them uses the cell centred differencing scheme while the other code uses the node centred differencing scheme. In the third code the unsteady Navier-Stokes equations are solved by implicit finite difference method. In this investigation it is clearly demonstrated that the solution accuracy can be increased by reducing the mesh size for low Mach number simulations, however the error becomes progressively worse at lower Mach and the required grid levels prohibitively large.

The source of these inaccuracies stems from the behaviour of the compressible algorithms at low Mach number, including an increase of artificial viscosity which has been discussed in detail in several papers. Noh [47] investigates three types of artificial viscosity errors, (i) excess artificial viscosity heating, which can be split into two types: (a) excess wall heating on shock formation and (b) shockless artificial viscosity heating; (ii) artificial viscosity errors when shocks are propagated over a nonuniform mesh; and (iii) artificial viscosity errors in propagating shocks in spherical geometry. The examples showed serious artificial viscosity induced errors can be produced in the presence of strong shocks during the use of artificial viscosity methods of von Neumann and Richtmyer [48], which is a very useful method for capturing shockwaves in the flow on finite difference methods.

Guillard and Viozat [49, 50] explored the source of solution inaccuracies in low Mach number limit through one dimensional problems, proving that the solution of the discrete system contains pressure fluctuations of order of Mach number while the continuous pressure scales with Mach number square, and showed that appropriate preconditioning can recover the correct pressure scaling. This preconditioning is suitable for implicit methods, however when applied to explicit time stepping methods the stability region is restrictively small, especially at high grid resolutions.

The poor performance in accuracy of Godunov schemes at low Mach numbers is explained by Thornber *et al.* [51] by addressing the entropy generation and the corresponding dissipation of kinetic energy associated with high-resolution, shock-capturing methods. The authors also demonstrate that for general continuously varying flows the inherent numerical entropy increase of Godunov methods is proportional to the velocity jump squared, not velocity jump cubed as commonly assumed. The analysis is also applied to high-order accurate methods in space and time and all analytical results are validated with simple numerical experiments. In a subsequent publication, Thornber *et al.* [24] developed a simple, computationally efficient low Mach correction for any method of lines compressible Godunov-type algorithm. This low Mach correction is intended for use in flows with both compressible and low Mach number features, and can

be employed with explicit time stepping methods under the standard CFL criteria. A simple local modification is included to the reconstruction process which effectively removes the Mach number dependence of the leading order dissipation rate of kinetic energy, hence significantly improving the resolution of low Mach number portions of a compressible flow.

Rieper [52] proposes a low Mach number fix for Roe's approximate Riemann solver (LMRoe). The approach is demonstrated with the example of the Roe scheme which removes the accuracy problem of upwind schemes in the low-Mach number regime and the numerical results show that the accuracy of the LMRoe scheme is independent of the Mach number. According to the author this method can also be applied to other Godunov-type schemes, such as HLLC [22] and HLLEM [53] but this method adds too much artificial diffusion to the shear and entropy wave when applied to some upwind schemes such as HLL, Rusanov and van Leer flux splitting.

This thesis will explore the performance of classical and low Mach corrected numerical schemes, using four different codes and a new, well posed test case at a range of Mach numbers. A single mode Kelvin-Helmholtz instability test case was previously used to demonstrate that Godunov methods suffer from severe dissipation at lower Mach numbers [24]. In that case the initial condition was ill-posed in that it consisted of a perfectly sharp interface, hence was absolutely unstable. This new two mode Kelvin-Helmholtz test case is much better as it is well-posed, consisting of a smooth initial condition, regularised by viscosity, and thus the solution converges with grid refinement.

Chapter 5

Initial and Boundary Conditions

5.1 Initial Conditions

The initial conditions are based on the shear layer experiment where the velocities are $U_1 = 0.55$ (upper stream) and $U_2 = 1.55$ (lower stream), and ΔU is the difference of the two streams. The calculation is performed in a frame of reference moving with the mean stream velocity, $\bar{U} = 1.05$ and focuses on the evaluation of the large scale vortex from the two smaller vortices. The final structure has a wavelength which is equal to 6.

The Mach number, defined by $M = \Delta U/\sqrt{(\gamma p/\rho)}$ is adjusted by changing the background pressure to obtain the results for $M = 0.02$ and $M = 0.002$. The size of the computational region is $L \times L$ where $L = 1$. Density is fixed at $\rho = 1$ and $\gamma = 5/3$. The measured initial momentum thickness, $\Theta_0 = 0.03$. The Reynolds number, defined by $Re = (L\Delta U)/\nu$ for the flow is fixed at 1600 to match with the experiment by Winant and Browand [4].

In the unperturbed initial geometry, the unperturbed velocity, u in the x direction is given by,

$$u = -\frac{1}{2}\Delta U \tanh\left(\frac{z}{2\Theta_0}\right) \tag{5.1}$$

Initial velocity perturbations, u' and v' are used to initiate the vortex pairing process and a stream function, ψ is used to give a divergence-free initial velocity field. The sum of two Kelvin–Helmholtz instability eigenmodes is used [54]. The velocity perturbations, u' and v' are defined as,

$$u' = -\frac{\partial \psi}{\partial z} \text{ and } v' = \frac{\partial \psi}{\partial x} \tag{5.2}$$

where the stream function, ψ is defined as,

$$\psi = A_1(z)\frac{V_1}{k_1}\cos(k_1 x)e^{(-k_1|z|)} + A_2(z)\frac{V_2}{k_2}\cos(k_2 x)e^{(-k_2|z|)} \tag{5.3}$$

The wave numbers, k_1 and k_2 are defined as,

$$k_1 = \frac{2\pi}{L} \text{ and } k_2 = \frac{4\pi}{L} \tag{5.4}$$

and the amplitude as,

$$A_i = \frac{1 - e^{(-2k_i[\frac{1}{2}L - |z|])}}{1 - e^{(-k_i L)}} \tag{5.5}$$

The velocity fluctuations are found by differentiating the stream function, ψ with respect to z and x,

$$u' = -\frac{\partial \psi}{\partial z} \tag{5.6}$$

$$\begin{aligned} u' =& A_1(z)V_1 \cos(k_1 x)e^{(-k_1|z|)} \left[\frac{z}{|z|}\right] \\ &+ A_2(z)V_2 \cos(k_2 x)e^{(-k_2|z|)} \left[\frac{z}{|z|}\right] \\ &+ \frac{2V_1}{(1 - e^{-k_1 L})} \cos(k_1 x)e^{(-k_1|z|-L)} \left[\frac{z}{|z|}\right] \\ &+ \frac{2V_2}{(1 - e^{-k_2 L})} \cos(k_2 x)e^{(-k_2|z|-L)} \left[\frac{z}{|z|}\right] \end{aligned} \tag{5.7}$$

$$v' = \frac{\partial \psi}{\partial x} \tag{5.8}$$

$$v' = -A_1(z)V_1 \sin(k_1 x)e^{(-k_1|z|)} - A_2(z)V_2 \sin(k_2 x)e^{(-k_2|z|)} \tag{5.9}$$

Finally, the velocity amplitudes in the experiment are not known and here it is estimated. Hence the time taken for the vortex growth and pairing process do not match with the experiment time. The two velocity amplitudes, V_1 and V_2 used here are,

$$V_1 = 0.025\Delta U \quad \text{and } V_2 = 0.05\Delta U \tag{5.10}$$

Momentum thickness, Θ is utilised to quantify the width of the mixing layer, and is defined as,

$$\Theta = \int \frac{(U_1 - \bar{u})(\bar{u} - U_2)}{(U_1 - U_2)^2} \, \mathrm{d}z \tag{5.11}$$

5.2 Boundary Conditions

The boundary conditions for the test case are set as, periodic in the x direction and reflective in the z direction. The axis and flow directions as well as the computational length are described in Figure 5.1.

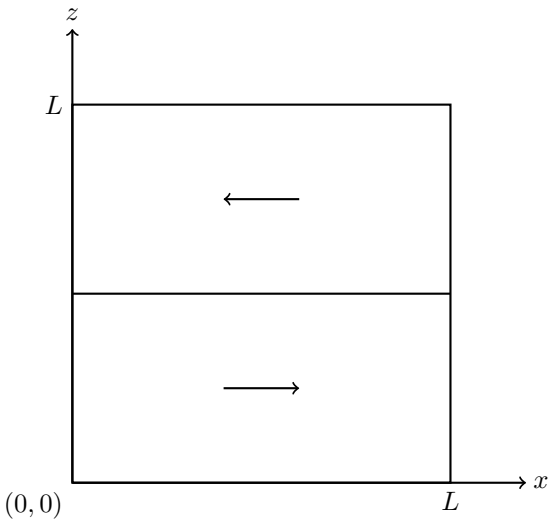

Figure 5.1: Description of the computational length and the directions of flow and axis

Chapter 6

Results and Discussion

6.1 Instability Development

The development of the Kelvin–Helmholtz instability captured at a converged grid level by the four non-commercial codes, 5^{th} order Godunov approach with the low Mach correction, 3^{rd} order accurate Lagrange-remap method, 5^{th} order wave propagation algorithm and 5^{th} order Godunov method with SLAU numerical flux, are shown in Figures 6.1 to 6.4 at four time instants.

Figure 6.1 shows the development of the Kelvin–Helmholtz instability growth captured by 5^{th} order Godunov approach with the low Mach correction. The results are obtained for Mach number at 0.2 on grid resolution of 64×64. The Figure illustrates the pairing process of the two small vortices becoming a single, larger structure as time progressed. The mode with the higher wavenumber, the second mode in this well posed, two dimensional two mode incompressible Kelvin–Helmholtz test case, grows faster compared to the first mode which has a wavenumber half the size of the second mode wavenumber. These two modes developed from the initial instability due to the perturbation continue to grow and form a single larger structure, a characteristic Kelvin–Helmholtz vortex. The mixing layer growth is controlled by the uninterrupted, repeating process of this vortex pairing and also responsible for the mixing of surrounding fluid.

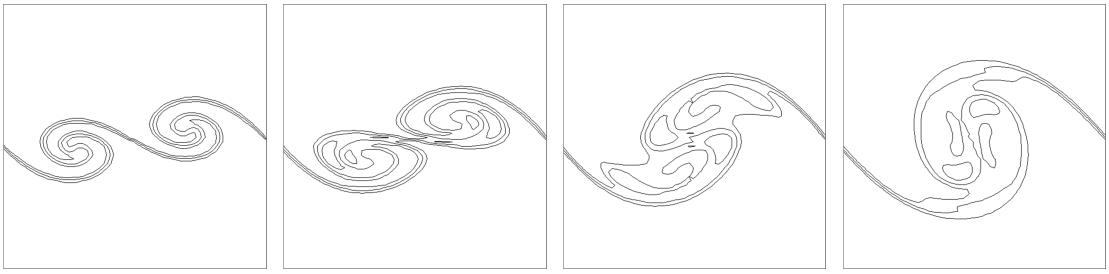

(a) t = 3s **(b)** t = 4s **(c)** t = 5s **(d)** t = 6s

Figure 6.1: Contour lines of volume fraction 0.25 to 0.75 for the instability development of the two mode Kelvin–Helmholtz test case captured by 5^{th} order Godunov approach with the low Mach correction for Mach number at 0.2 on grid resolution of 64×64

Figure 6.2 also illustrates the instability growth obtained by Lagrange-remap method at 64×64 grid resolution and Mach number of 0.2, and Figures 6.3 and 6.4 show the pairing process predicted using the two principal methods in `TRICLADE`, 5^{th} order wave propagation algorithm and 5^{th} order Godunov method with SLAU numerical flux, using same grid resolution and Mach number.

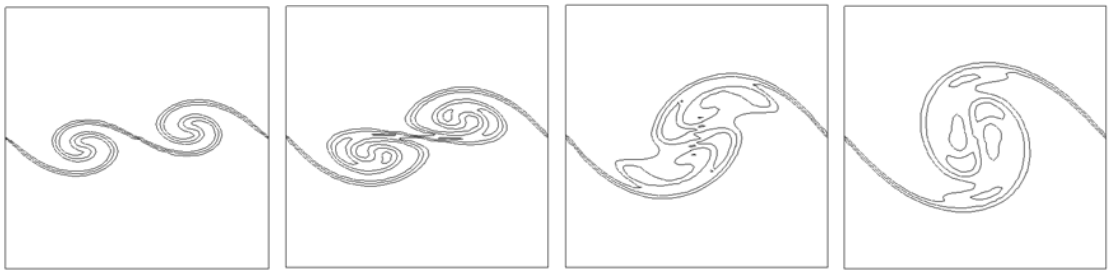

(a) t = 3s **(b)** t = 4s **(c)** t = 5s **(d)** t = 6s

Figure 6.2: Contour lines of volume fraction 0.25 to 0.75 for the instability development of the two mode Kelvin–Helmholtz test case captured by Lagrange-remap method for Mach number at 0.2 on grid resolution of 64×64

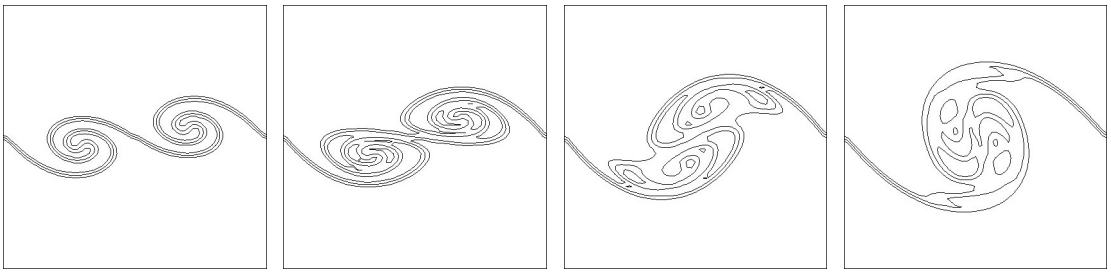

(a) t = 3s **(b)** t = 4s **(c)** t = 5s **(d)** t = 6s

Figure 6.3: Contour lines of volume fraction 0.25 to 0.75 for Mach number at 0.2 using `TRICLADE` with WP5 scheme (5^{th} order time-space accuracy, and MP limitation) on grid resolution of 64×64 [13]

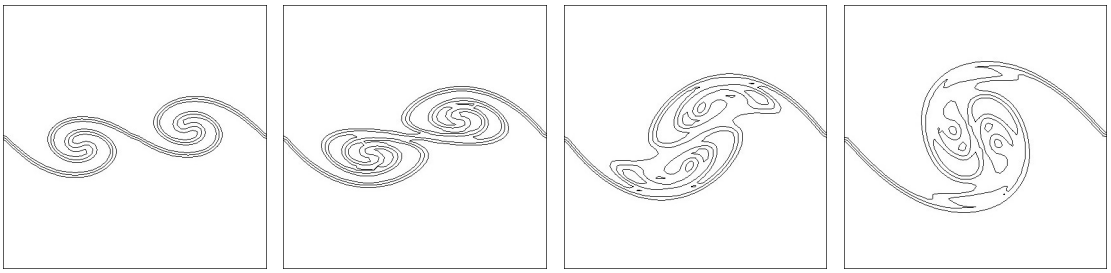

(a) t = 3s **(b)** t = 4s **(c)** t = 5s **(d)** t = 6s

Figure 6.4: Contour lines of volume fraction 0.25 to 0.75 for Mach number at 0.2 using `TRICLADE` with M5 Godunov scheme (5^{th} order space accuracy, 3^{rd} order time accuracy, and MP limitation) and SLAU flux on grid resolution of 64×64 [13]

The results obtained for the development of the Kelvin–Helmholtz instability on all four methods are very consistent. Two vortices develop first due to the initial high wavenumber instability (in accordance with Kelvin–Helmholtz instability theory). As the first long wavelength

mode begins to grown, these combine together as the time progress to form a single, larger vortex at $t = 6s$, the vortex pairing process.

The momentum thickness against time (dimensionless) results in Figure 6.5 due to the initial instability corresponds to the development of the Kelvin–Helmholtz vortices, captured by 5^{th} order Godunov approach with the low Mach correction, shown in Figure 6.1. This Figure illustrates the growth of the two modes clearly. The momentum thickness initially grows quickly as the 2^{nd} mode develops, then slows down due to non-linear saturation, and finally begins growing again as the 1^{st} mode emerges and pairing occurs.

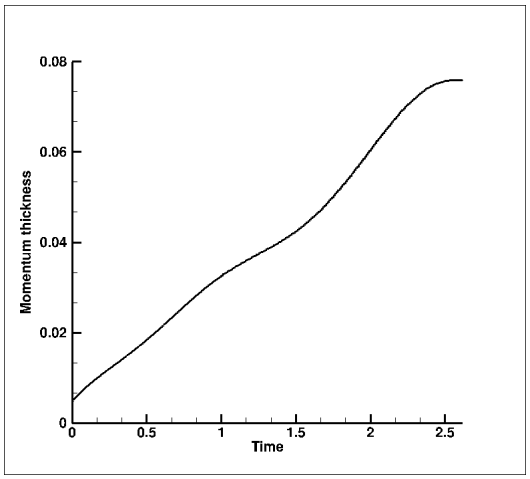

Figure 6.5: Momentum thickness against time (dimensionless) results obtained for 5^{th} order Godunov scheme with low Mach number correction feature on grid resolution of 64×64 for the instability development of the two mode Kelvin–Helmholtz test case for Mach number at 0.2

6.2 Grid Convergence

Grid convergence or mesh refinement is a straight forward method to test the convergence of the numerical scheme. The grid convergence of the non-commercial codes are tested on four different grid resolutions, 24×24, 32×32, 48×48 and 64×64, for all Mach numbers, 0.2, 0.02 and 0.002.

In order to demonstrate the grid convergence the Kelvin–Helmholtz instability growth is simulated by the 5^{th} order Godunov approach with the low Mach correction on four different grid resolutions, 24×24, 32×32, 48×48 and 64×64, for all Mach numbers, 0.2, 0.02 and 0.002. Figure 6.6 shows the momentum thickness against time (dimensionless) of the mixing layer developed by the Kelvin–Helmholtz instability growth by 5^{th} order Godunov approach with the low Mach correction. For all Mach numbers, 0.2, 0.02 and 0.002, the solution converges from grid resolution of 48×48. The Figure also shows initial quick growth of the momentum thickness as the second mode develops, then the growth slows down due to non-linear saturation. Finally the momentum thickness starts growing again as the first mode emerges and pairing occurs.

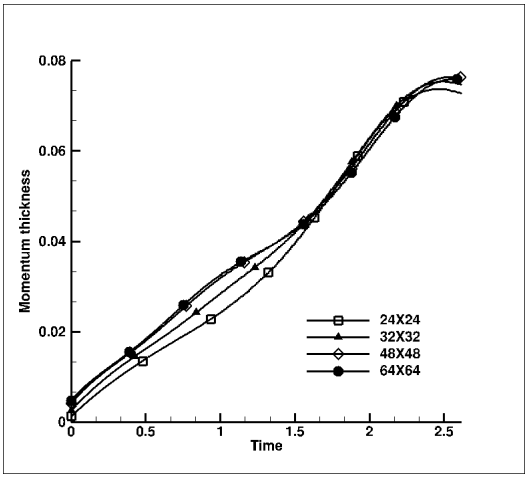

(a) M = 0.2

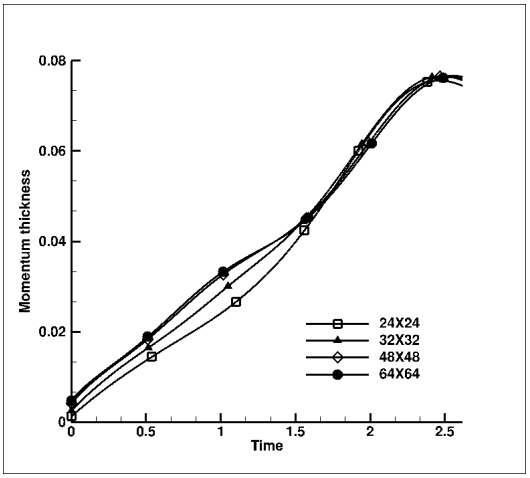

(b) M = 0.02

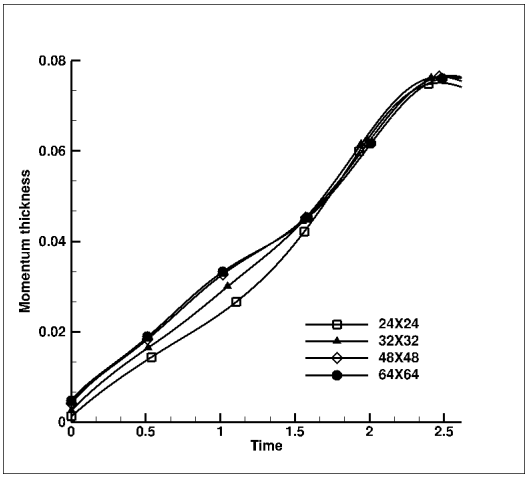

(c) M = 0.002

Figure 6.6: Momentum thickness against time (dimensionless) results obtained for 5^{th} order Godunov scheme with low Mach number correction feature on grid resolutions of 24×24, 32×32, 48×48 and 64×64 for the instability development of the two mode Kelvin–Helmholtz test case for Mach numbers at 0.2, 0.02 and 0.002

Figure 6.7 shows the mixing layer growth predicted by 3^{rd} order accurate Lagrange-remap method on grid resolutions of 24×24, 32×32, 48×48 and 64×64 for Mach number 0.2. The solution converges from grid resolution of 48×48.

The Kelvin–Helmholtz instability growth simulated by the 5^{th} order wave propagation algorithm is shown in Figure 6.8 for all grid resolutions and all Mach numbers. For Mach number 0.2 the solution converges from grid resolution of 48×48 but as the Mach number is reduced the results become dissipative.

The grid converged results obtained by 5^{th} order Godunov method with SLAU numerical flux for all Mach numbers, 0.2, 0.02 and 0.002, on all grid resolutions, 24×24, 32×32, 48×48 and 64×64, are shown in Figure 6.9. The solution converges from grid resolution of 48×48 for all

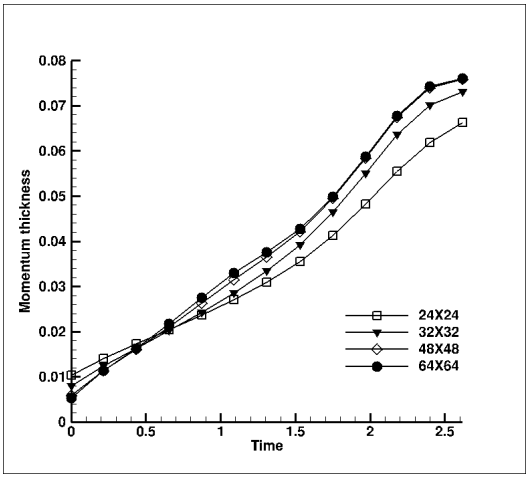

Figure 6.7: Momentum thickness against time (dimensionless) results obtained for Lagrange-remap method on grid resolutions of 24×24, 32×32, 48×48 and 64×64 for the instability development of the two mode Kelvin–Helmholtz test case for Mach number at 0.2

Mach numbers. These results are similar to the grid converged solution of 5^{th} order Godunov approach with the low Mach correction, shown in Figure 6.6.

Table 6.1 shows the final difference in the converged momentum thickness value as a percentage at $t = 6$s for all the grid resolutions when compared with the highest grid resolution of 64×64. These converged values of mixing layer thicknesses are obtained using the 5^{th} order Godunov scheme with low Mach number correction feature for all Mach numbers, 0.2, 0.02 and 0.002 on grid resolutions 24×24, 32×32, 48×48 and 64×64. As mentioned before from the momentum thickness against time in Figure 6.6 for all Mach numbers, 0.2, 0.02 and 0.002, the solution converges from grid resolution of 48×48. The tables also illustrate that the final mixing layer thickness at grid resolution of 48×48 is very close to the higher grid resolution used in this test case, 64×64, hence the solution converges at this resolution.

6.3 Mach Number Effects on Numerical Schemes

This section explores the behaviour of the non-commercial codes in the low Mach region during the development of the Kelvin–Helmholtz instability at a converged grid level. The results are obtained for Mach numbers of 0.02 and 0.002 with 5^{th} order Godunov approach, 5^{th} order wave propagation algorithm and 5^{th} order Godunov method with SLAU numerical flux.

6.3.1 Godunov Approach with and without Low Mach Correction

The low Mach correction proposed by Thornber *et al.* [24] which is implemented in 5^{th} order Godunov approach, is to improve performance at low Mach number regions in turbulent flows. The performance of the low Mach correction in the low Mach regions is demonstrated by capturing the development of the Kelvin–Helmholtz instability on all grid resolutions and for all low Mach numbers and compared against the results obtained using 5^{th} order Godunov approach without the low Mach correction feature.

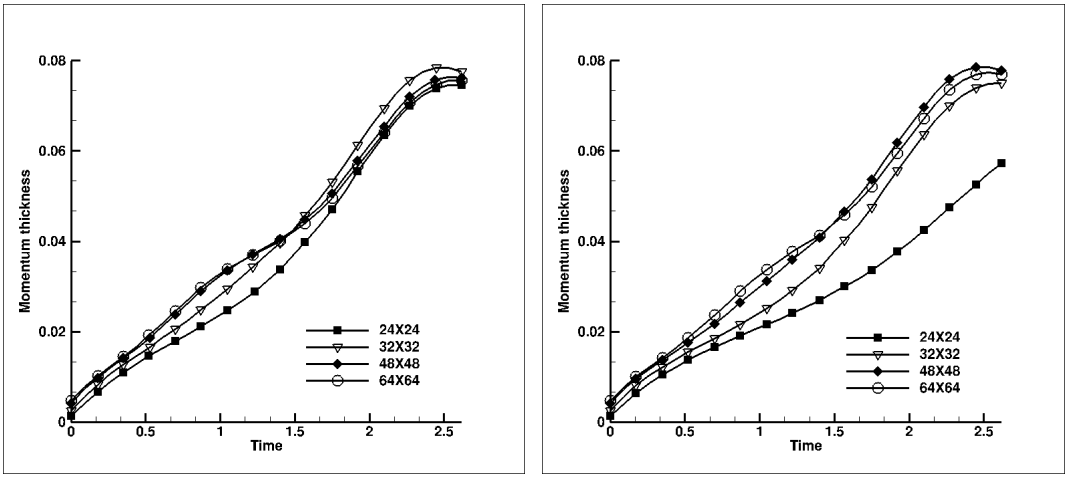

(a) M = 0.2 **(b)** M = 0.02

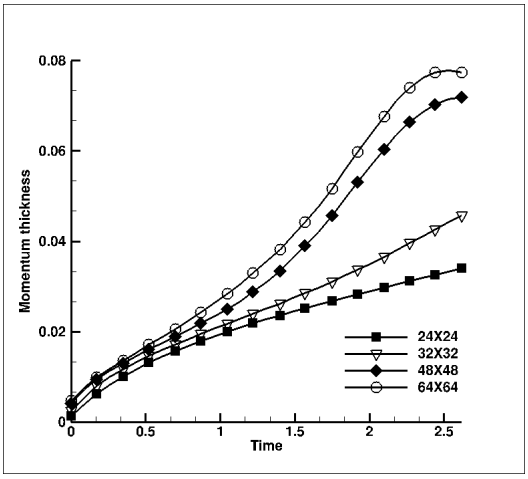

(c) M = 0.002

Figure 6.8: Momentum thickness against time (dimensionless) results obtained for `TRICLADE` with WP5 scheme (5^{th} order time-space accuracy, and MP limitation) on grid resolutions of 24×24, 32×32, 48×48 and 64×64 for the instability development of the two mode Kelvin–Helmholtz test case for Mach numbers at 0.2, 0.02 and 0.002

6.3.1.1 With Low Mach Number Correction

The ability of the 5^{th} order Godunov approach with the low Mach correction in capturing the Kelvin–Helmholtz instability growth in the low Mach number region is demonstrated by the observed vortex pairing results in Figures 6.10 and 6.11. These results are obtained for Mach numbers 0.02 and 0.002 on 64×64 grid resolution. The results obtained for Mach numbers 0.2, 0.02 and 0.002 in Figures 6.1, 6.10 and 6.11 respectively indicates that the numerical scheme, 5^{th} order Godunov approach with the low Mach correction, is predicting a Mach independent structure as the Mach number decreases. This prediction of the Mach independent structure

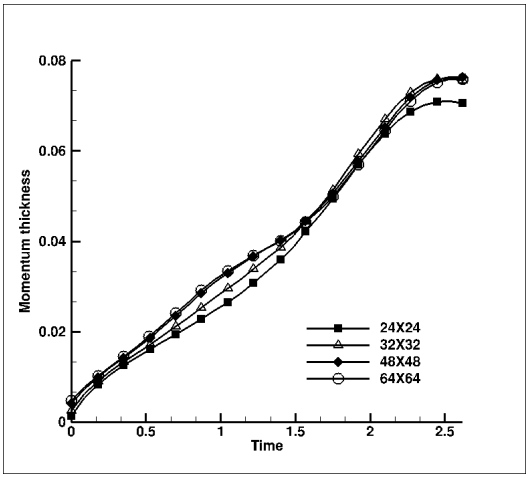

(a) M = 0.2

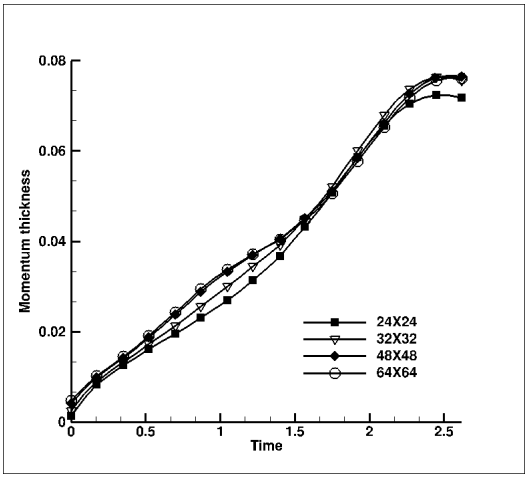

(b) M = 0.02

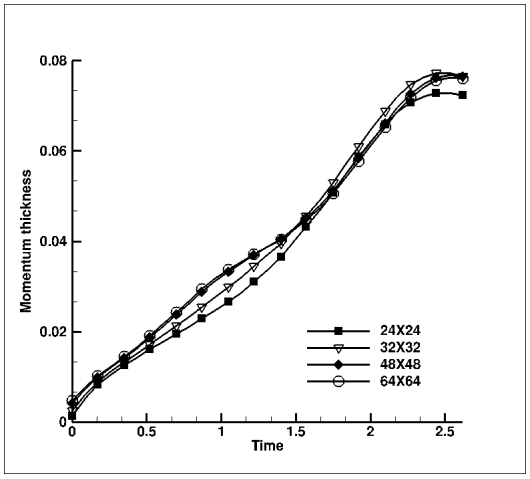

(c) M = 0.002

Figure 6.9: Momentum thickness against time (dimensionless) results obtained for `TRICLADE` with M5 Godunov scheme (5^{th} order space accuracy, 3^{rd} order time accuracy, and MP limitation) and SLAU flux on grid resolutions of 24×24, 32×32, 48×48 and 64×64 for the instability development of the two mode Kelvin–Helmholtz test case for Mach numbers at 0.2, 0.02 and 0.002

is clearly demonstrated in Figure 6.12. The momentum thickness against time (dimensionless) result captured on 64×64 grid resolution for Mach numbers at 0.2, 0.02 and 0.002 in Figure 6.12 shows the mixing of the surrounding fluid due to the growth of the Kelvin–Helmholtz instability. In each case, Mach numbers at 0.2, 0.02 and 0.002, the amount of the fluid mixing is identical regardless of the Mach number.

Figure 6.13 illustrates the momentum thickness against time (dimensionless) results obtained for all grid resolutions, 24×24, 32×32, 48×48 and 64×64, for each Mach number, 0.2, 0.02 and 0.002, by using 5^{th} order Godunov scheme with low Mach number correction. In each case the

Table 6.1: The final grid converged value as a percentage for each grid resolution using the high grid resolution, 64×64, as the reference value for all Mach numbers 0.2, 0.02 and 0.002 using 5^{th} order Godunov scheme with low Mach number correction feature

Mach number	*Grid resolution*	*Momentum thickness* (%)
0.2	24×24	95.90
	32×32	98.41
	48×48	99.59
	64×64	100.0
0.02	24×24	97.74
	32×32	99.30
	48×48	99.74
	64×64	100.0
0.002	24×24	97.38
	32×32	99.15
	48×48	99.68
	64×64	100.0

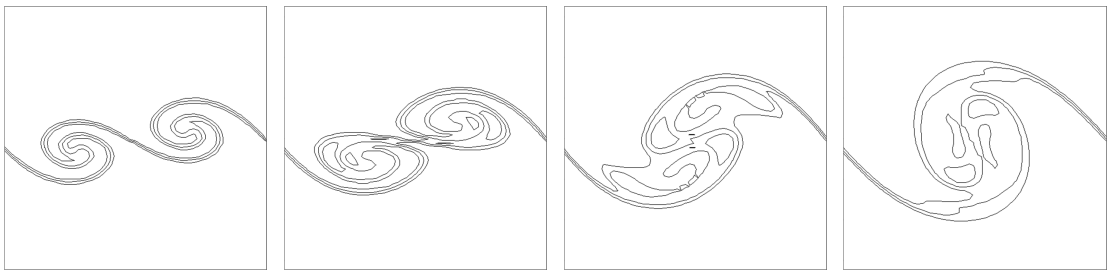

(a) t = 3s **(b)** t = 4s **(c)** t = 5s **(d)** t = 6s

Figure 6.10: Contour lines of volume fraction 0.25 to 0.75 for the instability development of the two mode Kelvin–Helmholtz test case captured by 5^{th} order Godunov approach with the low Mach correction for Mach number at 0.02 on grid resolution of 64×64

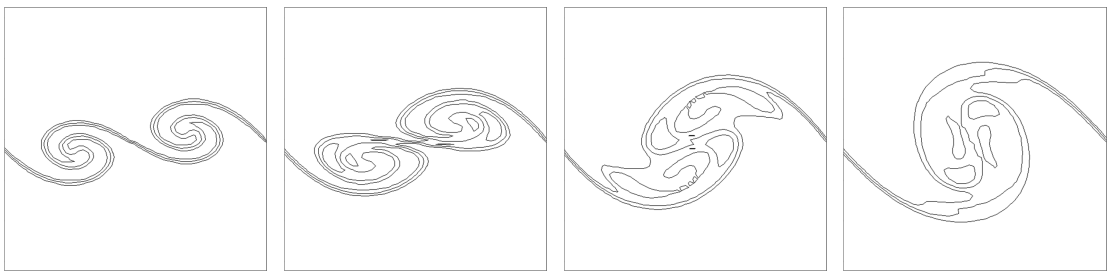

(a) t = 3s **(b)** t = 4s **(c)** t = 5s **(d)** t = 6s

Figure 6.11: Contour lines of volume fraction 0.25 to 0.75 for the instability development of the two mode Kelvin–Helmholtz test case captured by 5^{th} order Godunov approach with the low Mach correction for Mach number at 0.002 on grid resolution of 64×64

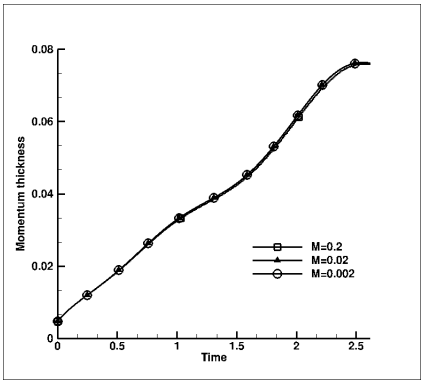

Figure 6.12: Momentum thickness against time (dimensionless) results obtained for 5^{th} order Godunov scheme with low Mach number correction feature on grid resolution of 64×64 for the instability development of the two mode Kelvin–Helmholtz test case for Mach numbers at 0.2, 0.02 and 0.002

solution is converged from grid resolution of 48×48. The results also show that for each Mach number, 0.2, 0.02 and 0.002, on grid resolutions of 48×48 and 64×64 the momentum thickness initially grows quickly as the 2^{nd} mode develops, then slows down due to non-linear saturation, and finally begins growing again as the 1^{st} mode emerges and pairing occurs.

6.3.1.2 Without low Mach Number Correction

The Kelvin–Helmholtz instability growth captured on a 64×64 grid resolution for Mach number of 0.2 by 5^{th} order Godunov approach without the low Mach correction is shown in Figure 6.14. The Figure illustrates the development of the two vortices and the pairing process as the time progresses and also the ability of the scheme, 5^{th} order Godunov approach, in capturing the Kelvin–Helmholtz instability growth without the recently proposed low Mach correction feature for Mach number of 0.2. The observed instability growth, without the low Mach number correction, in Figure 6.14 can be compared with the instability growth observed in Figure 6.1 which is obtained with the low Mach correction feature. These two Figures, 6.1 and 6.14, illustrate the ability of the scheme in capturing the Kelvin–Helmholtz instability growth for Mach number of 0.2 without the low Mach correction feature implemented in the 5^{th} order Godunov approach.

Figures 6.15 and 6.16 demonstrates the accuracy problem suffered by the Godunov-type schemes. The results for observed vortex pairing process, Figures 6.15 and 6.16, are obtained for Mach numbers of 0.02 and 0.002 respectively by using the 5^{th} order Godunov approach without the recently proposed low Mach correction on grid resolution of 64×64. Comparing the results obtained without low Mach correction for Mach number 0.2 (Figure 6.14) with Mach numbers of 0.02 and 0.002 (Figures 6.15 and 6.16) it is possible to come to the conclusion that the Godunov-type schemes suffer from an accuracy problem in the low Mach number regime which is below 0.2 as the excessive dissipation has prevented the growth of the Kelvin–Helmholtz instability.

The inability of the 5^{th} order Godunov scheme in capturing the Kelvin–Helmholtz instability growth at low Mach numbers is illustrated in Figure 6.17 for all grid resolutions, 24×24, 32×32, 48×48 and 64×64. As the Mach number is reduced the excessive dissipation prevents Kelvin–Helmholtz instability growth. Below Mach number of 0.2 the results become more dissipative

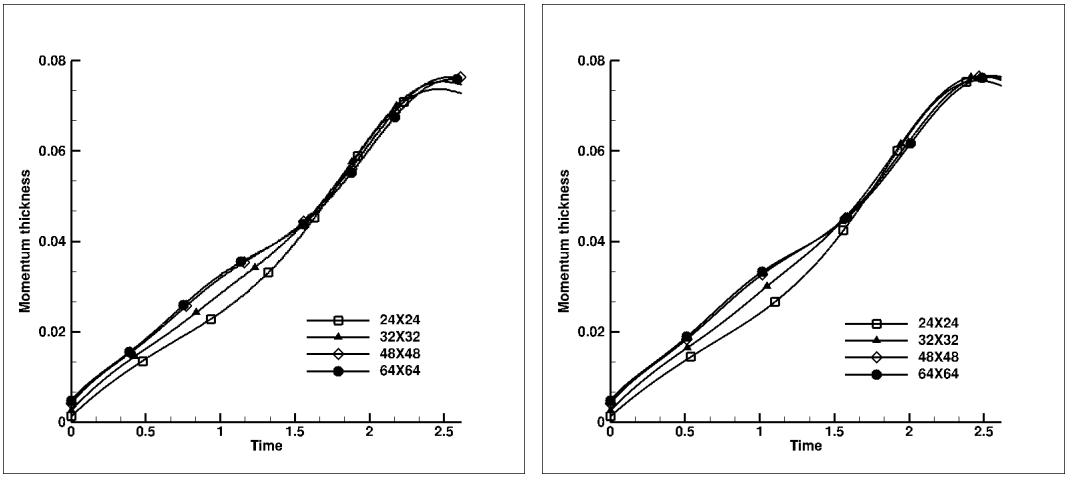

(a) M = 0.2 **(b)** M = 0.02

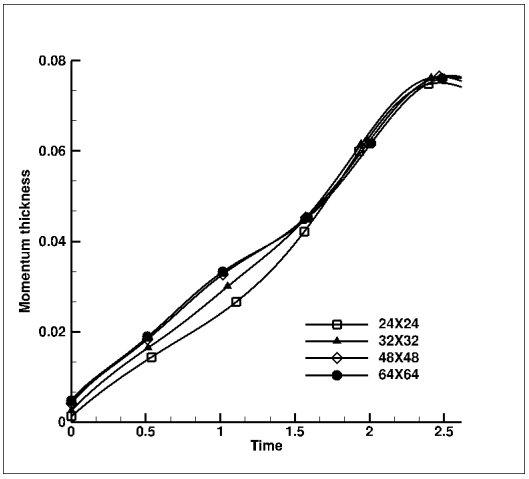

(c) M = 0.002

Figure 6.13: Momentum thickness against time (dimensionless) results obtained for 5^{th} order Godunov scheme with low Mach number correction feature on grid resolutions of 24×24, 32×32, 48×48 and 64×64 for the instability development of the two mode Kelvin–Helmholtz test case for Mach numbers at 0.2, 0.02 and 0.002

in the 5^{th} order Godunov scheme. This Figure also illustrates the accuracy problem suffered by the Godunov-type schemes in the low Mach number region.

The results become dissipative as the Mach number is reduced in the 5^{th} order Godunov scheme without the low Mach correction. By comparing the results, with and without the low Mach correction, the need for specifically designed low Mach correction in Godunov-based techniques is clearly demonstrated.

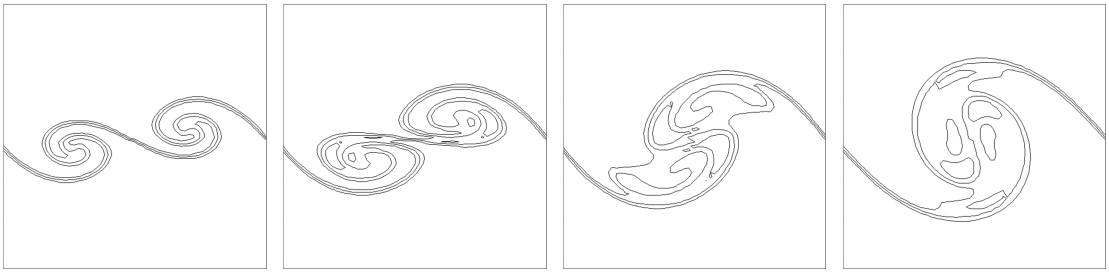

(a) t = 3s **(b)** t = 4s **(c)** t = 5s **(d)** t = 6s

Figure 6.14: Contour lines of volume fraction 0.25 to 0.75 for the instability development of the two mode Kelvin–Helmholtz test case captured by 5^{th} order Godunov approach without the low Mach correction for Mach number at 0.2 on grid resolution of 64×64

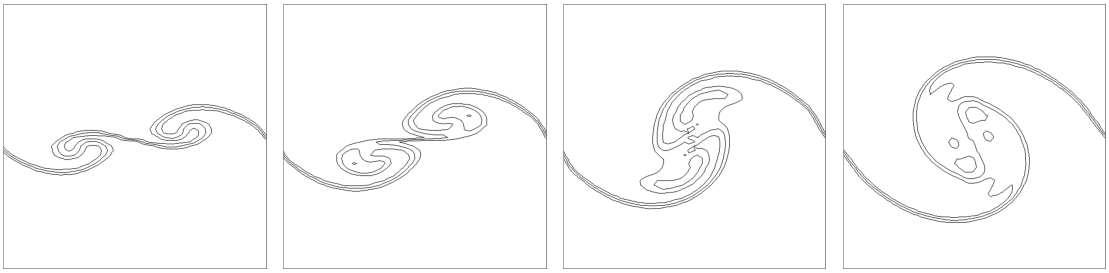

(a) t = 3s **(b)** t = 4s **(c)** t = 5s **(d)** t = 6s

Figure 6.15: Contour lines of volume fraction 0.25 to 0.75 for the instability development of the two mode Kelvin–Helmholtz test case captured by 5^{th} order Godunov approach without the low Mach correction for Mach number at 0.02 on grid resolution of 64×64

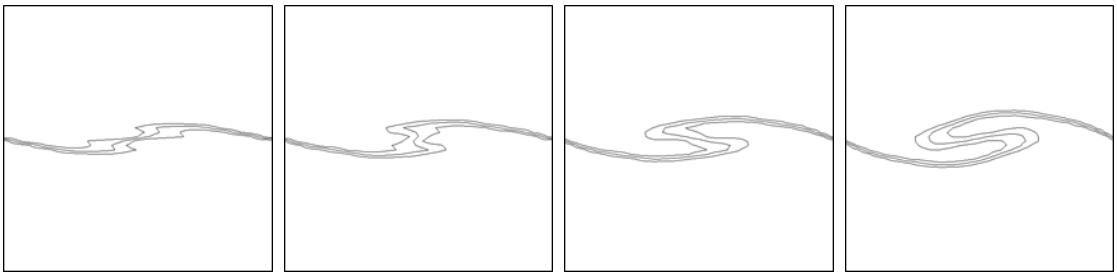

(a) t = 3s **(b)** t = 4s **(c)** t = 5s **(d)** t = 6s

Figure 6.16: Contour lines of volume fraction 0.25 to 0.75 for the instability development of the two mode Kelvin–Helmholtz test case captured by 5^{th} order Godunov approach without the low Mach correction for Mach number at 0.002 on grid resolution of 64×64

6.3.2 Wave Propagation Algorithm

Figures 6.18 and 6.19 show instability development captured by the 5^{th} order accurate in space and time finite difference type method based on the wave propagation algorithm for Mach num-

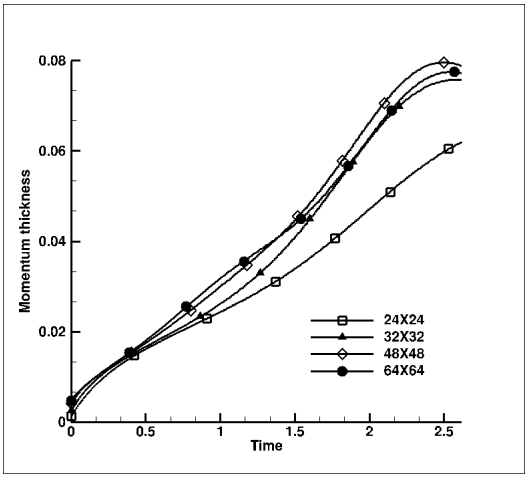

(a) M = 0.2

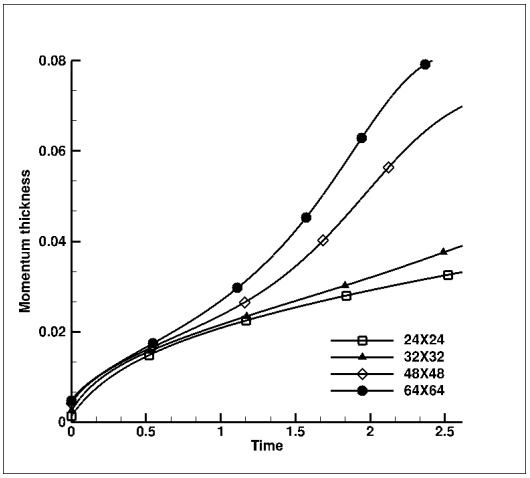

(b) M = 0.02

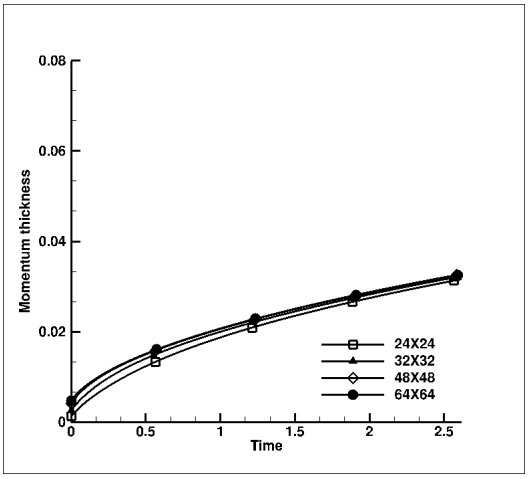

(c) M = 0.002

Figure 6.17: Momentum thickness against time (dimensionless) results obtained for 5^{th} order Godunov scheme without low Mach number correction feature on grid resolutions of 24×24, 32×32, 48×48 and 64×64 for the instability development of the two mode Kelvin–Helmholtz test case for Mach numbers at 0.2, 0.02 and 0.002

bers of 0.02 and 0.002 on grid resolution of 64×64.

Figure 6.20, mixing layer growth against time (dimensionless), shows the inability of the scheme, 5^{th} order wave propagation algorithm, in low Mach number regions for all grid resolutions. The scheme fails to capture the Kelvin–Helmholtz instability growth accurately for low Mach number of 0.02 particularly on lower grid resolutions. As the Mach number is reduced further, 0.002, the numerical dissipation prevents the growth of the Kelvin–Helmholtz instability and behaves poorly on all grid resolutions. These results show the 5^{th} order accurate in space and time finite difference type method based on the wave propagation algorithm suffers from over dissipation at low Mach numbers. However, it performs better than the standard Godunov

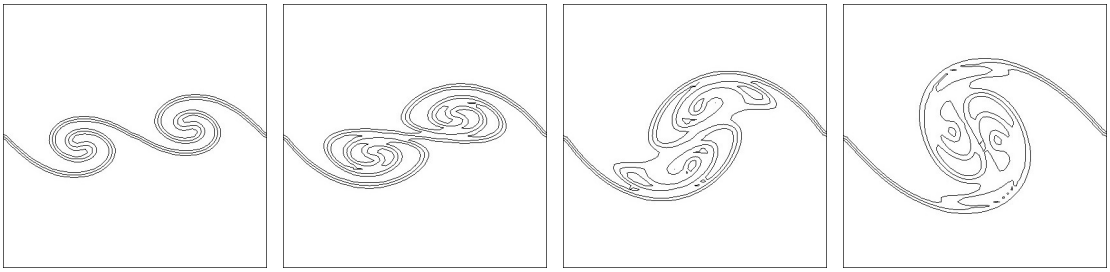

(a) t = 3s **(b)** t = 4s **(c)** t = 5s **(d)** t = 6s

Figure 6.18: Contour lines of volume fraction 0.25 to 0.75 for Mach number at 0.02 using `TRICLADE` with WP5 scheme (5^{th} order time-space accuracy, and MP limitation) on grid resolution of 64×64 [13]

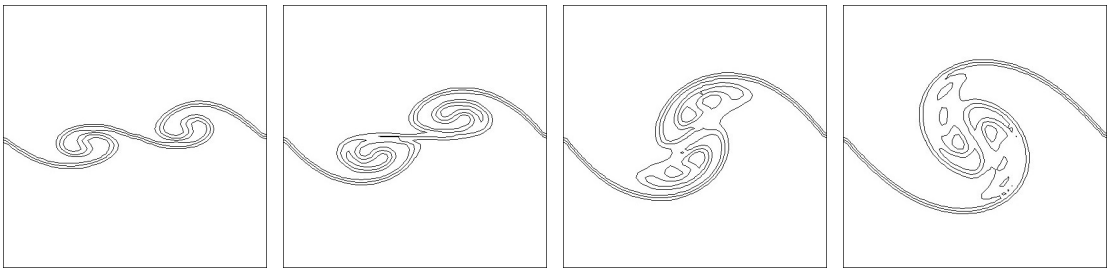

(a) t = 3s **(b)** t = 4s **(c)** t = 5s **(d)** t = 6s

Figure 6.19: Contour lines of volume fraction 0.25 to 0.75 for Mach number at 0.002 using `TRICLADE` with WP5 scheme (5^{th} order time-space accuracy, and MP limitation) on grid resolution of 64×64 [13]

method indicating that the levels of artificial dissipation do not increase as strongly with Mach number decreases.

6.3.3 Godunov Method with SLAU Numerical Flux

The ability of the finite volume 5^{th} order Godunov method with the SLAU numerical flux to capture development of the Kelvin–Helmholtz instability has been tested in the low Mach regions on all grid resolutions used in this test case. Figures 6.21 and 6.22 show the development of the Kelvin–Helmholtz instability obtained for Mach numbers of 0.02 and 0.002 on 64×64 grid resolution respectively.

Together with the SLAU numerical flux, the Gudunov method performs well by capturing the instability growth in the low Mach region due to the low Mach capture property of SLAU numerical flux. The observed results in Figures 6.21 and 6.22 are identical to the grid converged solutions by 5^{th} order Godunov scheme with low Mach number correction for Mach numbers of 0.02 and 0.002.

Figure 6.23, momentum thickness against time (dimensionless), shows the ability of the 5^{th} order Godunov method together with SLAU numerical flux in capturing the Kelvin–Helmholtz instability growth in the low Mach number region on all grid resolutions. Comparing these

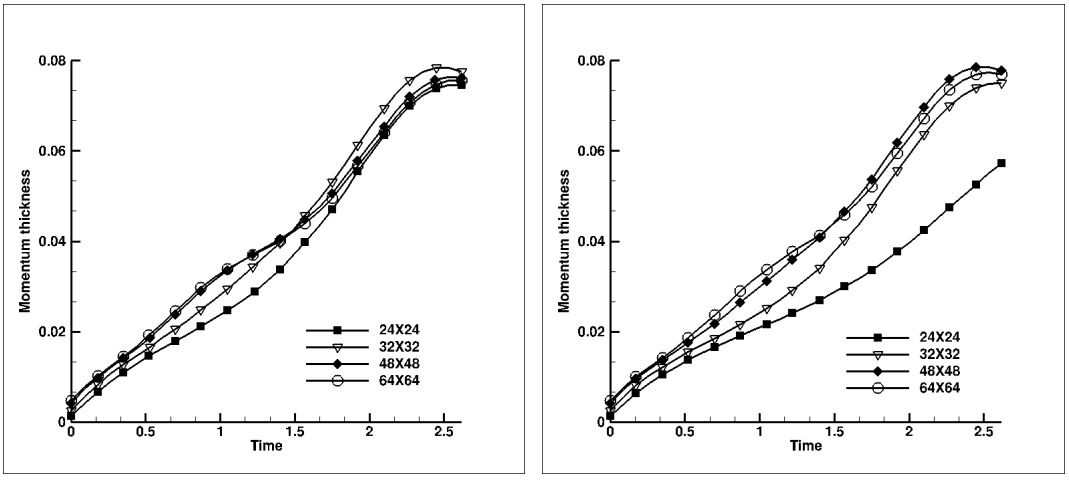

(a) M = 0.2 **(b)** M = 0.02

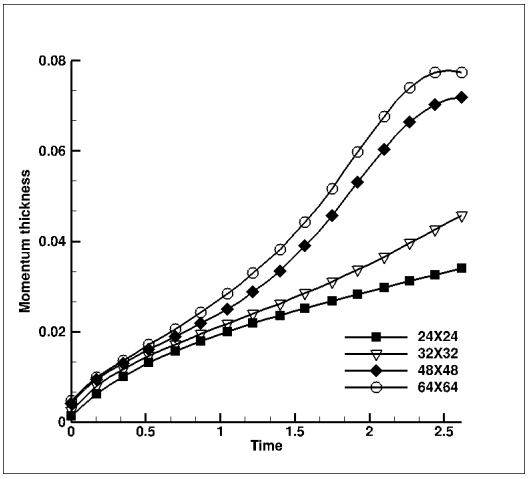

(c) M = 0.002

Figure 6.20: Momentum thickness against time (dimensionless) results obtained for `TRICLADE` with WP5 scheme (5^{th} order time-space accuracy, and MP limitation) on grid resolutions of 24×24, 32×32, 48×48 and 64×64 for the instability development of the two mode Kelvin–Helmholtz test case for Mach numbers at 0.2, 0.02 and 0.002

results with the 5^{th} order Godunov approach with low Mach correction, Figure 6.10, reveals the consistent of the two numerical schemes in capturing the development of the Kelvin–Helmholtz instability for all Mach numbers. In both numerical schemes, 5^{th} order Godunov approach with low Mach correction and 5^{th} order Godunov method together with SLAU numerical flux, the momentum thickness initially grows quickly as the second mode develops, then slows down due to non-linear saturation, and finally begins growing again as the first mode emerges and pairing occurs. The growth of the 2^{nd} mode is not captured accurately on 24×24 and 32×32 grid resolutions as done on grid resolution of 48×48 and 64×64 by both numerical schemes. However the first mode still emerges at late time for both numerical schemes on all grid resolutions.

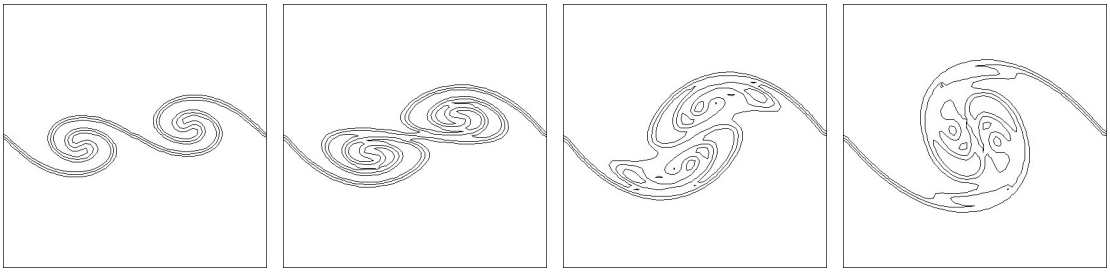

(a) t = 3s **(b)** t = 4s **(c)** t = 5s **(d)** t = 6s

Figure 6.21: Contour lines of volume fraction 0.25 to 0.75 for Mach number at 0.02 using `TRICLADE` with M5 Godunov scheme (5^{th} order space accuracy, 3^{rd} order time accuracy, and MP limitation) and SLAU flux on grid resolution of 64×64 [13]

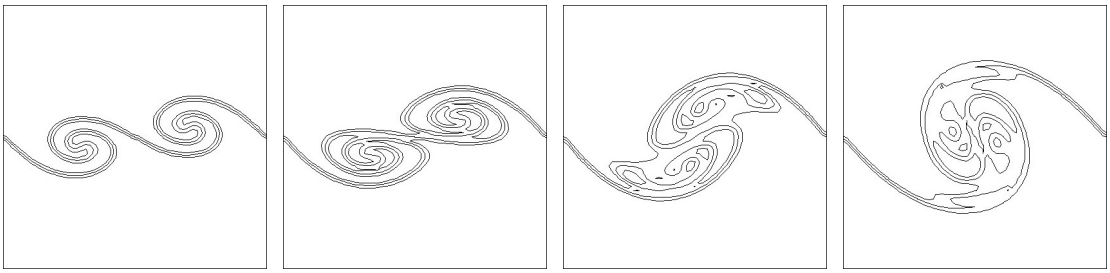

(a) t = 3s **(b)** t = 4s **(c)** t = 5s **(d)** t = 6s

Figure 6.22: Contour lines of volume fraction 0.25 to 0.75 for Mach number at 0.002 using `TRICLADE` with M5 Godunov scheme (5^{th} order space accuracy, 3^{rd} order time accuracy, and MP limitation) and SLAU flux on grid resolution of 64×64 [13]

6.4 Influence of Order of Accuracy - Godunov Scheme with Low Mach Number Correction

The influence of order of accuracy is highlighted by using the 2^{nd} and 5^{th} order Godunov scheme with low Mach number correction. The development of the Kelvin–Helmholtz instability is simulated by 2^{nd} and 5^{th} order methods on all grid resolutions and for all Mach numbers used in the present test case.

Figures 6.24, 6.25 and 6.26 show 2^{nd} and 5^{th} order results obtained by using Godunov scheme with low Mach number correction on grid resolutions of 24×24, 32×32, 48×48 and 64×64 for Mach numbers of 0.2, 0.02 and 0.002 respectively. In the 5^{th} order Godunov scheme MUSCL reconstruction is implemented and whereas 2^{nd} order uses van Leer. In terms of computational cost 5^{th} order Godunov scheme is slightly more expensive than the 2^{nd} order Godunov scheme but both 2^{nd} and 5^{th} order schemes are restricted by the bottleneck of the computational memory as during the simulations only one processor is used. Since both 2^{nd} and 5^{th} schemes have the same computational requirements. As the mesh is refined the 2^{nd} and 5^{th} order results converge at grid resolution of 48×48. The differences between 2^{nd} and 5^{th} order accurate Godunov method with low Mach correction are no longer as pronounced. Therefore 2^{nd} order can

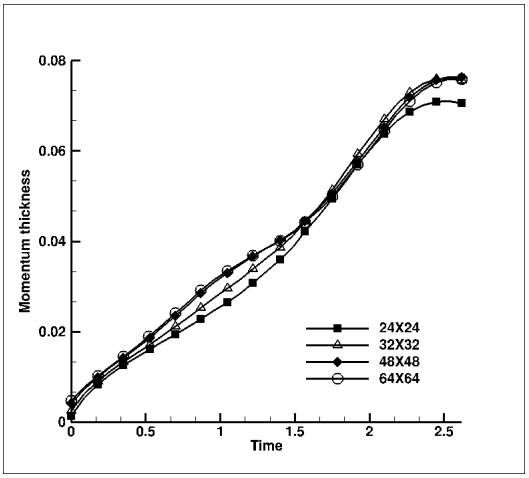

(a) M = 0.2

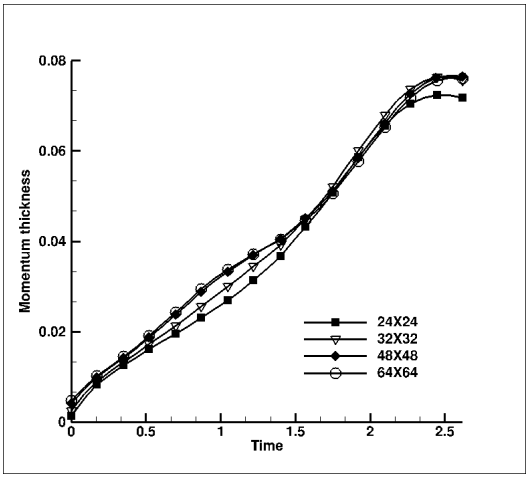

(b) M = 0.02

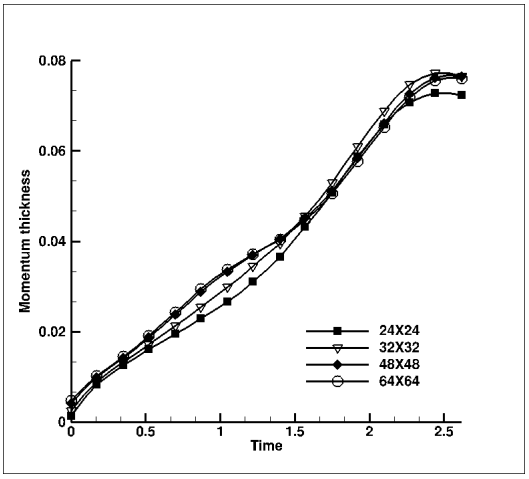

(c) M = 0.002

Figure 6.23: Momentum thickness against time (dimensionless) results obtained for `TRICLADE` with M5 Godunov scheme (5^{th} order space accuracy, 3^{rd} order time accuracy, and MP limitation) and SLAU flux on grid resolutions of 24×24, 32×32, 48×48 and 64×64 for the instability development of the two mode Kelvin–Helmholtz test case for Mach numbers at 0.2, 0.02 and 0.002

be applied to existing compressible Godunov schemes in incompressible simulation of low Mach number limit with only a relatively minor penalty. This also indicates that this method can be applied retrospectively to all current 2^{nd} order Godunov methods to give improved performance, a particularly important observation for unstructured codes where gaining a very high order of accuracy may be computationally prohibitive.

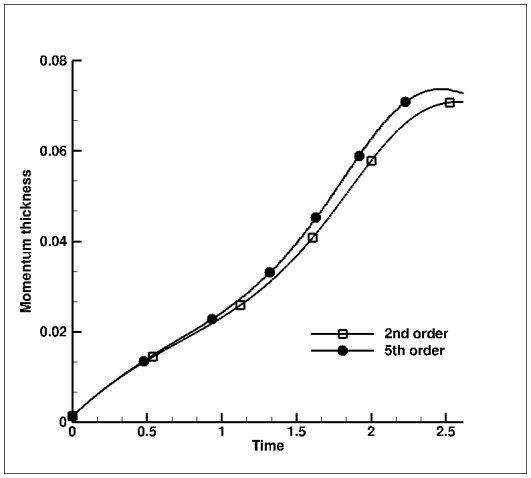

(a) 24×24

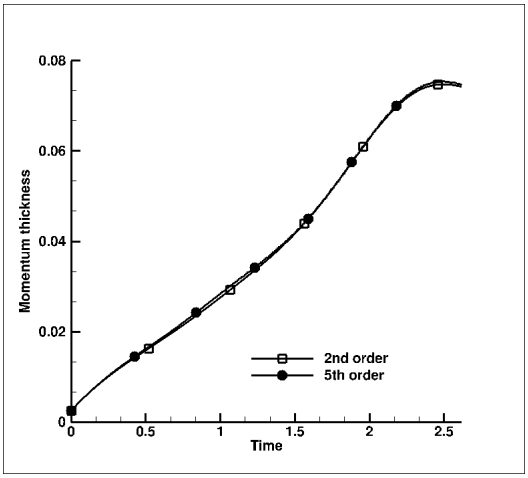

(b) 32×32

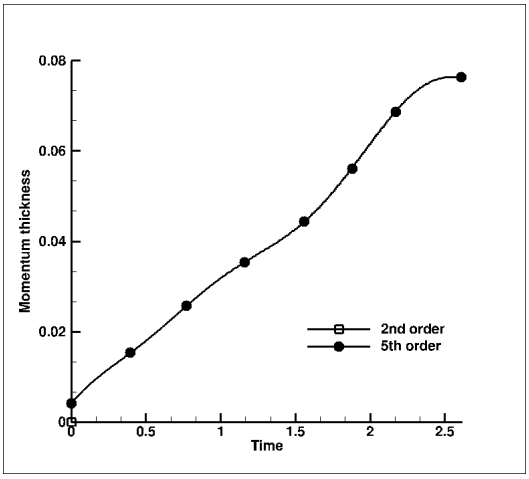

(c) 48×48

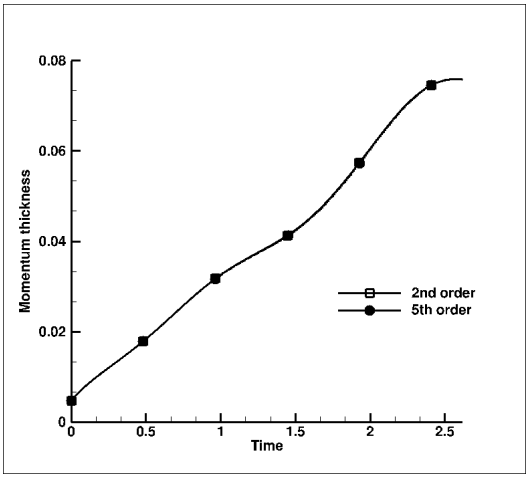

(d) 64×64

Figure 6.24: Momentum thickness against time (dimensionless) results obtained for 2^{nd} and 5^{th} order Godunov scheme with low Mach number correction feature on grid resolutions of 24×24, 32×32, 48×48 and 64×64 for the instability development of the two mode Kelvin–Helmholtz test case for Mach number at 0.2

6.5 Zero Perturbation

Figure 6.27 shows the comparison between the momentum thickness against time (dimensionless) results obtained without the low Mach correction and without perturbations using the 5^{th} order Godunov scheme for all three different Mach numbers used in the test case, 0.2, 0.02 and 0.002. The results obtained for no perturbations show the shear layer growth purely due to viscous diffusion. It illustrates that without the low Mach correction growth of the layer is only marginally higher than with viscous diffusion alone at the lowest Mach number. Thus the dissipation in the Godunov method damps nearly all initial perturbations at low Mach numbers.

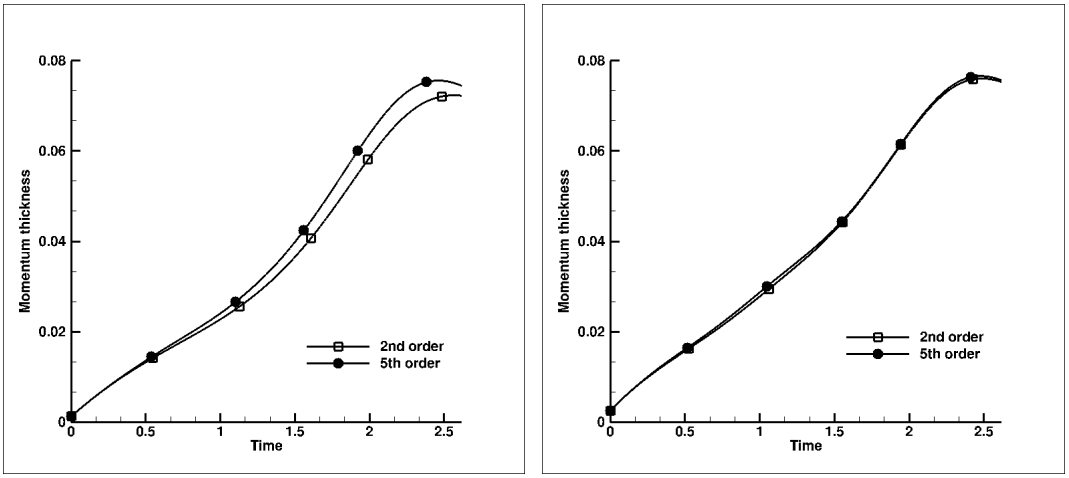

(a) 24×24 **(b)** 32×32

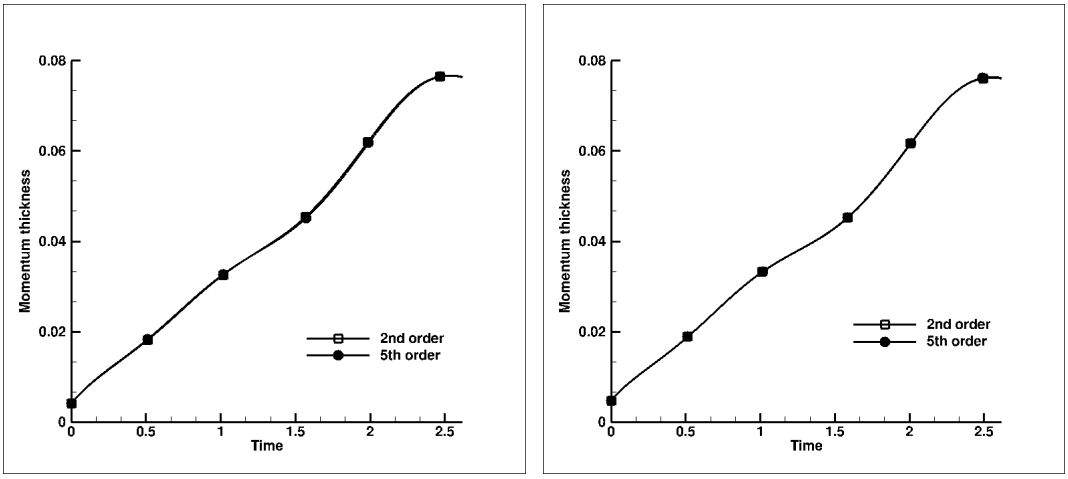

(c) 48×48 **(d)** 64×64

Figure 6.25: Momentum thickness against time (dimensionless) results obtained for 2^{nd} and 5^{th} order Godunov scheme with low Mach number correction feature on grid resolutions of 24×24, 32×32, 48×48 and 64×64 for the instability development of the two mode Kelvin–Helmholtz test case for Mach number at 0.02

A laminar case (i.e. without perturbations) is compared with the results obtained with the results where the perturbations are included. This result is shown in Figure 6.28 where the mixing layer thickness is obtained for all three different Mach numbers, 0.2, 0.02 and 0.002, on grid resolution of 64×64 using the 5^{th} order Godunov scheme with the low Mach number correction. The shear layer growth in the laminar case is purely due to viscous diffusion at all Mach numbers, which is clearly illustrated in the Figure 6.28. The growth of the mixing layer is enhanced by the introduction of the perturbations in the simulations regardless of the Mach number.

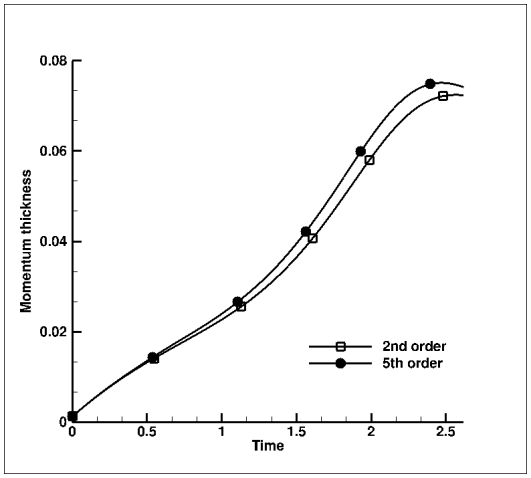

(a) 24×24

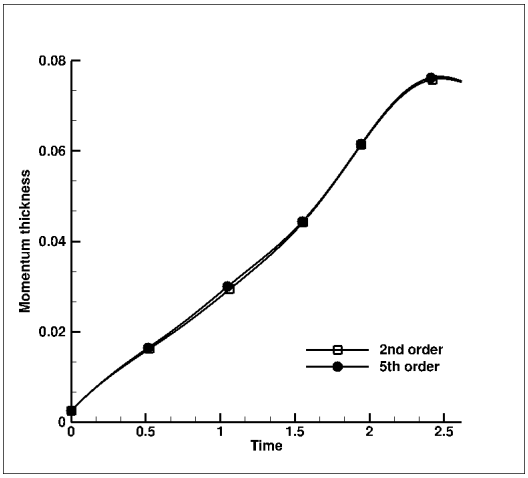

(b) 32×32

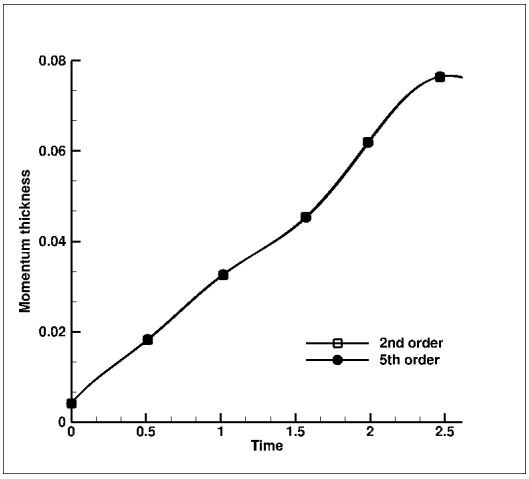

(c) 48×48

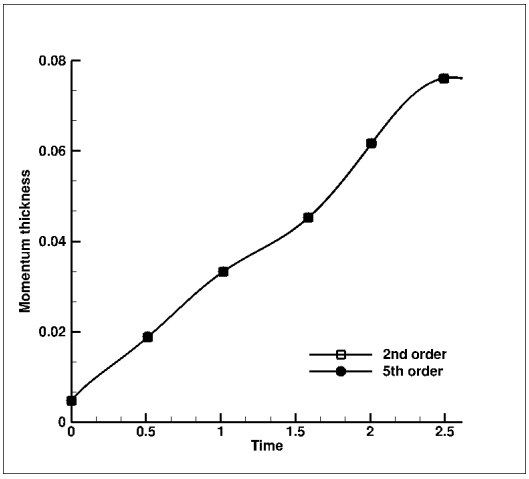

(d) 64×64

Figure 6.26: Momentum thickness against time (dimensionless) results obtained for 2^{nd} and 5^{th} order Godunov scheme with low Mach number correction feature on grid resolutions of 24×24, 32×32, 48×48 and 64×64 for the instability development of the two mode Kelvin–Helmholtz test case for Mach number at 0.002

6.6 Accessible Reference Results: ANSYS Fluent

The ability of the compressible flow solver of the commercial CFD software, ANSYS Fluent is also examined in capturing the development of the Kelvin–Helmholtz instability growth. Two different time stepping methods, implicit and explicit, implemented in the ANSYS Fluent is used in the compressible flow solver to capture the development of the Kelvin–Helmholtz instability growth. In both cases, implicit and explicit, a 2^{nd} order upwind scheme is used for spatial discretisation. The transient formulation is carried out by using both implicit and explicit time stepping methods. The time step size used during the simulation is $1 \times \exp^{-05}$ s.

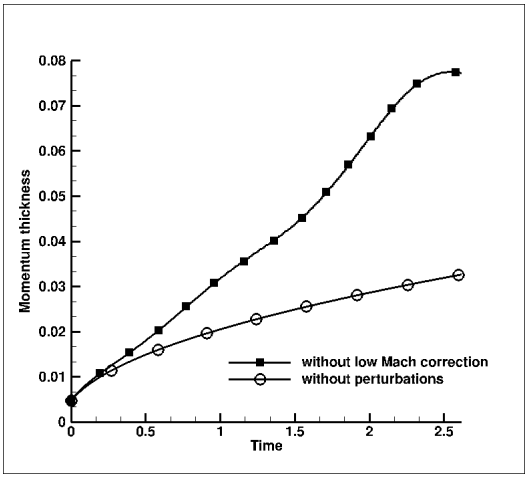

(a) Mach = 0.2

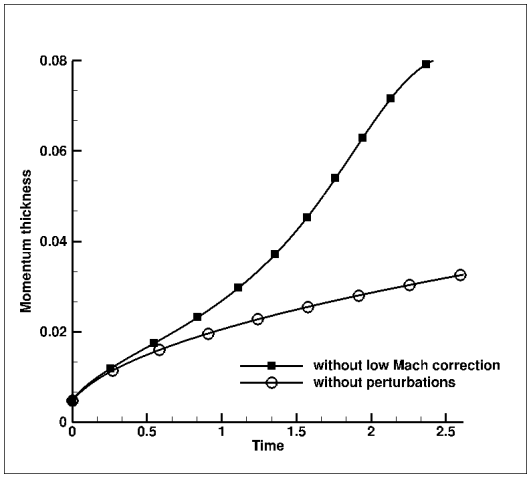

(b) Mach = 0.02

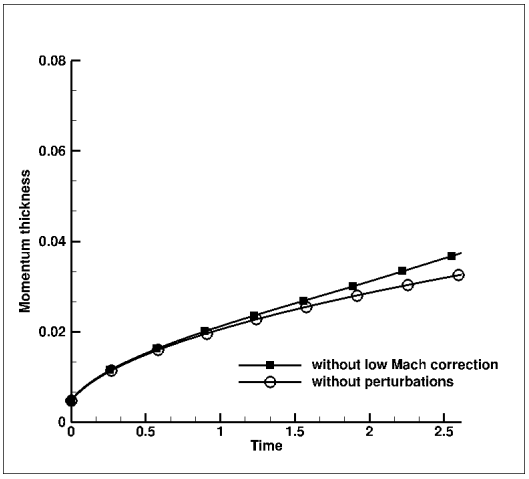

(c) Mach = 0.002

Figure 6.27: Momentum thickness against time (dimensionless) obtained from 5^{th} order Godunov scheme using both without the low Mach number correction and no perturbations with low Mach correction for Mach number of 0.2, 0.02 and 0.002 on grid resolution of 64×64

The development of the mixing layer is presented for all Mach numbers, 0.2, 0.02 and 0.002, on four different grid resolutions, 24×24, 32×32, 48×48 and 64×64 for both time stepping methods, implicit and explicit. Implicit and explicit results of the development of the mixing layer are compared against each other and the grid convergence of the implicit time stepping method is also highlighted.

6.6.1 Implicit Time Stepping Method

The observed vortex pairing process in Figure 6.29 illustrates the development of the Kelvin–Helmholtz instability captured by the implicit method of the compressible flow solver used in

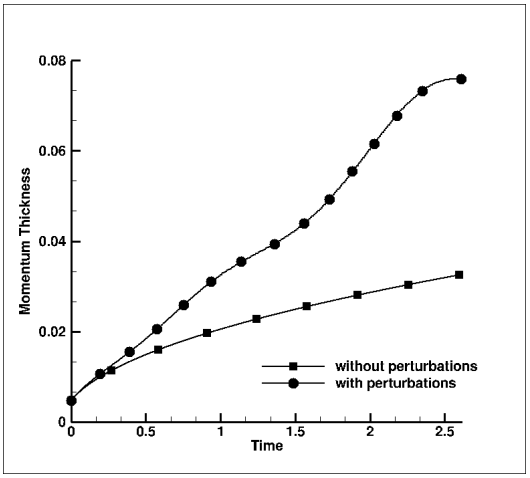

(a) Mach = 0.2

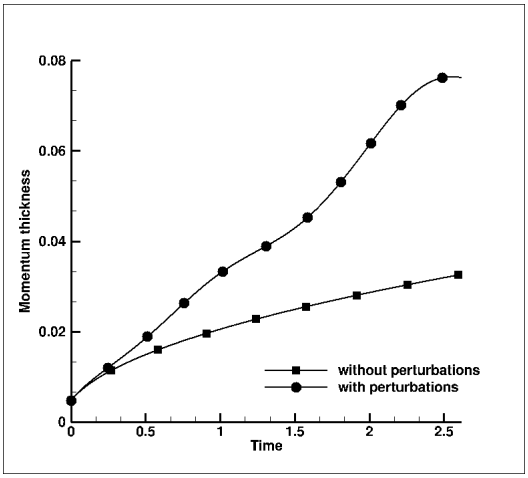

(b) Mach = 0.02

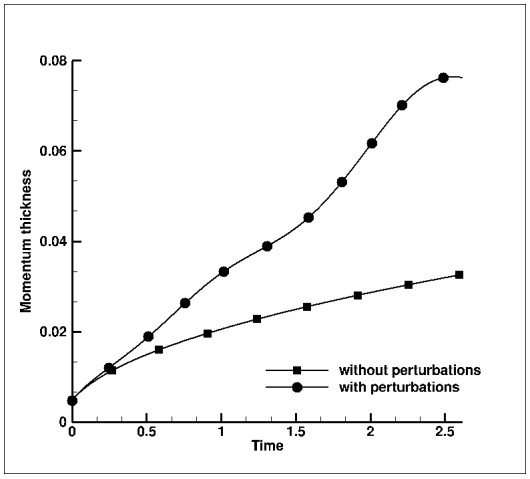

(c) Mach = 0.002

Figure 6.28: Momentum thickness against time (dimensionless) obtained from 5^{th} order Godunov scheme (`CHOC`) using the low Mach number correction with and without perturbations for Mach number of 0.2, 0.02 and 0.002 on grid resolution of 64×64

ANSYS Fluent on grid resolution of 64×64 for Mach number of 0.2.

The implicit time stepping method is consistent in capturing the development of the Kelvin–Helmholtz instability growth with the non-commercial codes, 5^{th} order Godunov approach with the low Mach correction, Lagrange-remap method, 5^{th} order wave propagation algorithm and 5^{th} order Godunov method with SLAU numerical flux, when the flow Mach number is 0.2.

6.6.2 Explicit Time Stepping Method

Figure 6.30 shows the results obtained for the compressible flow solver of the ANSYS Fluent where the transient formulation is carried out by using the explicit time stepping method. These

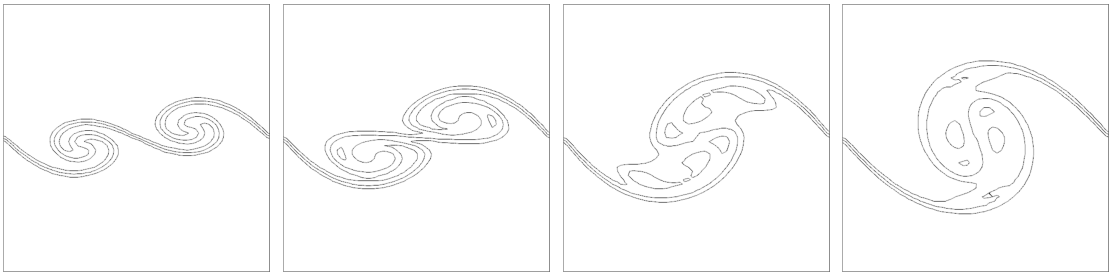

(a) t = 3s **(b)** t = 4s **(c)** t = 5s **(d)** t = 6s

Figure 6.29: Contour lines of volume fraction 0.25 to 0.75 for Mach number at 0.2 using ANSYS Fluent compressible solver with implicit time stepping method on grid resolution of 64×64

results are captured on grid resolution of 64×64 for Mach number of 0.2.

The development of the mixing layer at Mach number of 0.2 observed in Figure 6.30 concludes that the ANSYS Fluent implicit time stepping method results, shown in Figure 6.29, are different to explicit time stepping method on same grid resolution and same Mach number. ANSYS Fluent uses a low Mach number time-derivative preconditioner in the implicit time stepping method to provide accurate results but in the explicit time stepping approach the preconditioning is disabled. The results from both, implicit and explicit, time stepping approach clearly indicates that the implicit scheme is benefiting from the time-derivative preconditioner.

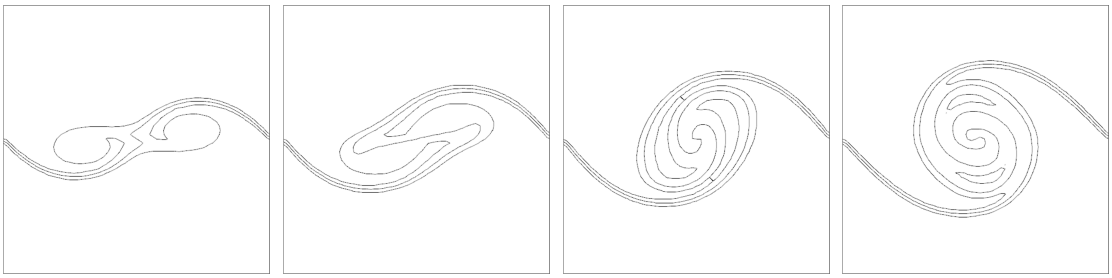

(a) t = 3s **(b)** t = 4s **(c)** t = 5s **(d)** t = 6s

Figure 6.30: Contour lines of volume fraction 0.25 to 0.75 for Mach number at 0.2 using ANSYS Fluent compressible solver with explicit time stepping method on grid resolution of 64×64

The development of the mixing layer at Mach number of 0.2 observed from Figures 6.29 and 6.30 shows that the ANSYS Fluent implicit time stepping method results are different to explicit time stepping method. Both time stepping methods, implicit and explicit, show the development of the mixing layer growth due to the initial instability but when comparing these two Figures the two different time stepping methods are not producing the identical results. The results from implicit time stepping method shows more detailed flow structure, at $t = 3s$ the two vortices are clearly visible and separate from each other whereas in the explicit time stepping method the vortices are closer to each other and less well resolved. In both cases the vortex structures are completely different, however the implicit time stepping approach is more comparable to the results of the non-commercial codes.

6.6.3 Implicit versus Explicit

The momentum thickness of the mixing layer for implicit and explicit time stepping methods are shown in Figure 6.31 for Mach numbers 0.2 and 0.02 on same grid resolution of 64×64. These Figures correspond to the observed vortex pairing process shown in Figures 6.29 and 6.30 for Mach number of 0.2 and Figures 6.32 and 6.34 for Mach number of 0.02. The explicit method has a marginally slower growth of the second mode compared to the implicit method. Excess dissipation in the explicit time stepping method reduces the instability development as the Mach number is reduced to 0.02. The explicit method was not run at a lower Mach number or grid resolution as all results were essentially null, i.e. numerical dissipation completely prevents any instability growth. Comparing this to the second order accurate results shown in Figures 6.24, 6.25 and 6.26 again reinforces the need for a low Mach correction.

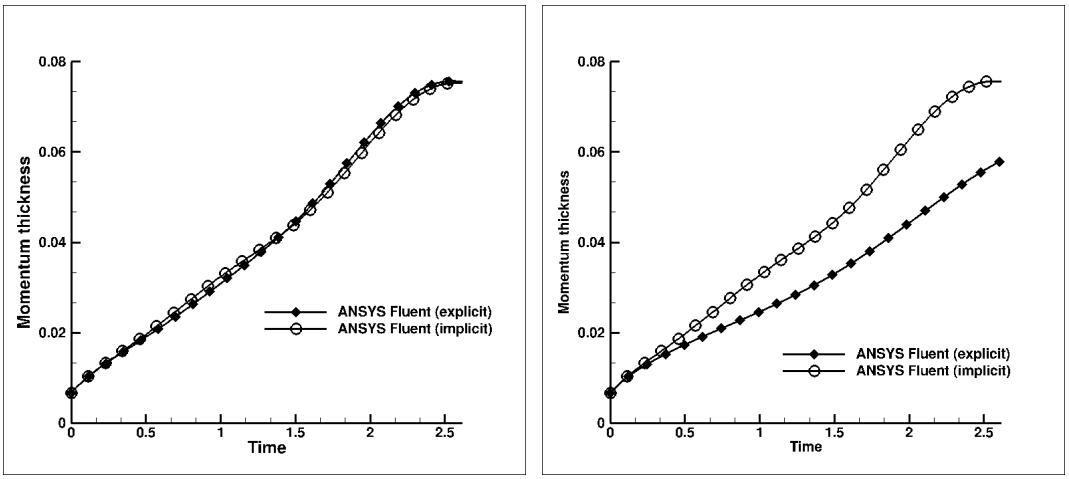

(a) Mach = 0.2 **(b)** Mach = 0.02

Figure 6.31: Momentum thickness against time (dimensionless) obtained from the compressible solver of ANSYS Fluent for explicit and implicit time stepping methods on grid resolution of 64×64 for Mach number of 0.2 and 0.02

6.6.4 Mach Number Effects

The behaviour of the two different time stepping methods in low Mach number region are compared by using the results of the instability development in the low Mach region of 0.02 and 0.002.

Figures 6.32 and 6.33 show the ability of the compressible flow solver of ANSYS Fluent with implicit time stepping method in capturing the vortices at low Mach numbers, 0.02 and 0.002. The development of the initial instability is captured on 64×64 grid resolution. The two vortices combine together to form a single larger vortex as observed with the 5^{th} order Godunov approach with the low Mach correction and 5^{th} order Godunov method with SLAU numerical flux. This highlights the observation that the dissipative properties of the numerical scheme cannot be predicted by separate consideration of temporal and spatial discretisation, clearly the dissipation of kinetic energy occurs via a different mechanism in the implicit formulation. Here the implicit scheme is benefiting from the time derivative preconditioner, however this would not be accurate

in the presence of shock waves.

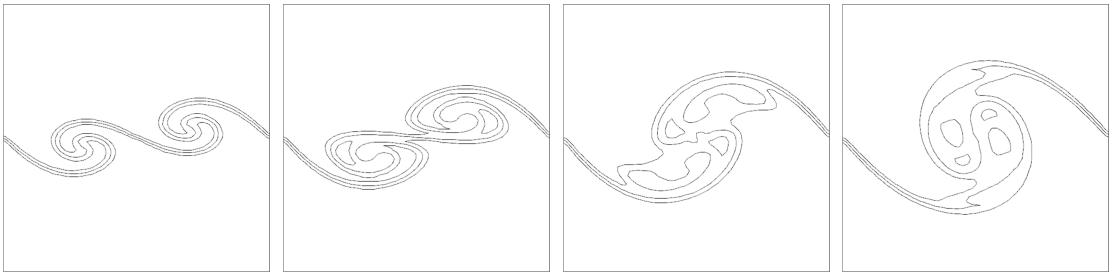

(a) t = 3s **(b)** t = 4s **(c)** t = 5s **(d)** t = 6s

Figure 6.32: Contour lines of volume fraction 0.25 to 0.75 for Mach number at 0.02 using ANSYS Fluent compressible solver with implicit time stepping method on grid resolution of 64×64

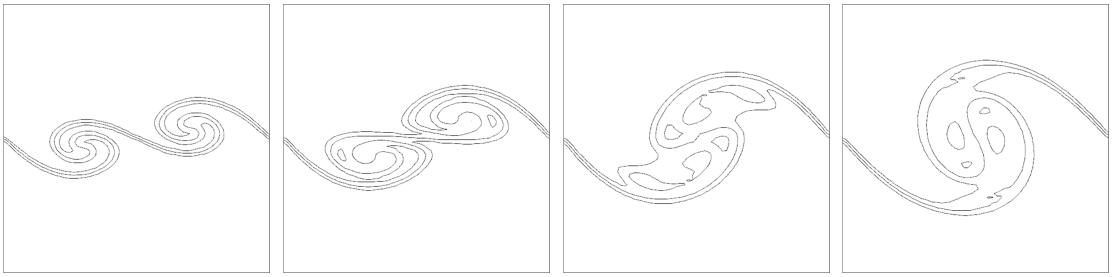

(a) t = 3s **(b)** t = 4s **(c)** t = 5s **(d)** t = 6s

Figure 6.33: Contour lines of volume fraction 0.25 to 0.75 for Mach number at 0.002 using ANSYS Fluent compressible solver with implicit time stepping method on grid resolution of 64×64

The inability of the compressible solver of ANSYS Fluent with explicit time stepping method in capturing the instability growth at Mach number of 0.02 is shown in Figure 6.34. The excessive dissipation in the explicit time stepping method of the compressible flow solver of ANSYS Fluent prevents the growth of the two modes and the instability growth even at this moderate Mach number and high grid resolution.

6.6.5 Grid Convergence

Figure 6.35 shows the results of grid convergence test on all grid resolutions obtained by the compressible flow solver of ANSYS Fluent with the implicit time stepping method for all Mach numbers, 0.2, 0.02 and 0.002. The mixing layer thickness developed by the Kelvin–Helmholtz instability growth shows that for all Mach numbers the solution converges from grid resolution of 48×48 and comparable to the results of the non-commercial codes, 5^{th} order Godunov approach with the low Mach correction and 5^{th} order Godunov method with SLAU numerical flux, in Figures 6.6 and 6.9.

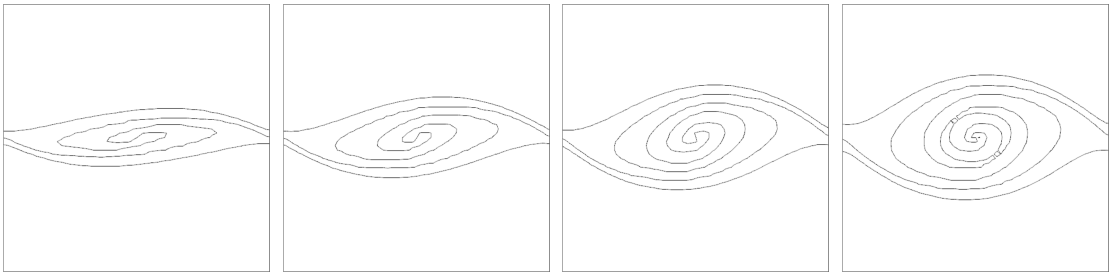

(a) t = 3s **(b)** t = 4s **(c)** t = 5s **(d)** t = 6s

Figure 6.34: Contour lines of volume fraction 0.25 to 0.75 for Mach number at 0.2 using ANSYS Fluent compressible solver with explicit time stepping method on grid resolution of 64×64

6.7 Comparison of Grid Converged Solutions

The performance of the numerical schemes in the low Mach region are compared in this section. The numerical schemes included in this comparison are 5^{th} order Godunov scheme with low Mach number correction, Lagrange-remap method and 5^{th} order Godunov method with SLAU numerical flux. The results obtained by the explicit time stepping method in ANSYS Fluent has not been included as this is significantly over-dissipative and the results of 5^{th} order wave propagation algorithm is also excluded in this section due to the poor performance in low Mach regions as shown earlier.

The grid converged solutions (64×64 grid resolution) are compared for all Mach numbers, 0.2, 0.02 and 0.002, and the performance of Lagrange-remap method is compared against other numerical methods only at Mach number of 0.2 as this numerical scheme is independent of Mach number.

Figure 6.36 shows the converged solutions obtained from the 5^{th} order Godunov scheme with low Mach number correction, Lagrange-remap method and 5^{th} order Godunov method with SLAU numerical flux. For all Mach numbers, 0.2, 0.02 and 0.002, with the implicit time stepping method the mixing layer growth of the 1^{st} mode and 2^{nd} mode are marginally higher than the non-commercial codes compared against. However the growth of the 2^{nd} mode by the implicit time stepping method still merges with the growth of the 2^{nd} mode captured by non-commercial codes at a dimensionless time of 1.

The non-commercial code, Lagrange-remap method, predicts the mixing layer growth similar to the other non-commercial codes, 5^{th} order Godunov scheme with low Mach number correction and 5^{th} order Godunov method with SLAU numerical flux, but has a marginally lower growth for the 2^{nd} mode at a dimensionless time of 1 for Mach number of 0.2. this is clearly visible from the momentum thickness against time (dimensionless) results shown in Figure 6.36(a).

5^{th} order Godunov scheme with low Mach number correction and 5^{th} order Godunov method with SLAU numerical flux captures the development of the Kelvin–Helmholtz instability growth identically. The low Mach correction feature and the SLAU numerical flux used in the Godunov approach perform well in the low Mach region by capturing the vortex pairing process accurately and identically for all Mach numbers on same grid resolution.

Figure 6.37 shows the comparison of the momentum thickness against time for 64×64 grid resolution and Mach number examined for 5^{th} order Godunov scheme with low Mach number correction, 5^{th} order Godunov method with SLAU numerical flux and ANSYS Fluent implicit time scheme. The results indicate that the numerical schemes are predicting a Mach independent

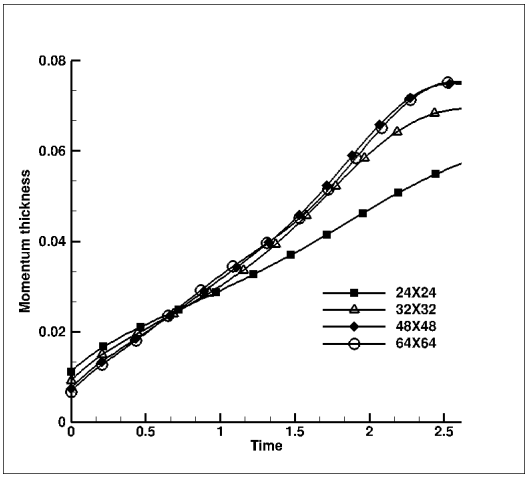

(a) Mach = 0.2

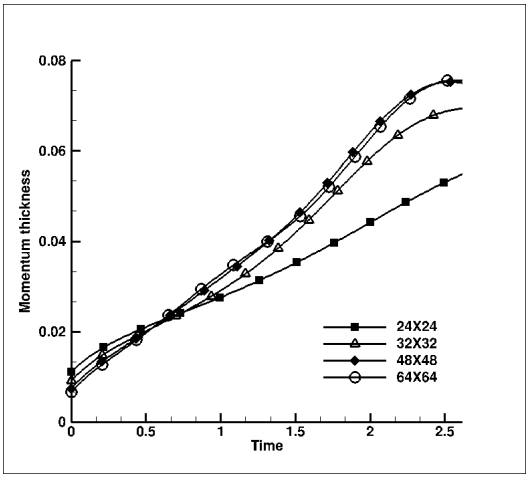

(b) Mach = 0.02

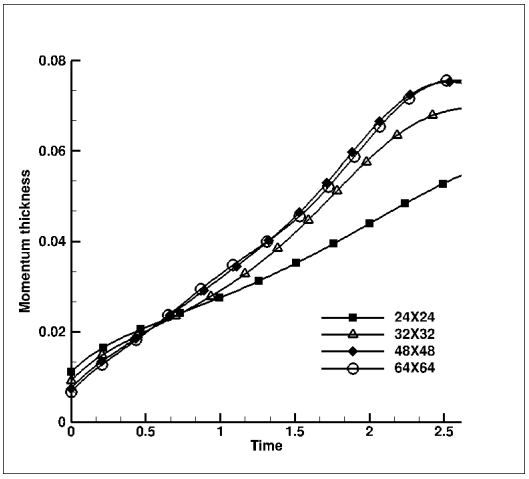

(c) Mach = 0.002

Figure 6.35: Momentum thickness against time (dimensionless) obtained from the compressible solver of ANSYS Fluent with implicit time stepping method on grid resolutions of 24×24, 32×32, 48×48 and 64×64 for Mach numbers of 0.2, 0.02 and 0.002

structure as the Mach number decreases, as the physics of the governing equations predict.

6.8 Computational Time Requirements

Table 6.2 shows the time requirement of 2^{nd} and 5^{th} order Godunov method with low Mach correction and implicit and explicit time stepping methods of ANSYS Fluent for the test case on grid resolution of 64×64 for Mach numbers, 0.2, 0.02 and 0.002. The time taken to achieve the converged results are a lot less using the compressible flow solver of the commercial software, ANSYS Fluent than the non-commercial code, Godunov method with low Mach correction. The

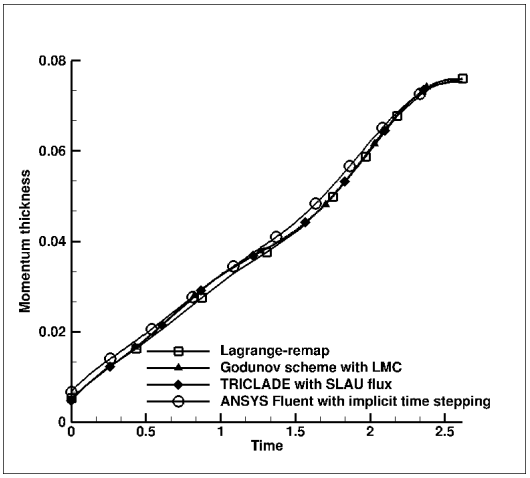

(a) Mach = 0.2

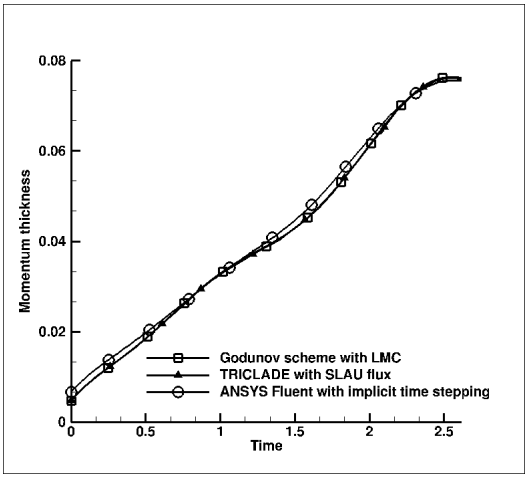

(b) Mach = 0.02

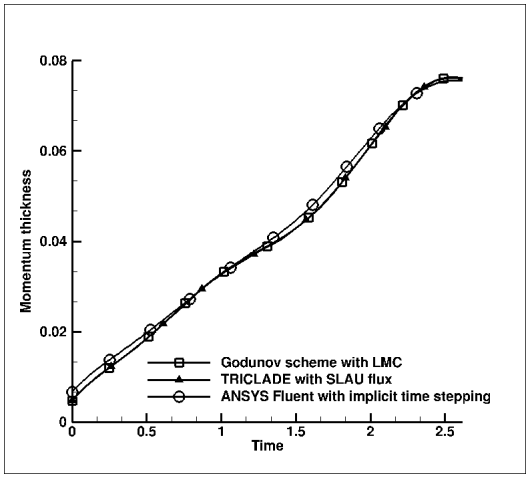

(c) Mach = 0.002

Figure 6.36: Comparison of scheme performance using the results obtained for momentum thickness against time (dimensionless) using 5^{th} order Godunov scheme with low Mach number correction (LMC), Godunov method with SLAU numerical flux (5^{th} order space accuracy, 3^{rd} order time accuracy, and MP limitation), Lagrange-remap method and the compressible solver of ANSYS Fluent with implicit time stepping method on grid resolution of 64×64 for Mach numbers of 0.2, 0.02 and 0.002

difference in time taken for simulations of the 2^{nd} and 5^{th} order Godunov method with low Mach correction are very small. The 5^{th} order Godunov method with low Mach correction has taken longer when compared to the 2^{nd} order method. The vortex pairing prediction by the commercial software, ANSYS Fluent on grid resolution of 64×64 indicates that the implicit time stepping method takes a lot less time to provide accurate results for all Mach numbers, 0.2, 0.02 and 0.002, when compared to the non-commercial code, Godunov method with low Mach correction. Another conclusion from the results shown in Table 6.2 indicates that the time required by the

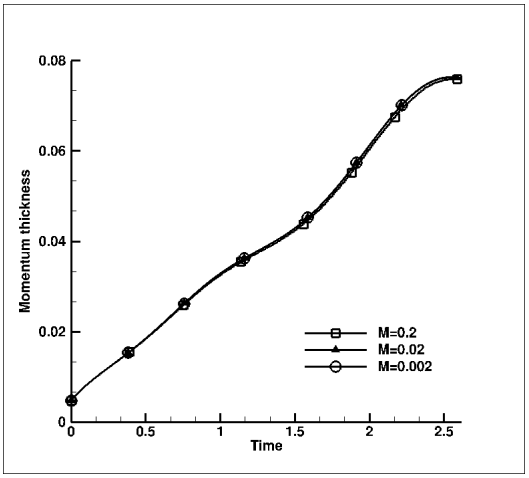

(a) 5^{th} order Godunov approach with the low Mach correction

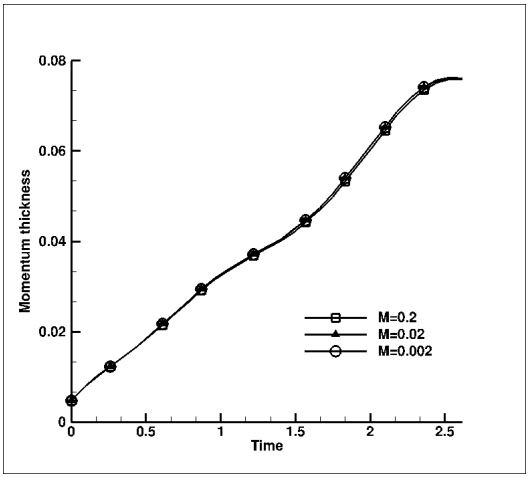

(b) 5^{th} order Godunov method with SLAU numerical flux

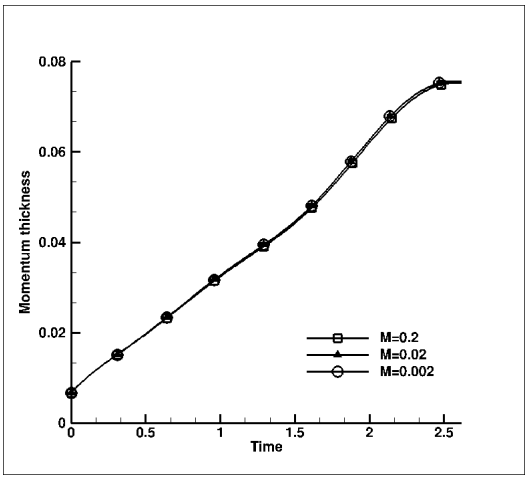

(c) ANSYS Fluent implicit time scheme

Figure 6.37: Momentum thickness against time (dimensionless) for grid converged (64×64) solutions of 5^{th} order Godunov scheme with low Mach number correction, 5^{th} order Godunov method with SLAU numerical flux and ANSYS Fluent implicit time scheme for Mach numbers at 0.2, 0.02 and 0.002

commercial software, ANSYS Fluent is identical in all three different Mach numbers, predicting a Mach independent computational cost in the case of implicit time approach. Comparison between implicit and explicit time approach shows that the explicit time stepping method takes a less time but the excessive dissipation in the explicit time stepping method of the compressible flow solver of ANSYS Fluent prevents the growth of the two modes and the instability growth even at this moderate Mach number and high grid resolution. The time required by the explicit time stepping method for Mach number 0.002 is not shown in Table 6.2 as the explicit method was not run at a lower Mach number or grid resolution as all results were essentially null, i.e.

numerical dissipation completely prevents any instability growth.

Table 6.2: The time required for the simulation of the vortex pairing process using 2^{nd} and 5^{th} order Godunov scheme with low Mach number correction feature and implicit and explicit time approach in ANSYS Fluent on grid resolution of 64×64 for all Mach numbers, 0.2, 0.02 and 0.002

Mach number	*Grid resolution*	*Time Required* (s)			
		Godunov scheme		*ANSYS Fluent*	
		5^{th} *order*	2^{nd} *order*	*Implicit*	*Explicit*
0.2	64×64	10021.02	9838.50	610	180
0.02	64×64	16033.08	15741.06	610	540
0.002	64×64	71688.04	70977.84	610	-

Chapter 7

Conclusions

For Mach number 0.2, the grid converged results obtained for vortex pairing are identical with the Lagrange-remap method, Godunov approach with and without low-Mach number correction, Godunov method with SLAU numerical flux which includes the low Mach capture property and wave propagation algorithm. As the Mach number is reduced, without the low Mach number correction, results become very dissipative for all schemes excepting the Lagrange-remap method and ANSYS Fluent with implicit time stepping. With the low Mach number correction, results are insensitive to the Mach number and accurate results are obtained with only 48×48 grid resolution. The need to use specifically designed low Mach corrections or fluxes in Godunov-based techniques during low Mach number simulations is clearly demonstrated. The momentum thickness against time shows that Godunov scheme with the low Mach number correction and SLAU numerical flux captures the 2^{nd} mode more accurately when compared with the other algorithms used in this test case. Results from the compressible flow solver of ANSYS Fluent show for simulations below Mach number of 0.2 implicit time stepping method provides accurate results, but the explicit scheme performs very poorly. Furthermore the utility of this well posed test case to highlight scheme performance for vortical flows has been established.

Bibliography

[1] Admin. March 2012. URL: http://askphysics.com/relation_between_velocity_and_and_pressure_for_fluids/.

[2] Y. Nakayama and R. F. Boucher. *Introduction to Fluid Mechanics*. Arnold, 1999.

[3] A. Bhatia. March 2012. URL: http://www.empiricalzeal.com/wp-content/uploads/2011/07/reynolds-flow.png.

[4] C. D. Winant and F. K. Browand. Vortex pairing: the mechanism of turbulent mixing-layer growth at moderate Reynolds number. *Journal of Fluid Mechanics*, 63:237–255, 1974.

[5] P. K. Kundu and I. M. Cohen. *Fluid Mechanics*. Elsevier Academic Press, 2004.

[6] G. L. Brown and A. Roshko. On density effects and large structure in turbulent mixing layers. *Journal of Fluid Mechanics*, 64:775–816, 1974.

[7] F. K. Browand and P. D. Weidman. Large scales in the developing mixing layer. *Journal of Fluid Mechanics*, 76:127–144, 1976.

[8] P. E. Dimotakis and A. G. Brown. The mixing layer at high Reynolds number: large-structure dynamics and entrainment. *Journal of Fluid Mechanics*, 78:535–560, 1976.

[9] F. K. Browand and T. R. Troutt. A note on spanwise structure in the two-dimensional mixing layer. *Journal of Fluid Mechanics*, 97:771–781, 1980.

[10] H. Aref and E. Siggia. Vortex dynamics of the two-dimensional turbulent shear layer. *Journal of Fluid Mechanics*, 100:705–737, 1980.

[11] L. P. Bernal and A. Roshko. Streamwise Vortex Structure in Plane Mixing Layers. *Journal of Fluid Mechanics*, 170:499–525, 1986.

[12] J. Fontane and L. Joly. The stability of the variabledensity KelvinHelmholtz billow. *Journal of Fluid Mechanics*, 612:237–260, 2008.

[13] J. Griffond. Private communication. 2012.

[14] D. L. Youngs. Private communication. 2011.

[15] H. K. Versteeg and W. Malalasekera. *An Introduction to Computational Fluid Dynamics, the Finite Volume Method*. Pearson Prentice Hall, 2007.

[16] A. H. Shapiro. *Shape and Flow*. Heinemann, 1960.

[17] Webmaster. March 2012. URL: http://www.cfd-online.com/Wiki/Large_eddy_simulation_%28LES%29.

[18] S. B. Pope. *Turbulent Flows*. Cambridge university press, 2006.

[19] B. Thornber. *Introduction to turbulent flows and turbulent flow modelling.* Cranfield University Lecture Notes, 2012.

[20] G. Allaire, S. Clerc, and S. Kokh. A five-equation model for the simulation of interfaces between compressible fluids. *Journal of Computational Physics*, 181:577–616, 2002.

[21] R. J. Leveque. *Finite Volume Methods for Hyperbolic Problems.* Cambridge University Press, 2005.

[22] E. Toro. *Riemann Solvers and Numerical Methods for Fluid Dynamics.* Springer-Verlag, Cambridge, 1997.

[23] ANSYS Fluent. November 2012. URL: `http://www.ansys.com/Products/Simulation+Technology/Fluid+Dynamics/ANSYS+Fluent`.

[24] B. Thornber, A. Mosedale, D. Drikakis, D. L. Youngs, and R. J. R. Williams. An improved reconstruction method for compressible flows with low Mach number features. *Journal of Computational Physics*, 227:4873–4894, 2008.

[25] Bilger R. W. Masri A. R. Thornber, B. and E. R. Hawkes. An algorithm for LES of premixed compressible flows using the Conditional Moment Closure model. *Journal of Computational Physics*, 230:7687–7705, 2011.

[26] R.J. Spiteri and S.J. Ruuth. A class of optimal high-order strong-stability preserving time discretization methods. *SIAM Journal of Numerical Analysis*, 40:469–491, 2002.

[27] D. L. Youngs. Time-dependent multi-material flow with large fluid distortion. *In Numerical Methods for Fluid Dynamics, Morton KW, Baines MJ (eds). Academic Press: New York*, 13:273–285, 1982.

[28] D. L. Youngs. Numerical simulation of mixing by Rayleigh-Taylor and Richtmyer-Meshkov instabilities. *Laser and particle beams*, 12:725–750, 1994.

[29] R. Debar. A method in 2-d Eulerian hydrodynamics. Technical report, UCID-196831, Lawrence Livermore National Laboratory, 1974.

[30] J. Griffond. Linear interaction analysis applied to a mixture of two perfect gases. *Physics of Fluids*, 17:086101, 2005.

[31] Griffond J. Soulard, O. and D. Souffland. Pseudocompressible approximation and statistical turbulence modeling: Application to shock tube flows. *Physical Review E*, 85:026307, 2012.

[32] R. J. LeVeque. Finite Volume Methods for Hyperbolic Problems. 2002.

[33] V. Daru and C. Tenaud. High order one-step monotonicity-preserving schemes for unsteady compressible flow calculations. *Journal of Computational Physics*, 193:563–594, 2004.

[34] A. Suresh and H. T. Huynh. Accurate monotonicity preserving schemes with Runge-Kutta time stepping. *Journal of Computational Physics*, 136:83–99, 1997.

[35] S. Dellacherie. Analysis of Godunov type schemes applied to the compressible Euler system at low Mach number. *Journal of Computational Physics*, 229:978–1016, 2010.

[36] X. S. Li and C. W. Gu. An All-Speed Roe-type scheme and its Asymptotic Analysis of Low Mach Number Behaviour. *Journal of Computational Physics*, 227:5144–5159, 2008.

[37] E. Shima and K. Kitamura. Parameter-free simple low-dissipation AUSM-family scheme for all speeds. *AIAA Journal*, 2011.

[38] A. Dowling. *Introduction to Fluid Mechanics*. Cambridge University Lecture Notes, 2005.

[39] F. K. Browand and B. O. Latigo. Growth of the twodimensional mixing layer from a turbulent and nonturbulent boundary layer. *Physics of Fluids*, 22:1011–1019, 1979.

[40] B. Gustafsson and H. Stoor. Navier–Stokes equations for almost incompressible flow. *SIAM Journal of Numerical Analysis*, 28:1523–1547, 1991.

[41] S. Klainerman and A. Majda. Compressible and incompressible fluids. *Communications on Pure and Applied Mathematics*, 35:629–651, 1982.

[42] H.O. Kreiss, J. Lorenz, and M. Naughton. Convergence of the solutions of the compressible to the solutions of the incompressible Navier–Stokes equations. *Advances in Applied Mathematics*, 12:187–214, 1991.

[43] E. Turkel, A. Fiterman, and B. van Leer. Preconditioning and the limit to the incompressible flow equations. NASA Contractor Report 191500 93–42, National Aeronautics and Space Administration, Langley research centre, Hampton, Virginia 23681–0001, July 1993.

[44] E. Turkel. Preconditioned methods for solving the incompressible and low speed compressible equations. *Journal of Computational Physics*, 72:277–298, 1987.

[45] J. Jorn Sesterhenn, B. Muller, and H. Thomann. On the cancellation problem in calculating compressible low Mach number flows. *Journal of Computational Physics*, 151:597–615, 1999.

[46] G. Volpe. Performance of compressible flow codes at low Mach number. *AIAA J.*, 31:49–56, 1993.

[47] W. Noh. Errors for calculations of strong shocks using and artificial viscosity and an artificial heat flux. *Journal of Computational Physics*, 72:78–120, 1987.

[48] J. von Neumann and R. D. Richtmyer. *Journal of Applied Physics*, 21:232, 1950.

[49] H. Guillard and C. Viozat. On the behaviour of upwind schemes in the low Mach number limit. *Computational Fluids*, 28:63–86, 1999.

[50] H. Guillard and A. Murrone. On the behaviour of upwind schemes in the low Mach number limit: Ii. Godunov type schemes. *Computational Fluids*, 33:655–675, 2004.

[51] B. Thornber, A. Mosedale, D. Drikakis, D. L. Youngs, and R. J. R. Williams. On entropy generation and dissipation of kinetic energy in high-resolution shock-capturing schemes. *Journal of Computational Physics*, 227:4853–4872, 2008.

[52] F. Rieper. A low-Mach number fix for Roes approximate Riemann solver. *Journal of Computational Physics*, 230:5263–5287, 2011.

[53] B. Einfeldt. Ein schneller algorithmus zur lsung des Riemann-problems (an efficient algorithm for the solution to the Riemann problem). *Computing*, 39:77–86, 1987.

[54] P. G. Drazin and W. H. Reid. *Hydrodynamic Stability*. Cambridge University Press, 2004.

Appendix A

Vortex pairing - 5^{th} order Godunov method

A.1 5^{th} order Godunov method with low Mach correction

The development of the Kelvin–Helmholtz instability captured on all grid resolutions, 24×24, 32×32, 48×48 and 64×64, for all Mach numbers, 0.2, 0.02 and 0.002, by 5^{th} order Godunov method with low Mach correction are included in this section.

A.1.1 Mach number at 0.2

A.1.1.1 Grid resolution 24×24

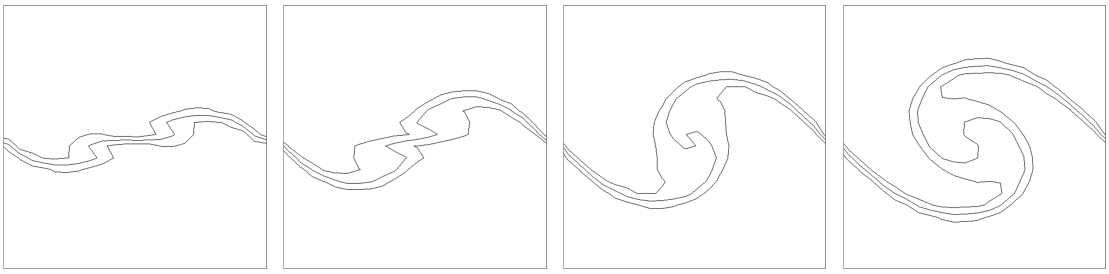

(a) t = 3s **(b)** t = 4s **(c)** t = 5s **(d)** t = 6s

Figure A.1: Contour lines of volume fraction 0.25 to 0.75 for the instability development of the two mode Kelvin–Helmholtz test case captured by 5^{th} order Godunov method with low Mach correction for Mach number at 0.2 on grid resolution of 24×24

A.1.1.2 Grid resolution 32×32

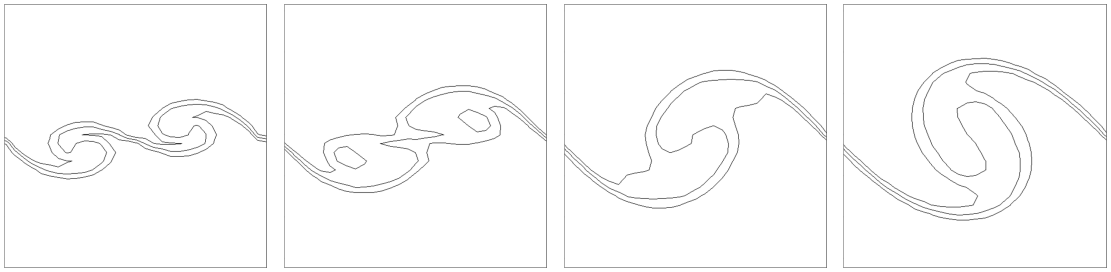

(a) t = 3s **(b)** t = 4s **(c)** t = 5s **(d)** t = 6s

Figure A.2: Contour lines of volume fraction 0.25 to 0.75 for the instability development of the two mode Kelvin–Helmholtz test case captured by 5^{th} order Godunov method with low Mach correction for Mach number at 0.2 on grid resolution of 32×32

A.1.1.3 Grid resolution 48×48

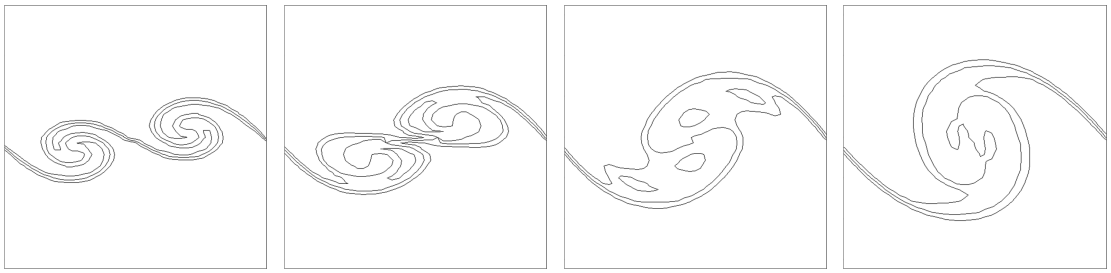

(a) t = 3s **(b)** t = 4s **(c)** t = 5s **(d)** t = 6s

Figure A.3: Contour lines of volume fraction 0.25 to 0.75 for the instability development of the two mode Kelvin–Helmholtz test case captured by 5^{th} order Godunov method with low Mach correction for Mach number at 0.2 on grid resolution of 48×48

A.1.1.4 Grid resolution 64×64

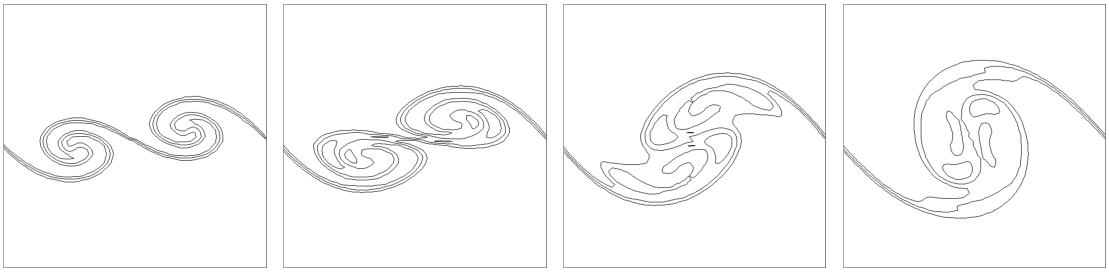

(a) t = 3s **(b)** t = 4s **(c)** t = 5s **(d)** t = 6s

Figure A.4: Contour lines of volume fraction 0.25 to 0.75 for the instability development of the two mode Kelvin–Helmholtz test case captured by 5^{th} order Godunov method with low Mach correction for Mach number at 0.2 on grid resolution of 64×64

A.1.1.5 Grid resolution 128×128

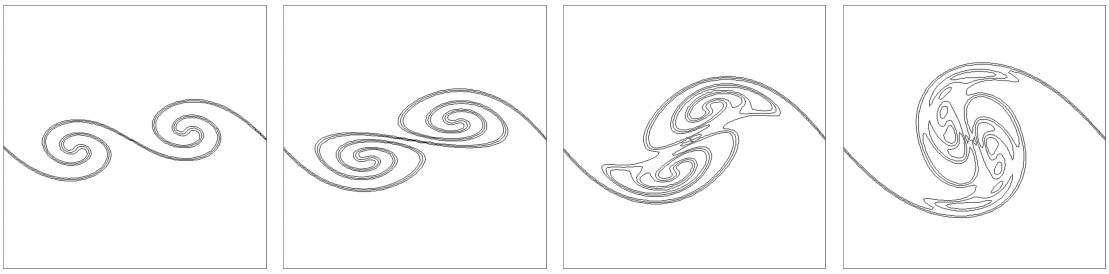

(a) t = 3s **(b)** t = 4s **(c)** t = 5s **(d)** t = 6s

Figure A.5: Contour lines of volume fraction 0.25 to 0.75 for the instability development of the two mode Kelvin–Helmholtz test case captured by 5^{th} order Godunov method with low Mach correction for Mach number at 0.2 on grid resolution of 128×128

A.1.2 Mach number at 0.02

A.1.2.1 Grid resolution 24×24

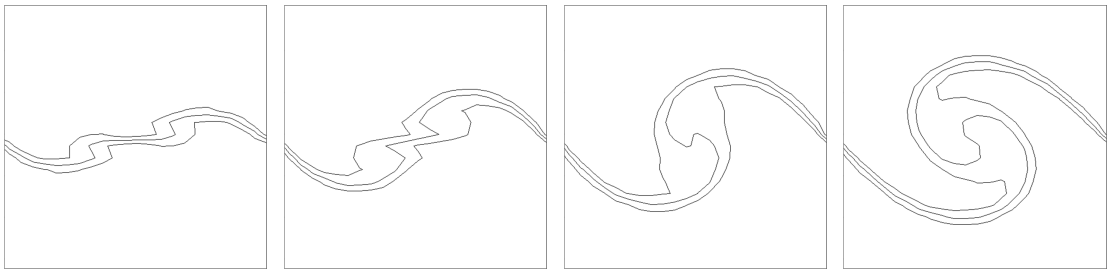

(a) t = 3s **(b)** t = 4s **(c)** t = 5s **(d)** t = 6s

Figure A.6: Contour lines of volume fraction 0.25 to 0.75 for the instability development of the two mode Kelvin–Helmholtz test case captured by 5^{th} order Godunov method with low Mach correction for Mach number at 0.02 on grid resolution of 24×24

A.1.2.2 Grid resolution 32×32

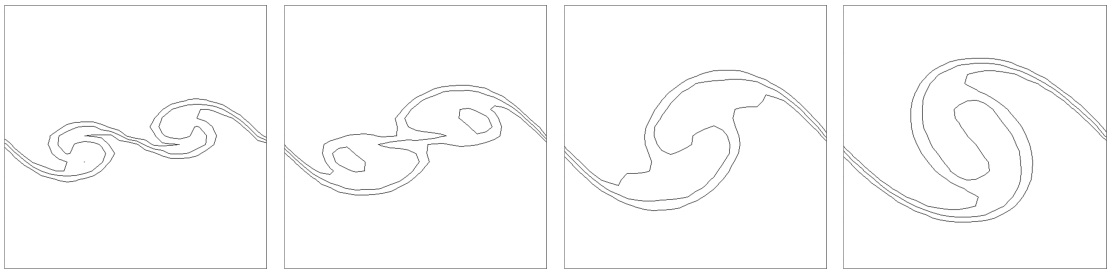

(a) t = 3s **(b)** t = 4s **(c)** t = 5s **(d)** t = 6s

Figure A.7: Contour lines of volume fraction 0.25 to 0.75 for the instability development of the two mode Kelvin–Helmholtz test case captured by 5^{th} order Godunov method with low Mach correction for Mach number at 0.02 on grid resolution of 32×32

A.1.2.3 Grid resolution 48×48

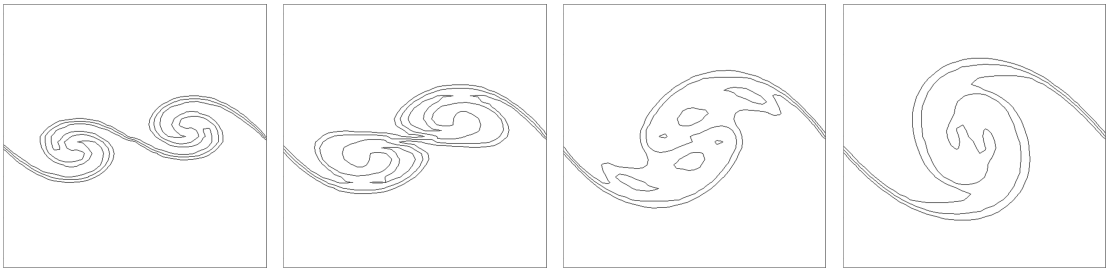

(a) t = 3s **(b)** t = 4s **(c)** t = 5s **(d)** t = 6s

Figure A.8: Contour lines of volume fraction 0.25 to 0.75 for the instability development of the two mode Kelvin–Helmholtz test case captured by 5^{th} order Godunov method with low Mach correction for Mach number at 0.02 on grid resolution of 48×48

A.1.2.4 Grid resolution 64×64

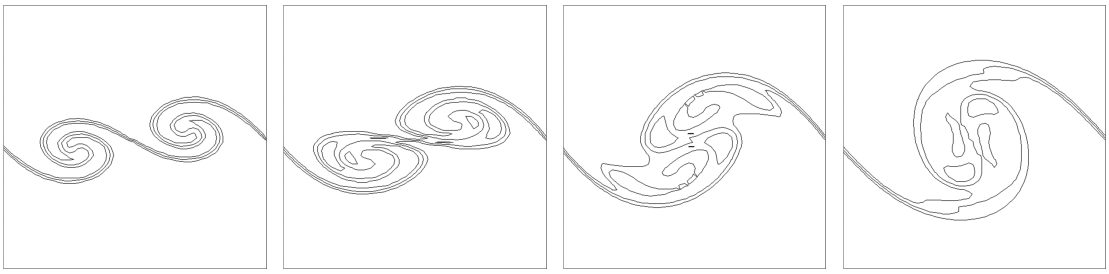

(a) t = 3s **(b)** t = 4s **(c)** t = 5s **(d)** t = 6s

Figure A.9: Contour lines of volume fraction 0.25 to 0.75 for the instability development of the two mode Kelvin–Helmholtz test case captured by 5^{th} order Godunov method with low Mach correction for Mach number at 0.02 on grid resolution of 64×64

A.1.3 Mach number at 0.002

A.1.3.1 Grid resolution 24×24

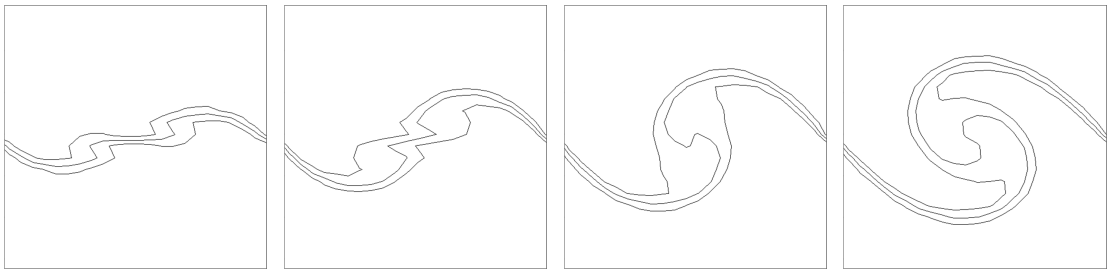

(a) t = 3s **(b)** t = 4s **(c)** t = 5s **(d)** t = 6s

Figure A.10: Contour lines of volume fraction 0.25 to 0.75 for the instability development of the two mode Kelvin–Helmholtz test case captured by 5^{th} order Godunov method with low Mach correction for Mach number at 0.002 on grid resolution of 24×24

A.1.3.2 Grid resolution 32×32

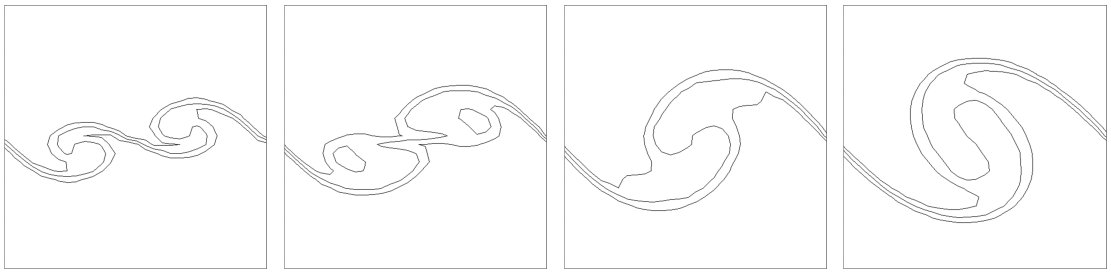

(a) t = 3s **(b)** t = 4s **(c)** t = 5s **(d)** t = 6s

Figure A.11: Contour lines of volume fraction 0.25 to 0.75 for the instability development of the two mode Kelvin–Helmholtz test case captured by 5^{th} order Godunov method with low Mach correction for Mach number at 0.002 on grid resolution of 32×32

A.1.3.3 Grid resolution 48×48

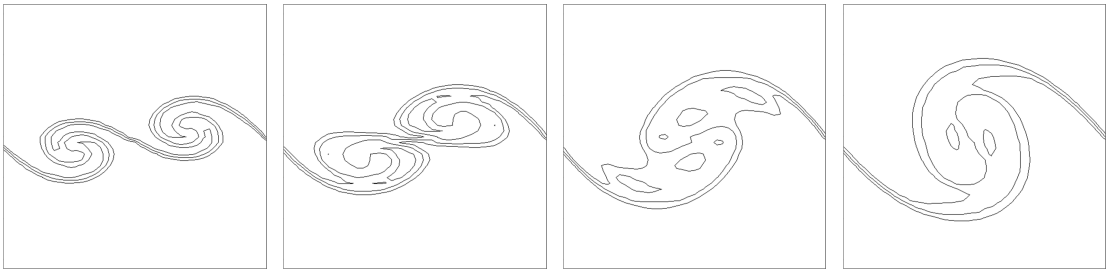

(a) t = 3s **(b)** t = 4s **(c)** t = 5s **(d)** t = 6s

Figure A.12: Contour lines of volume fraction 0.25 to 0.75 for the instability development of the two mode Kelvin–Helmholtz test case captured by 5^{th} order Godunov method with low Mach correction for Mach number at 0.002 on grid resolution of 48×48

A.1.3.4 Grid resolution 64×64

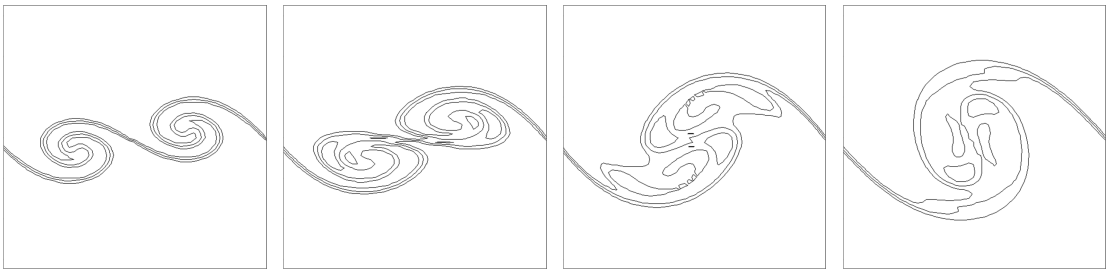

(a) t = 3s **(b)** t = 4s **(c)** t = 5s **(d)** t = 6s

Figure A.13: Contour lines of volume fraction 0.25 to 0.75 for the instability development of the two mode Kelvin–Helmholtz test case captured by 5^{th} order Godunov method with low Mach correction for Mach number at 0.002 on grid resolution of 64×64

A.2 5^{th} order Godunov method without low Mach correction

The development of the Kelvin–Helmholtz instability captured on all grid resolutions, 24×24, 32×32, 48×48 and 64×64, for all Mach numbers, 0.2, 0.02 and 0.002, by 5^{th} order Godunov method without low Mach correction are included in this section.

A.2.1 Mach number at 0.2

A.2.1.1 Grid resolution 24×24

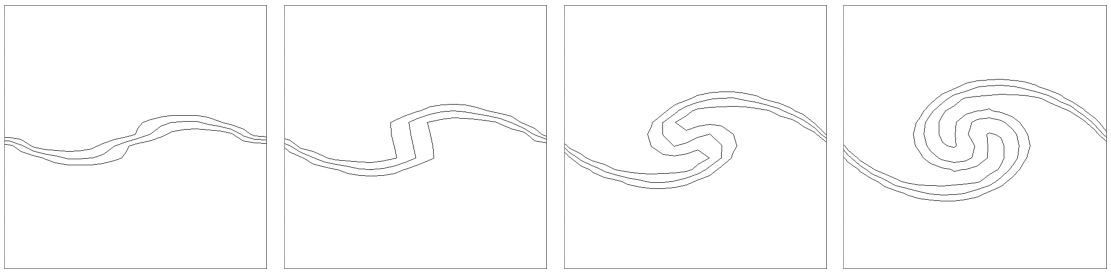

(a) t = 3s **(b)** t = 4s **(c)** t = 5s **(d)** t = 6s

Figure A.14: Contour lines of volume fraction 0.25 to 0.75 for the instability development of the two mode Kelvin–Helmholtz test case captured by 5^{th} order Godunov method without low Mach correction for Mach number at 0.2 on grid resolution of 24×24

A.2.1.2 Grid resolution 32×32

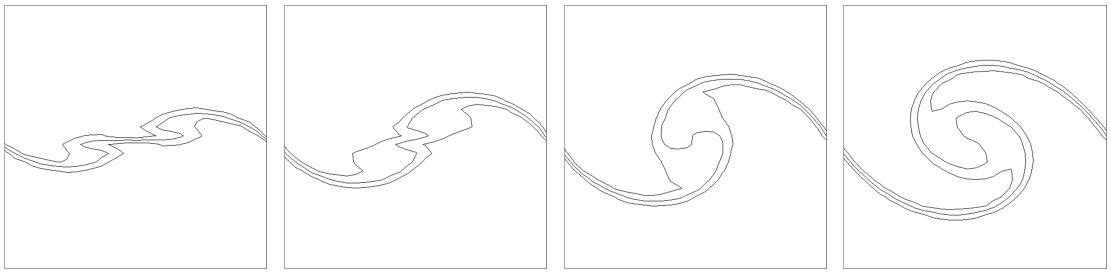

(a) t = 3s **(b)** t = 4s **(c)** t = 5s **(d)** t = 6s

Figure A.15: Contour lines of volume fraction 0.25 to 0.75 for the instability development of the two mode Kelvin–Helmholtz test case captured by 5^{th} order Godunov method without low Mach correction for Mach number at 0.2 on grid resolution of 32×32

A.2.1.3 Grid resolution 48×48

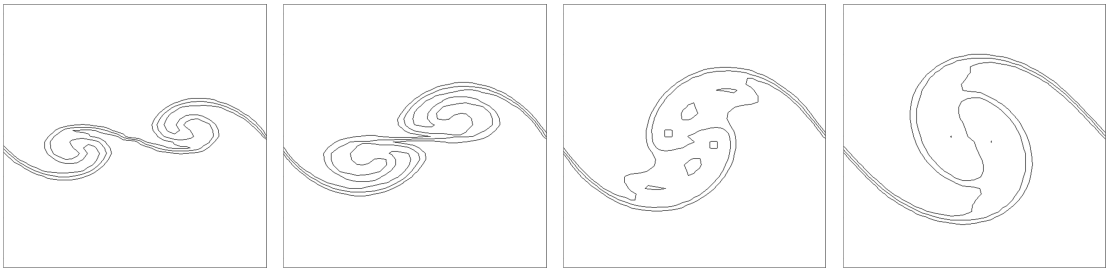

(a) t = 3s **(b)** t = 4s **(c)** t = 5s **(d)** t = 6s

Figure A.16: Contour lines of volume fraction 0.25 to 0.75 for the instability development of the two mode Kelvin–Helmholtz test case captured by 5^{th} order Godunov method without low Mach correction for Mach number at 0.2 on grid resolution of 48×48

A.2.1.4 Grid resolution 64×64

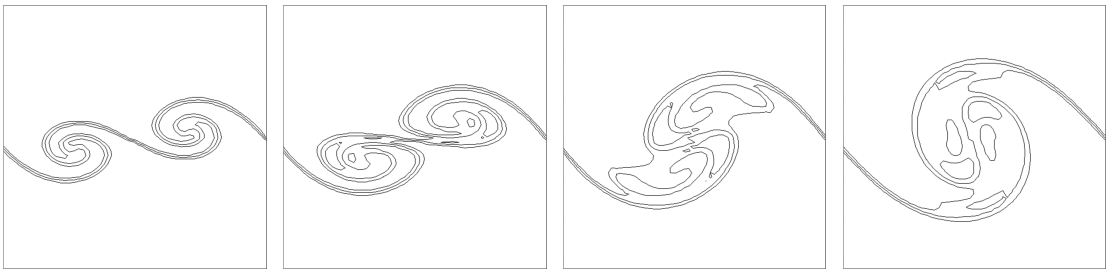

(a) t = 3s **(b)** t = 4s **(c)** t = 5s **(d)** t = 6s

Figure A.17: Contour lines of volume fraction 0.25 to 0.75 for the instability development of the two mode Kelvin–Helmholtz test case captured by 5^{th} order Godunov method without low Mach correction for Mach number at 0.2 on grid resolution of 64×64

A.2.2 Mach number at 0.02

A.2.2.1 Grid resolution 24×24

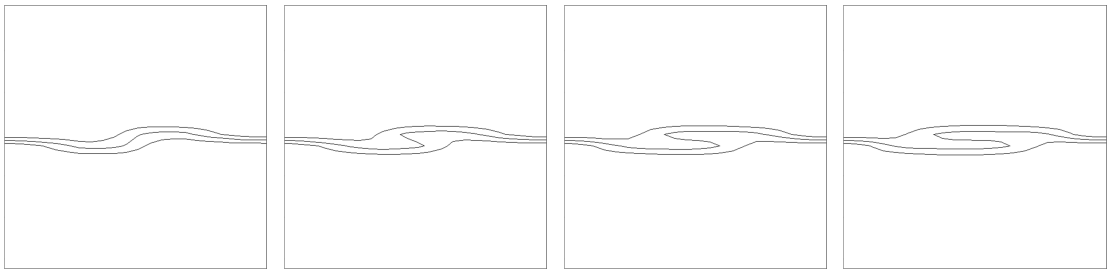

(a) t = 3s **(b)** t = 4s **(c)** t = 5s **(d)** t = 6s

Figure A.18: Contour lines of volume fraction 0.25 to 0.75 for the instability development of the two mode Kelvin–Helmholtz test case captured by 5^{th} order Godunov method without low Mach correction for Mach number at 0.02 on grid resolution of 24×24

A.2.2.2 Grid resolution 32×32

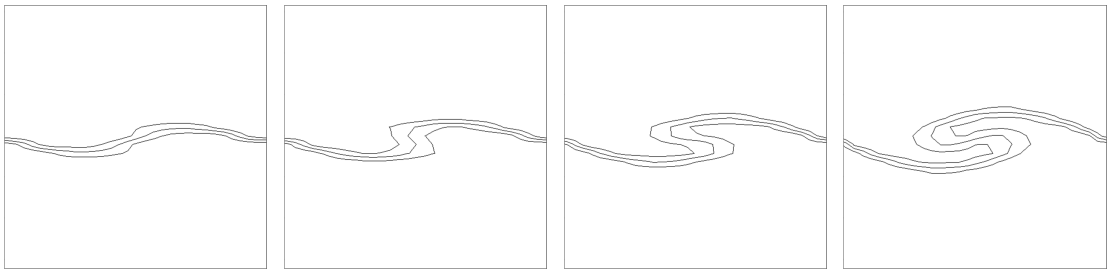

(a) t = 3s **(b)** t = 4s **(c)** t = 5s **(d)** t = 6s

Figure A.19: Contour lines of volume fraction 0.25 to 0.75 for the instability development of the two mode Kelvin–Helmholtz test case captured by 5^{th} order Godunov method without low Mach correction for Mach number at 0.02 on grid resolution of 32×32

A.2.2.3 Grid resolution 48×48

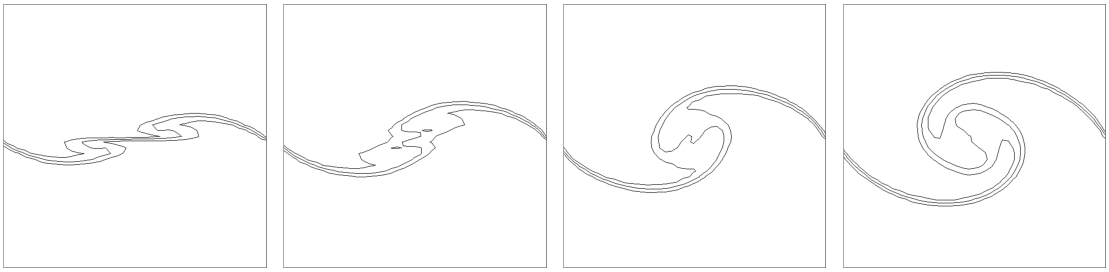

(a) t = 3s **(b)** t = 4s **(c)** t = 5s **(d)** t = 6s

Figure A.20: Contour lines of volume fraction 0.25 to 0.75 for the instability development of the two mode Kelvin–Helmholtz test case captured by 5^{th} order Godunov method without low Mach correction for Mach number at 0.02 on grid resolution of 48×48

A.2.2.4 Grid resolution 64×64

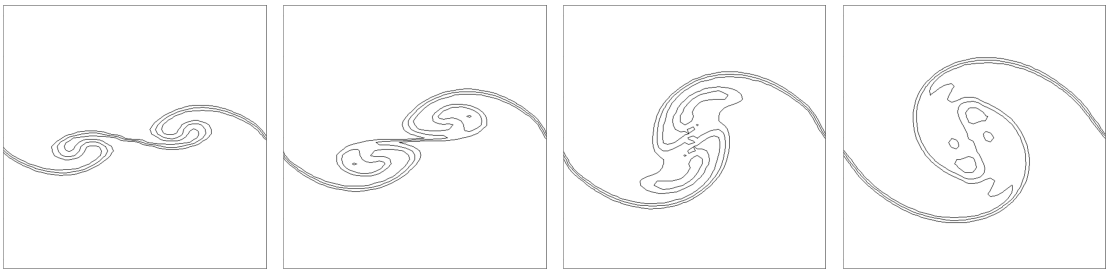

(a) t = 3s **(b)** t = 4s **(c)** t = 5s **(d)** t = 6s

Figure A.21: Contour lines of volume fraction 0.25 to 0.75 for the instability development of the two mode Kelvin–Helmholtz test case captured by 5^{th} order Godunov method without low Mach correction for Mach number at 0.02 on grid resolution of 64×64

A.2.3 Mach number at 0.002

A.2.3.1 Grid resolution 24×24

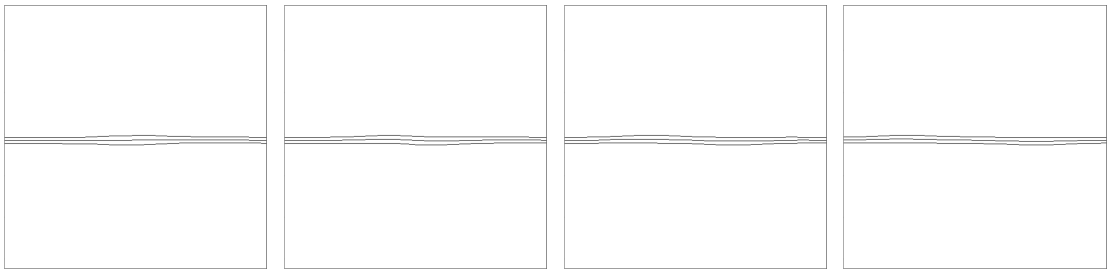

(a) t = 3s **(b)** t = 4s **(c)** t = 5s **(d)** t = 6s

Figure A.22: Contour lines of volume fraction 0.25 to 0.75 for the instability development of the two mode Kelvin–Helmholtz test case captured by 5^{th} order Godunov method without low Mach correction for Mach number at 0.002 on grid resolution of 24×24

A.2.3.2 Grid resolution 32×32

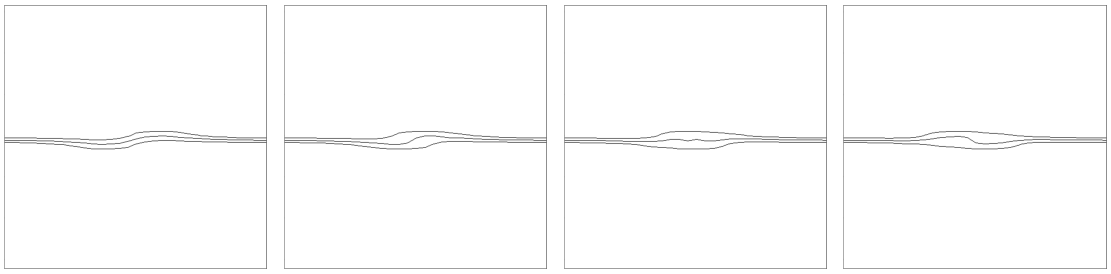

(a) t = 3s **(b)** t = 4s **(c)** t = 5s **(d)** t = 6s

Figure A.23: Contour lines of volume fraction 0.25 to 0.75 for the instability development of the two mode Kelvin–Helmholtz test case captured by 5^{th} order Godunov method without low Mach correction for Mach number at 0.002 on grid resolution of 32×32

A.2.3.3 Grid resolution 48×48

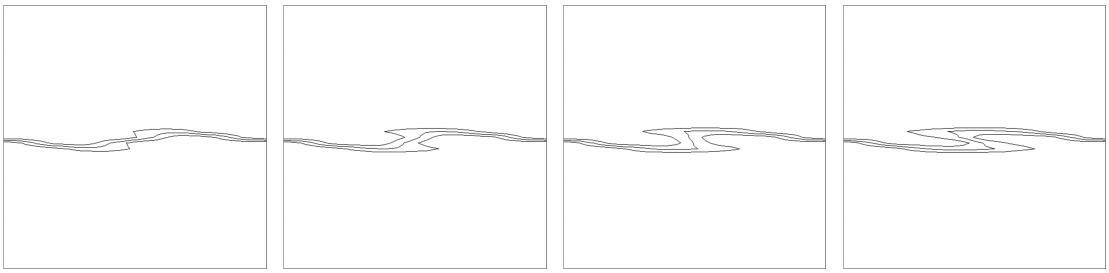

(a) t = 3s **(b)** t = 4s **(c)** t = 5s **(d)** t = 6s

Figure A.24: Contour lines of volume fraction 0.25 to 0.75 for the instability development of the two mode Kelvin–Helmholtz test case captured by 5^{th} order Godunov method without low Mach correction for Mach number at 0.002 on grid resolution of 48×48

A.2.3.4 Grid resolution 64×64

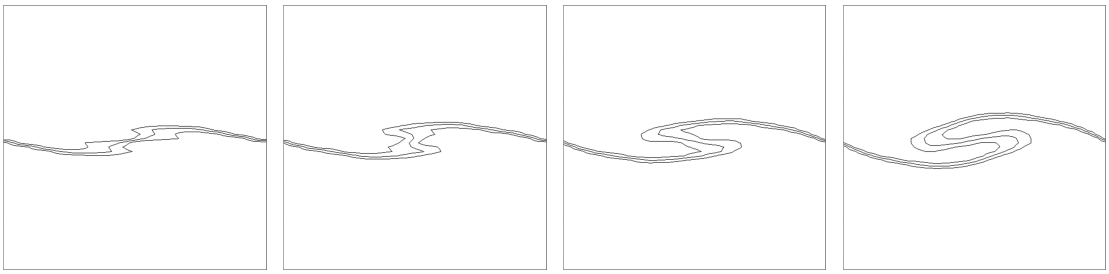

(a) t = 3s **(b)** t = 4s **(c)** t = 5s **(d)** t = 6s

Figure A.25: Contour lines of volume fraction 0.25 to 0.75 for the instability development of the two mode Kelvin–Helmholtz test case captured by 5^{th} order Godunov method without low Mach correction for Mach number at 0.002 on grid resolution of 64×64

Appendix B

Vortex pairing - 2^{nd} order Godunov method

B.1 2^{nd} order Godunov method with low Mach correction

The development of the Kelvin–Helmholtz instability captured on all grid resolutions, 24×24, 32×32, 48×48 and 64×64, for all Mach numbers, 0.2, 0.02 and 0.002, by 2^{nd} order Godunov method with low Mach correction are included in this section.

B.1.1 Mach number at 0.2

B.1.1.1 Grid resolution 24×24

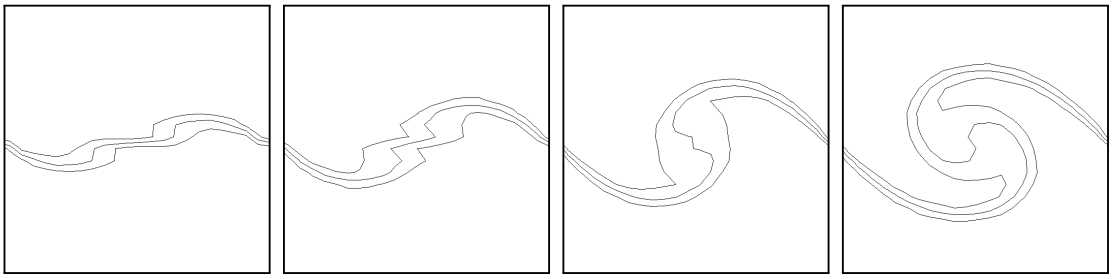

(a) t = 3s **(b)** t = 4s **(c)** t = 5s **(d)** t = 6s

Figure B.1: Contour lines of volume fraction 0.25 to 0.75 for the instability development of the two mode Kelvin–Helmholtz test case captured by 2^{nd} order Godunov method with low Mach correction for Mach number at 0.2 on grid resolution of 24×24

B.1.1.2 Grid resolution 32×32

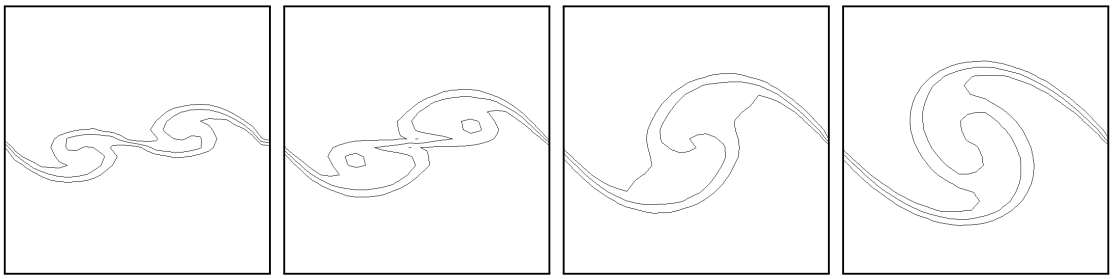

(a) t = 3s **(b)** t = 4s **(c)** t = 5s **(d)** t = 6s

Figure B.2: Contour lines of volume fraction 0.25 to 0.75 for the instability development of the two mode Kelvin–Helmholtz test case captured by 2nd order Godunov method with low Mach correction for Mach number at 0.2 on grid resolution of 32×32

B.1.1.3 Grid resolution 48×48

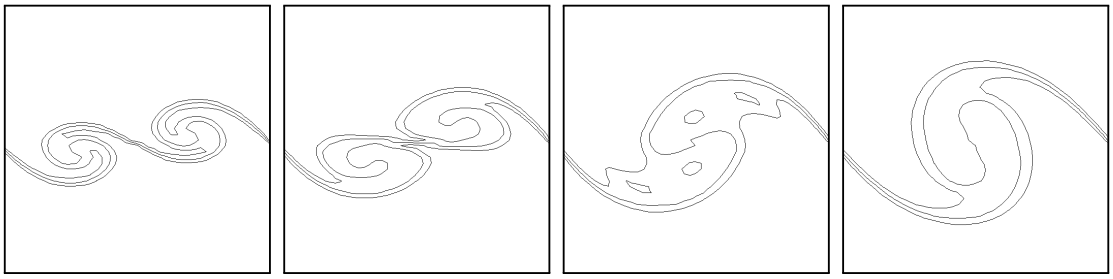

(a) t = 3s **(b)** t = 4s **(c)** t = 5s **(d)** t = 6s

Figure B.3: Contour lines of volume fraction 0.25 to 0.75 for the instability development of the two mode Kelvin–Helmholtz test case captured by 2nd order Godunov method with low Mach correction for Mach number at 0.2 on grid resolution of 48×48

B.1.1.4 Grid resolution 64×64

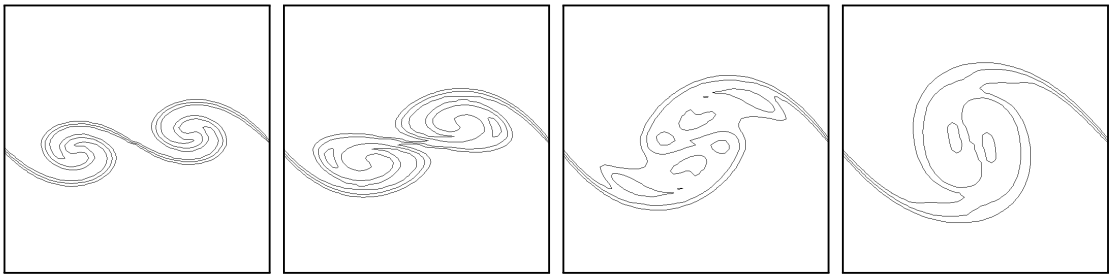

(a) t = 3s **(b)** t = 4s **(c)** t = 5s **(d)** t = 6s

Figure B.4: Contour lines of volume fraction 0.25 to 0.75 for the instability development of the two mode Kelvin–Helmholtz test case captured by 2nd order Godunov method with low Mach correction for Mach number at 0.2 on grid resolution of 64×64

B.1.2 Mach number at 0.02

B.1.2.1 Grid resolution 24×24

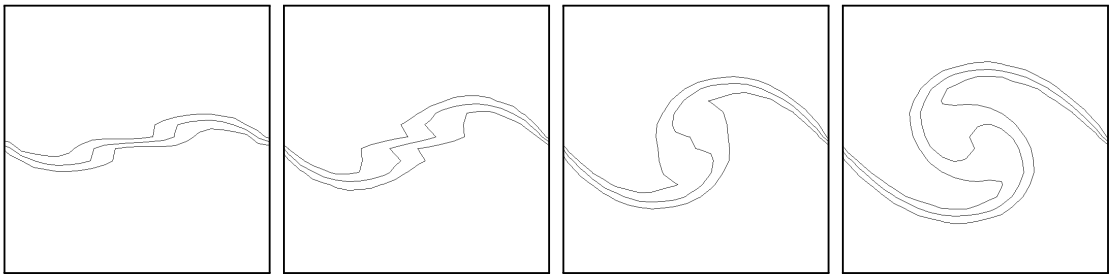

(a) t = 3s **(b)** t = 4s **(c)** t = 5s **(d)** t = 6s

Figure B.5: Contour lines of volume fraction 0.25 to 0.75 for the instability development of the two mode Kelvin–Helmholtz test case captured by 2nd order Godunov method with low Mach correction for Mach number at 0.02 on grid resolution of 24×24

B.1.2.2 Grid resolution 32×32

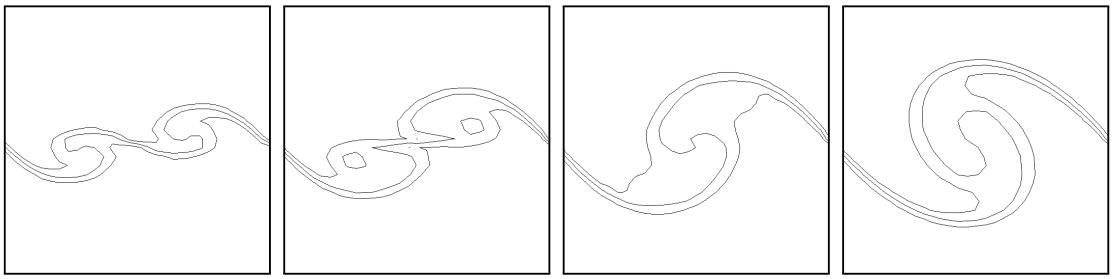

(a) t = 3s **(b)** t = 4s **(c)** t = 5s **(d)** t = 6s

Figure B.6: Contour lines of volume fraction 0.25 to 0.75 for the instability development of the two mode Kelvin–Helmholtz test case captured by 2nd order Godunov method with low Mach correction for Mach number at 0.02 on grid resolution of 32×32

B.1.2.3 Grid resolution 48×48

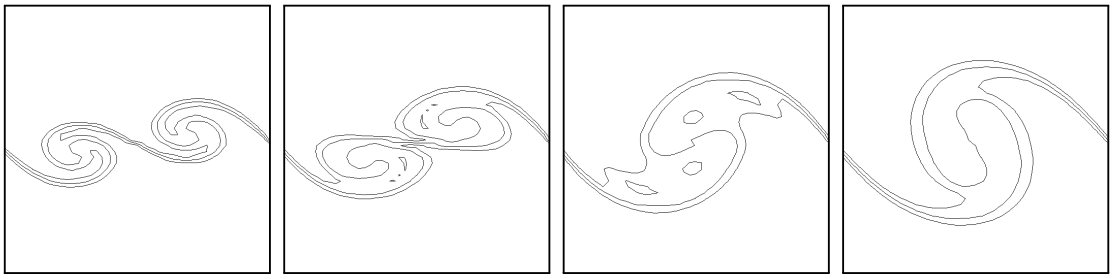

(a) t = 3s **(b)** t = 4s **(c)** t = 5s **(d)** t = 6s

Figure B.7: Contour lines of volume fraction 0.25 to 0.75 for the instability development of the two mode Kelvin–Helmholtz test case captured by 2nd order Godunov method with low Mach correction for Mach number at 0.02 on grid resolution of 48×48

B.1.2.4 Grid resolution 64×64

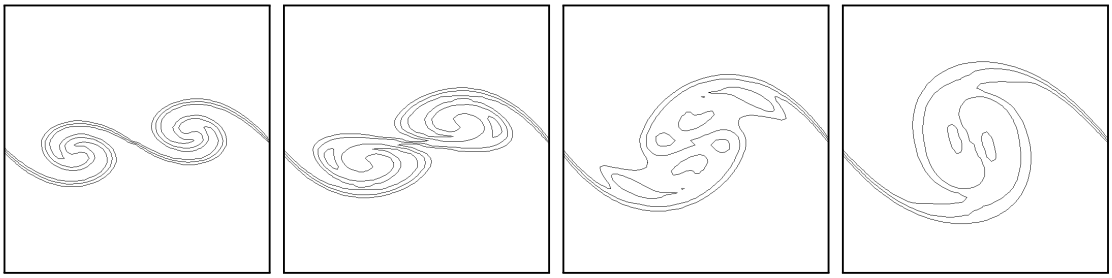

(a) t = 3s **(b)** t = 4s **(c)** t = 5s **(d)** t = 6s

Figure B.8: Contour lines of volume fraction 0.25 to 0.75 for the instability development of the two mode Kelvin–Helmholtz test case captured by 2nd order Godunov method with low Mach correction for Mach number at 0.02 on grid resolution of 64×64

B.1.3 Mach number at 0.002

B.1.3.1 Grid resolution 24×24

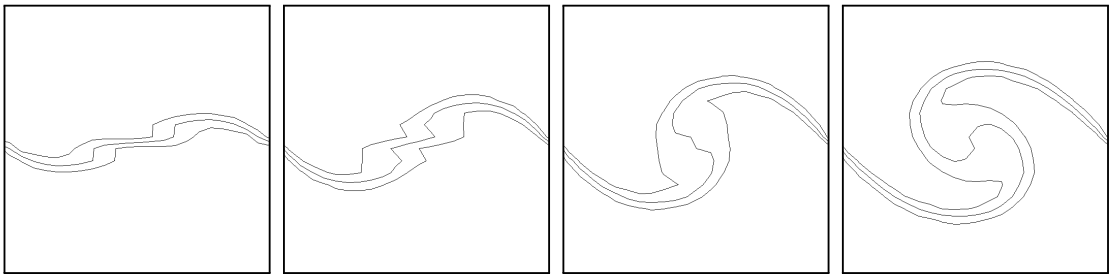

(a) t = 3s **(b)** t = 4s **(c)** t = 5s **(d)** t = 6s

Figure B.9: Contour lines of volume fraction 0.25 to 0.75 for the instability development of the two mode Kelvin–Helmholtz test case captured by 2nd order Godunov method with low Mach correction for Mach number at 0.002 on grid resolution of 24×24

B.1.3.2 Grid resolution 32×32

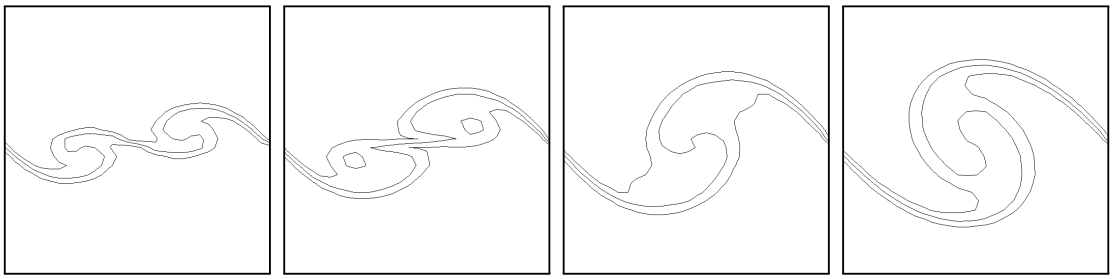

(a) t = 3s **(b)** t = 4s **(c)** t = 5s **(d)** t = 6s

Figure B.10: Contour lines of volume fraction 0.25 to 0.75 for the instability development of the two mode Kelvin–Helmholtz test case captured by 2nd order Godunov method with low Mach correction for Mach number at 0.002 on grid resolution of 32×32

B.1.3.3 Grid resolution 48×48

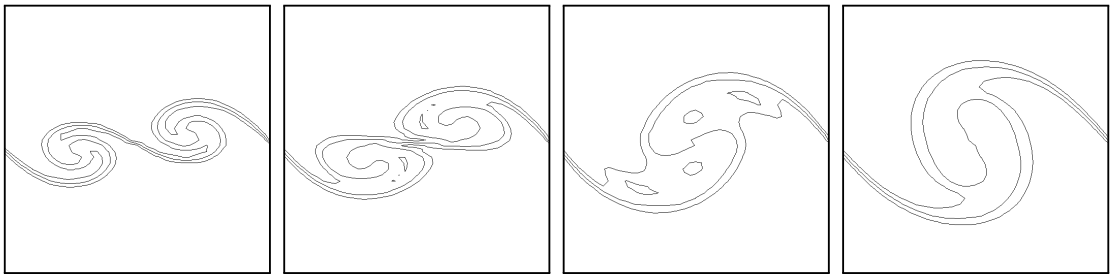

(a) t = 3s **(b)** t = 4s **(c)** t = 5s **(d)** t = 6s

Figure B.11: Contour lines of volume fraction 0.25 to 0.75 for the instability development of the two mode Kelvin–Helmholtz test case captured by 2nd order Godunov method with low Mach correction for Mach number at 0.002 on grid resolution of 48×48

B.1.3.4 Grid resolution 64×64

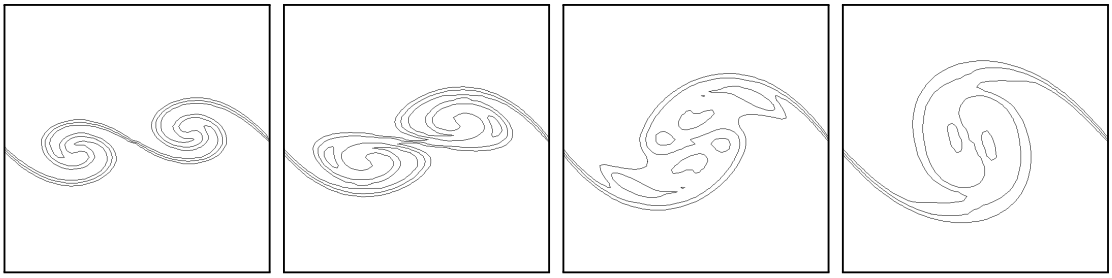

(a) t = 3s **(b)** t = 4s **(c)** t = 5s **(d)** t = 6s

Figure B.12: Contour lines of volume fraction 0.25 to 0.75 for the instability development of the two mode Kelvin–Helmholtz test case captured by 2nd order Godunov method with low Mach correction for Mach number at 0.002 on grid resolution of 64×64

B.2 2nd order Godunov method without low Mach correction

The development of the Kelvin–Helmholtz instability captured on all grid resolutions, 24×24, 32×32, 48×48 and 64×64, for all Mach numbers, 0.2, 0.02 and 0.002, by 2nd order Godunov method without low Mach correction are included in this section.

B.2.1 Mach number at 0.2

B.2.1.1 Grid resolution 24×24

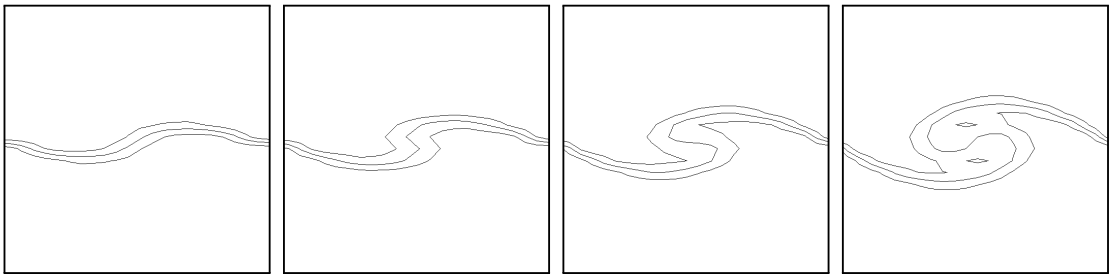

(a) t = 3s **(b)** t = 4s **(c)** t = 5s **(d)** t = 6s

Figure B.13: Contour lines of volume fraction 0.25 to 0.75 for the instability development of the two mode Kelvin–Helmholtz test case captured by 2nd order Godunov method without low Mach correction for Mach number at 0.2 on grid resolution of 24×24

B.2.1.2 Grid resolution 32×32

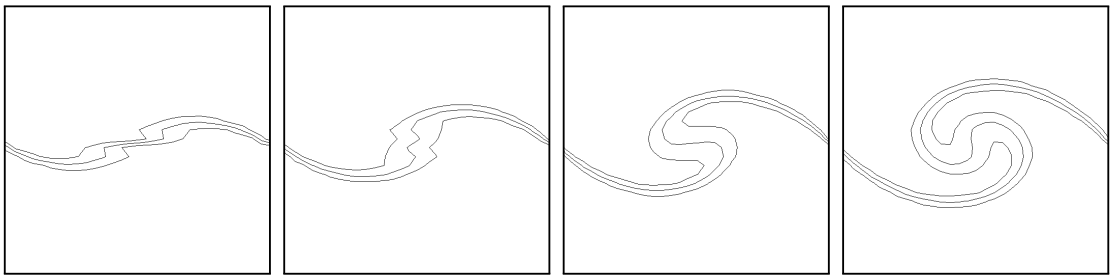

(a) t = 3s **(b)** t = 4s **(c)** t = 5s **(d)** t = 6s

Figure B.14: Contour lines of volume fraction 0.25 to 0.75 for the instability development of the two mode Kelvin–Helmholtz test case captured by 2nd order Godunov method without low Mach correction for Mach number at 0.2 on grid resolution of 32×32

B.2.1.3 Grid resolution 48×48

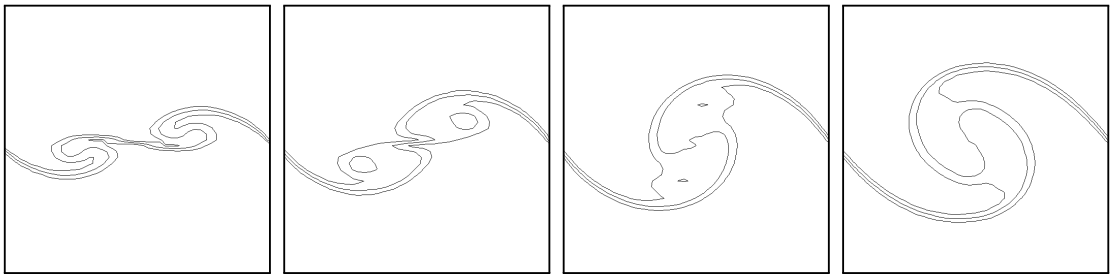

(a) t = 3s **(b)** t = 4s **(c)** t = 5s **(d)** t = 6s

Figure B.15: Contour lines of volume fraction 0.25 to 0.75 for the instability development of the two mode Kelvin–Helmholtz test case captured by 2nd order Godunov method without low Mach correction for Mach number at 0.2 on grid resolution of 48×48

B.2.1.4 Grid resolution 64×64

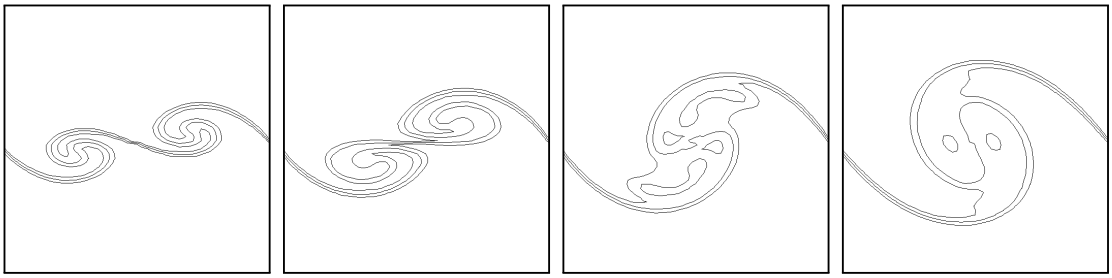

(a) t = 3s **(b)** t = 4s **(c)** t = 5s **(d)** t = 6s

Figure B.16: Contour lines of volume fraction 0.25 to 0.75 for the instability development of the two mode Kelvin–Helmholtz test case captured by 2nd order Godunov method without low Mach correction for Mach number at 0.2 on grid resolution of 64×64

B.2.2 Mach number at 0.02

B.2.2.1 Grid resolution 24×24

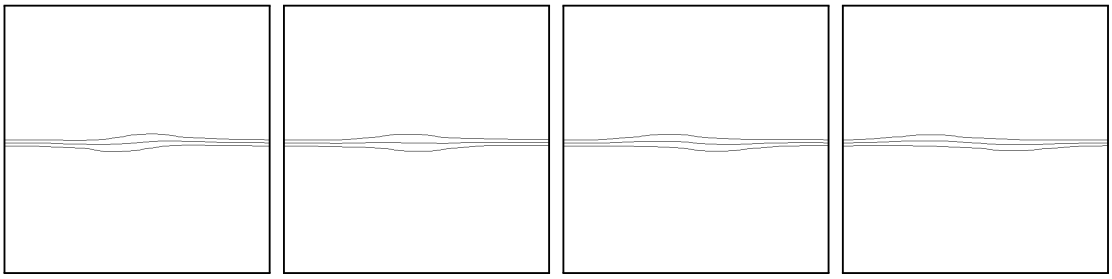

(a) t = 3s **(b)** t = 4s **(c)** t = 5s **(d)** t = 6s

Figure B.17: Contour lines of volume fraction 0.25 to 0.75 for the instability development of the two mode Kelvin–Helmholtz test case captured by 2nd order Godunov method without low Mach correction for Mach number at 0.02 on grid resolution of 24×24

B.2.2.2 Grid resolution 32×32

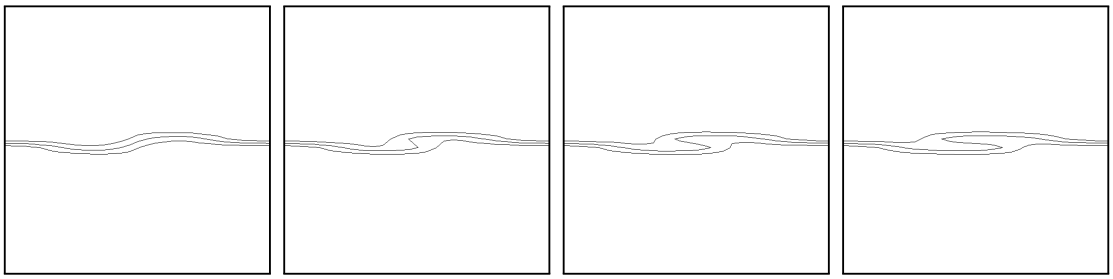

(a) t = 3s **(b)** t = 4s **(c)** t = 5s **(d)** t = 6s

Figure B.18: Contour lines of volume fraction 0.25 to 0.75 for the instability development of the two mode Kelvin–Helmholtz test case captured by 2nd order Godunov method without low Mach correction for Mach number at 0.02 on grid resolution of 32×32

B.2.2.3 Grid resolution 48×48

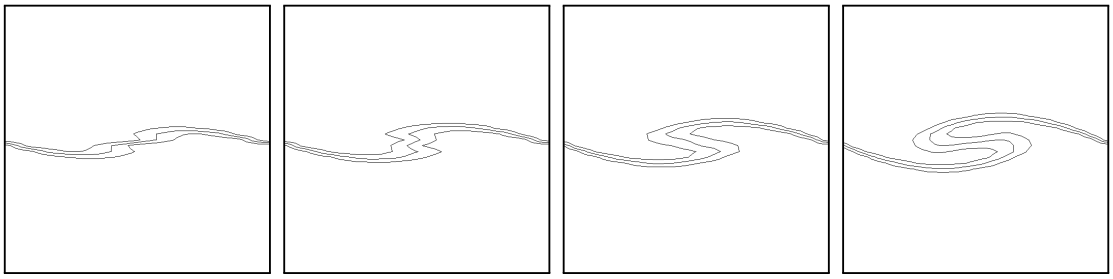

(a) t = 3s **(b)** t = 4s **(c)** t = 5s **(d)** t = 6s

Figure B.19: Contour lines of volume fraction 0.25 to 0.75 for the instability development of the two mode Kelvin–Helmholtz test case captured by 2nd order Godunov method without low Mach correction for Mach number at 0.02 on grid resolution of 48×48

B.2.2.4 Grid resolution 64×64

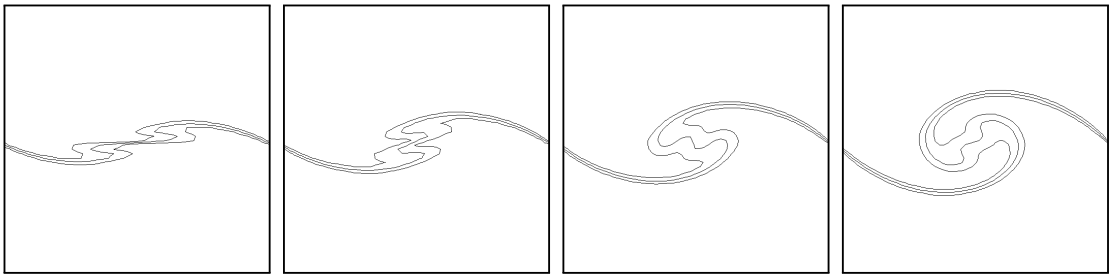

(a) t = 3s **(b)** t = 4s **(c)** t = 5s **(d)** t = 6s

Figure B.20: Contour lines of volume fraction 0.25 to 0.75 for the instability development of the two mode Kelvin–Helmholtz test case captured by 2nd order Godunov method without low Mach correction for Mach number at 0.02 on grid resolution of 64×64

B.2.3 Mach number at 0.002

B.2.3.1 Grid resolution 24×24

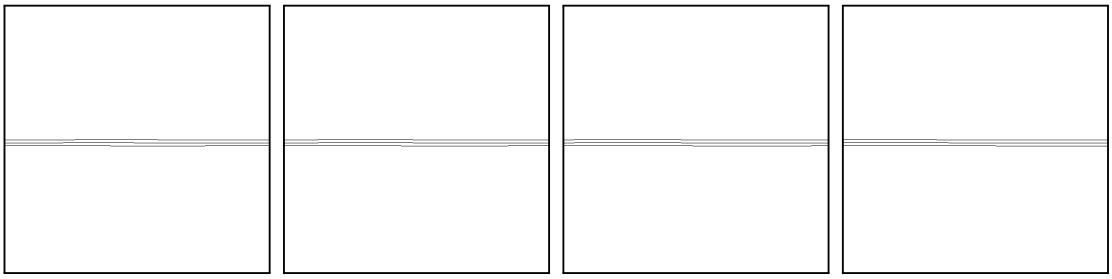

(a) t = 3s **(b)** t = 4s **(c)** t = 5s **(d)** t = 6s

Figure B.21: Contour lines of volume fraction 0.25 to 0.75 for the instability development of the two mode Kelvin–Helmholtz test case captured by 2nd order Godunov method without low Mach correction for Mach number at 0.002 on grid resolution of 24×24

B.2.3.2 Grid resolution 32×32

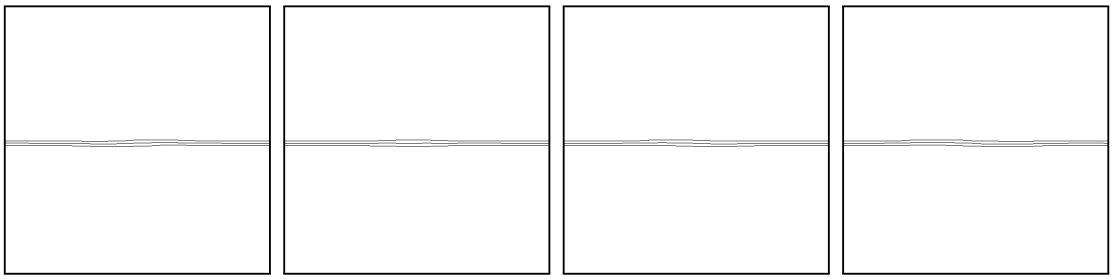

(a) t = 3s **(b)** t = 4s **(c)** t = 5s **(d)** t = 6s

Figure B.22: Contour lines of volume fraction 0.25 to 0.75 for the instability development of the two mode Kelvin–Helmholtz test case captured by 2nd order Godunov method without low Mach correction for Mach number at 0.002 on grid resolution of 32×32

B.2.3.3 Grid resolution 48×48

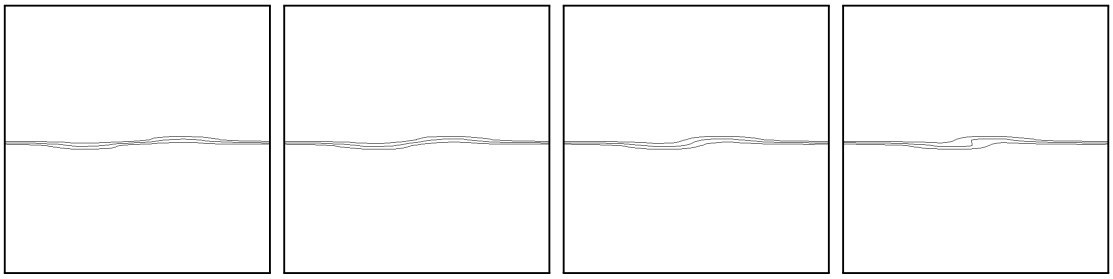

(a) t = 3s **(b)** t = 4s **(c)** t = 5s **(d)** t = 6s

Figure B.23: Contour lines of volume fraction 0.25 to 0.75 for the instability development of the two mode Kelvin–Helmholtz test case captured by 2nd order Godunov method without low Mach correction for Mach number at 0.002 on grid resolution of 48×48

B.2.3.4 Grid resolution 64×64

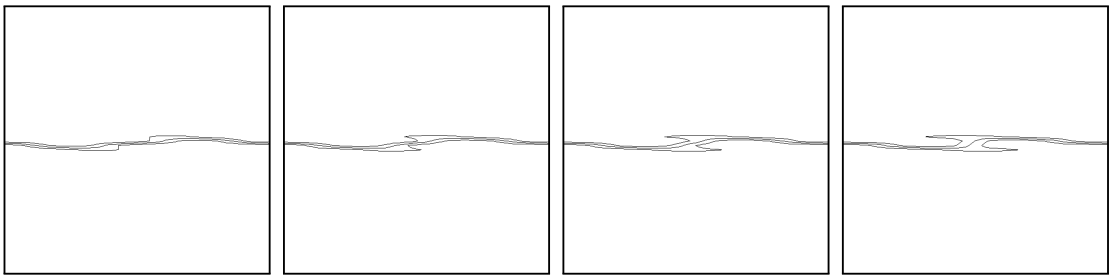

(a) t = 3s **(b)** t = 4s **(c)** t = 5s **(d)** t = 6s

Figure B.24: Contour lines of volume fraction 0.25 to 0.75 for the instability development of the two mode Kelvin–Helmholtz test case captured by 2^{nd} order Godunov method without low Mach correction for Mach number at 0.002 on grid resolution of 64×64

Appendix C

Vortex pairing - TURMOIL

C.1 3^{rd} order accurate Lagrange-remap method

The development of the Kelvin–Helmholtz instability captured on grid resolutions 32×32 and 64×64, for Mach number of 0.2 by 3^{rd} order accurate Lagrange-remap method are included in this section [14].

C.1.1 Mach number at 0.2

C.1.1.1 Grid resolution 32×32

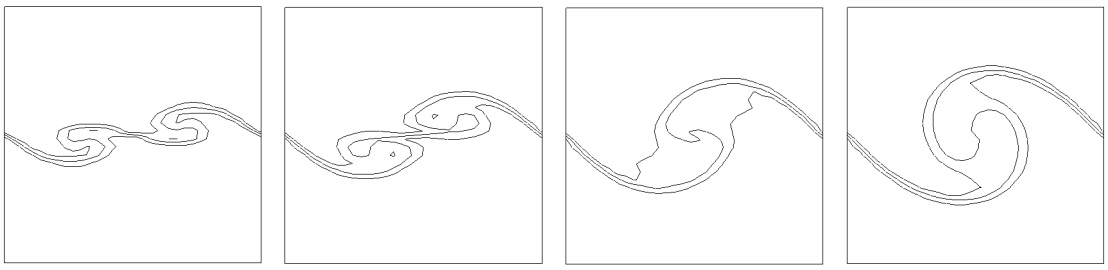

(a) t = 3s **(b)** t = 4s **(c)** t = 5s **(d)** t = 6s

Figure C.1: Contour lines of volume fraction 0.25 to 0.75 for the instability development of the two mode Kelvin–Helmholtz test case captured by 3^{rd} order accurate Lagrange-remap method for Mach number at 0.2 on grid resolution of 32×32 [14]

C.1.1.2 Grid resolution 64×64

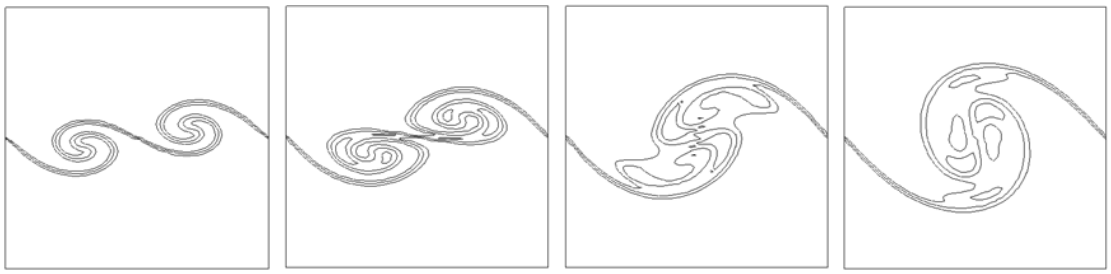

(a) t = 3s **(b)** t = 4s **(c)** t = 5s **(d)** t = 6s

Figure C.2: Contour lines of volume fraction 0.25 to 0.75 for the instability development of the two mode Kelvin–Helmholtz test case captured by 3rd order accurate Lagrange-remap method for Mach number at 0.2 on grid resolution of 64×64 [14]

Appendix D

Vortex pairing - ANSYS Fluent

D.1 ANSYS Fluent with implicit time stepping method

The development of the Kelvin–Helmholtz instability captured on all grid resolutions, 24×24, 32×32, 48×48 and 64×64, for all Mach numbers, 0.2, 0.02 and 0.002, by ANSYS Fluent with implicit time stepping method are included in this section.

D.1.1 Mach number at 0.2

D.1.1.1 Grid resolution 24×24

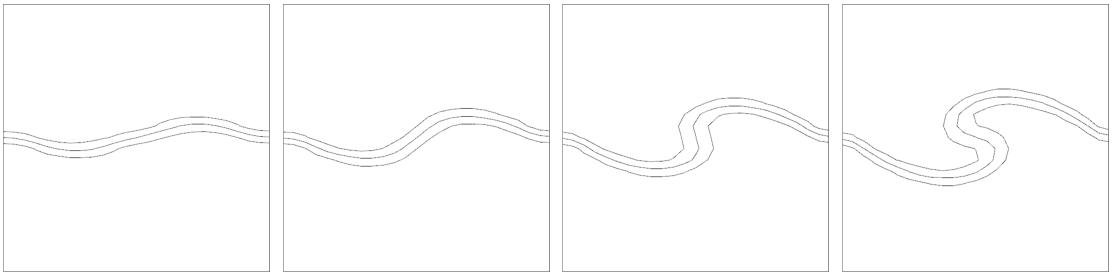

(a) t = 3s **(b)** t = 4s **(c)** t = 5s **(d)** t = 6s

Figure D.1: Contour lines of volume fraction 0.25 to 0.75 for the instability development of the two mode Kelvin–Helmholtz test case captured by compressible flow solver of ANSYS Fluent with implicit time stepping method for Mach number at 0.2 on grid resolution of 24×24

D.1.1.2 Grid resolution 32×32

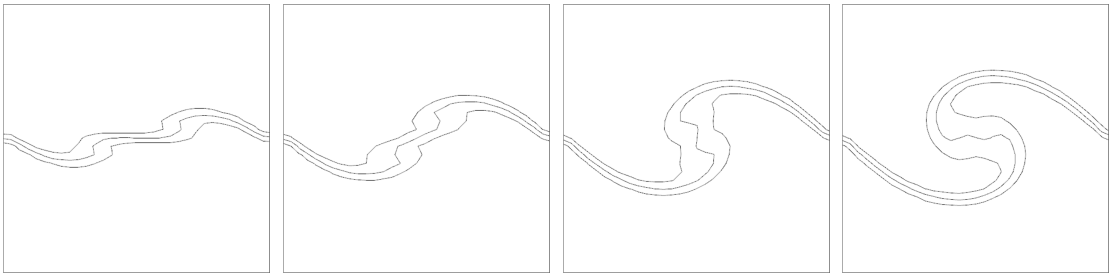

(a) t = 3s **(b)** t = 4s **(c)** t = 5s **(d)** t = 6s

Figure D.2: Contour lines of volume fraction 0.25 to 0.75 for the instability development of the two mode Kelvin–Helmholtz test case captured by compressible flow solver of ANSYS Fluent with implicit time stepping method for Mach number at 0.2 on grid resolution of 32×32

D.1.1.3 Grid resolution 48×48

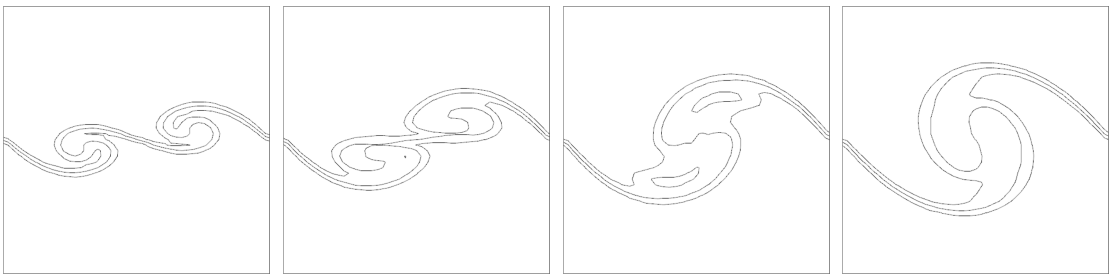

(a) t = 3s **(b)** t = 4s **(c)** t = 5s **(d)** t = 6s

Figure D.3: Contour lines of volume fraction 0.25 to 0.75 for the instability development of the two mode Kelvin–Helmholtz test case captured by compressible flow solver of ANSYS Fluent with implicit time stepping method for Mach number at 0.2 on grid resolution of 48×48

D.1.1.4 Grid resolution 64×64

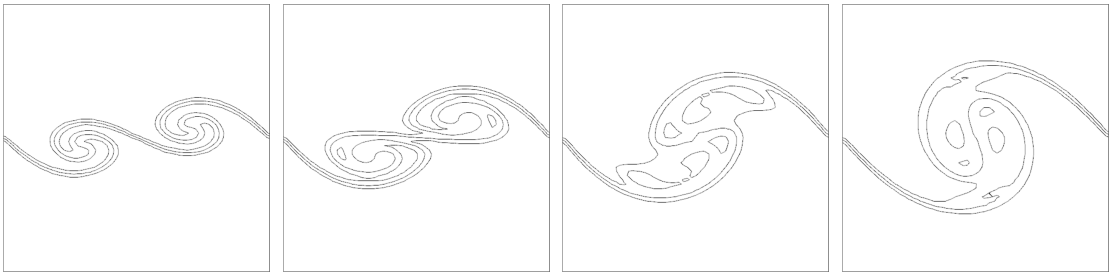

(a) t = 3s **(b)** t = 4s **(c)** t = 5s **(d)** t = 6s

Figure D.4: Contour lines of volume fraction 0.25 to 0.75 for the instability development of the two mode Kelvin–Helmholtz test case captured by compressible flow solver of ANSYS Fluent with implicit time stepping method for Mach number at 0.2 on grid resolution of 64×64

D.1.2 Mach number at 0.02

D.1.2.1 Grid resolution 24×24

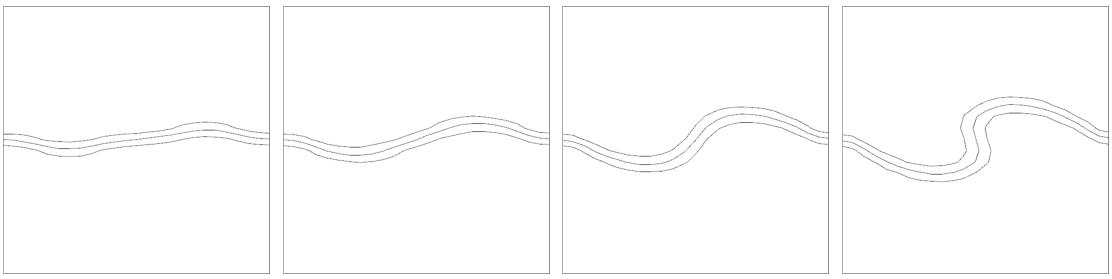

(a) t = 3s **(b)** t = 4s **(c)** t = 5s **(d)** t = 6s

Figure D.5: Contour lines of volume fraction 0.25 to 0.75 for the instability development of the two mode Kelvin–Helmholtz test case captured by compressible flow solver of ANSYS Fluent with implicit time stepping method for Mach number at 0.02 on grid resolution of 24×24

D.1.2.2 Grid resolution 32×32

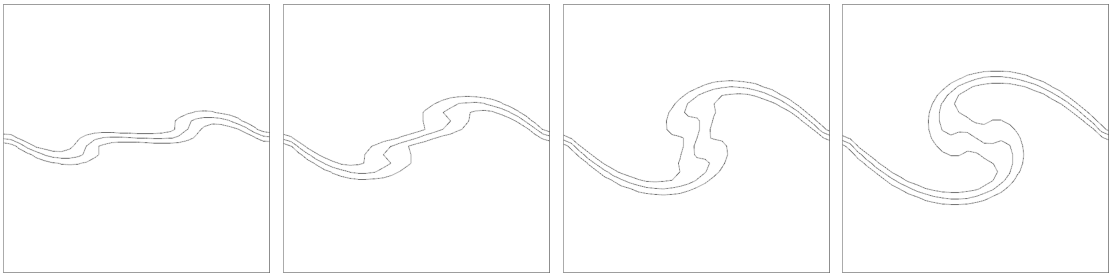

(a) t = 3s **(b)** t = 4s **(c)** t = 5s **(d)** t = 6s

Figure D.6: Contour lines of volume fraction 0.25 to 0.75 for the instability development of the two mode Kelvin–Helmholtz test case captured by compressible flow solver of ANSYS Fluent with implicit time stepping method for Mach number at 0.02 on grid resolution of 32×32

D.1.2.3 Grid resolution 48×48

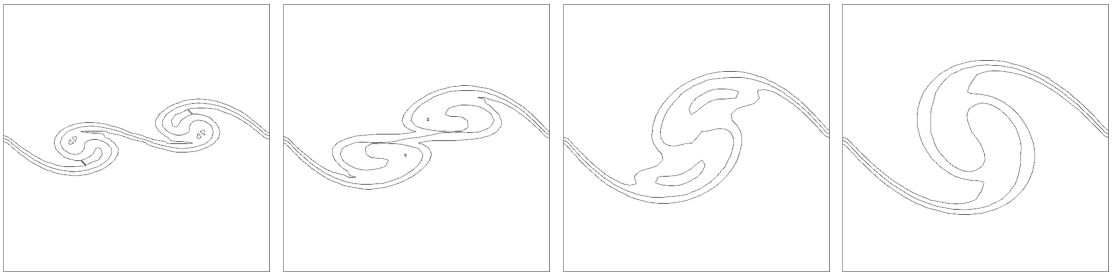

(a) t = 3s **(b)** t = 4s **(c)** t = 5s **(d)** t = 6s

Figure D.7: Contour lines of volume fraction 0.25 to 0.75 for the instability development of the two mode Kelvin–Helmholtz test case captured by compressible flow solver of ANSYS Fluent with implicit time stepping method for Mach number at 0.02 on grid resolution of 48×48

D.1.2.4 Grid resolution 64×64

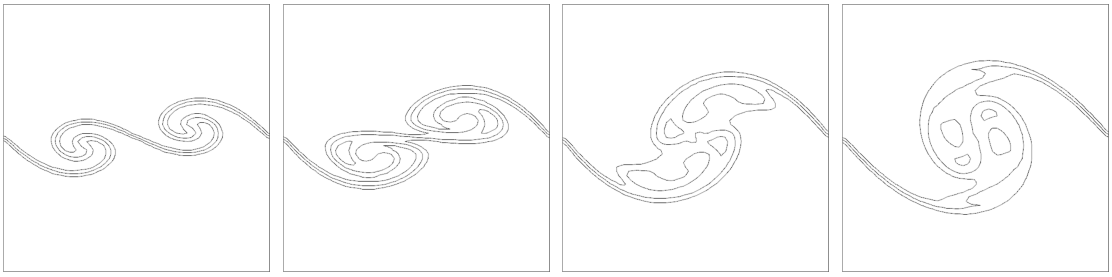

(a) t = 3s **(b)** t = 4s **(c)** t = 5s **(d)** t = 6s

Figure D.8: Contour lines of volume fraction 0.25 to 0.75 for the instability development of the two mode Kelvin–Helmholtz test case captured by compressible flow solver of ANSYS Fluent with implicit time stepping method for Mach number at 0.02 on grid resolution of 64×64

D.1.3 Mach number at 0.002

D.1.3.1 Grid resolution 24×24

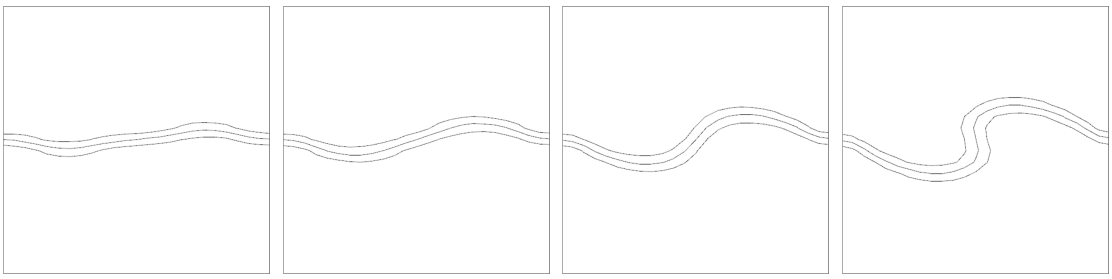

(a) t = 3s **(b)** t = 4s **(c)** t = 5s **(d)** t = 6s

Figure D.9: Contour lines of volume fraction 0.25 to 0.75 for the instability development of the two mode Kelvin–Helmholtz test case captured by compressible flow solver of ANSYS Fluent with implicit time stepping method for Mach number at 0.002 on grid resolution of 24×24

D.1.3.2 Grid resolution 32×32

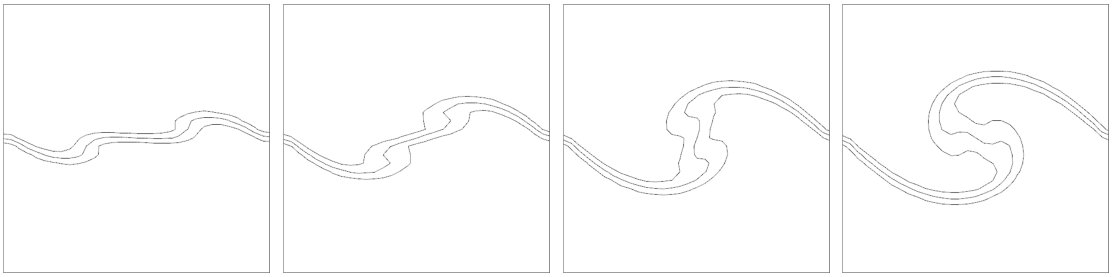

(a) t = 3s **(b)** t = 4s **(c)** t = 5s **(d)** t = 6s

Figure D.10: Contour lines of volume fraction 0.25 to 0.75 for the instability development of the two mode Kelvin–Helmholtz test case captured by compressible flow solver of ANSYS Fluent with implicit time stepping method for Mach number at 0.002 on grid resolution of 32×32

D.1.3.3 Grid resolution 48×48

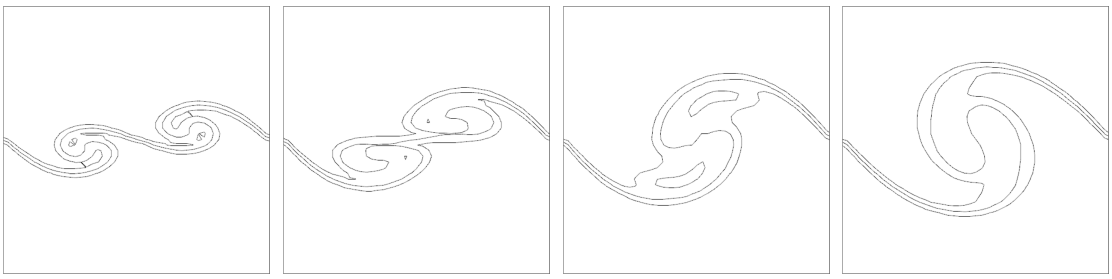

(a) t = 3s **(b)** t = 4s **(c)** t = 5s **(d)** t = 6s

Figure D.11: Contour lines of volume fraction 0.25 to 0.75 for the instability development of the two mode Kelvin–Helmholtz test case captured by compressible flow solver of ANSYS Fluent with implicit time stepping method for Mach number at 0.002 on grid resolution of 48×48

D.1.3.4 Grid resolution 64×64

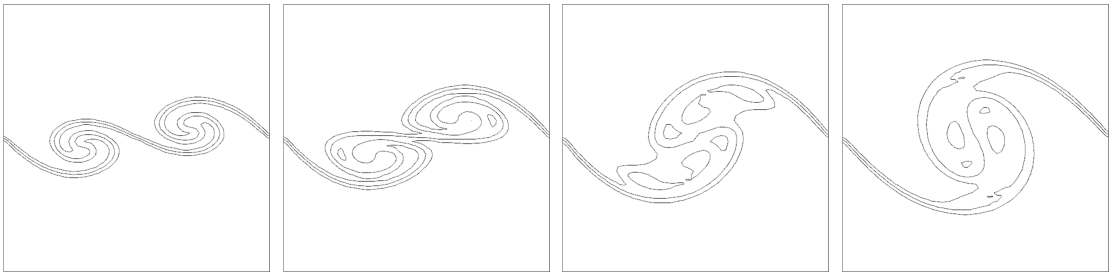

(a) t = 3s **(b)** t = 4s **(c)** t = 5s **(d)** t = 6s

Figure D.12: Contour lines of volume fraction 0.25 to 0.75 for the instability development of the two mode Kelvin–Helmholtz test case captured by compressible flow solver of ANSYS Fluent with implicit time stepping method for Mach number at 0.002 on grid resolution of 64×64

D.2 ANSYS Fluent with explicit time stepping method

The development of the Kelvin–Helmholtz instability captured on all grid resolutions, 24×24, 32×32, 48×48 and 64×64, for Mach numbers, 0.2 and 0.02, by ANSYS Fluent with explicit time stepping method are included in this section.

D.2.1 Mach number at 0.2

D.2.1.1 Grid resolution 24×24

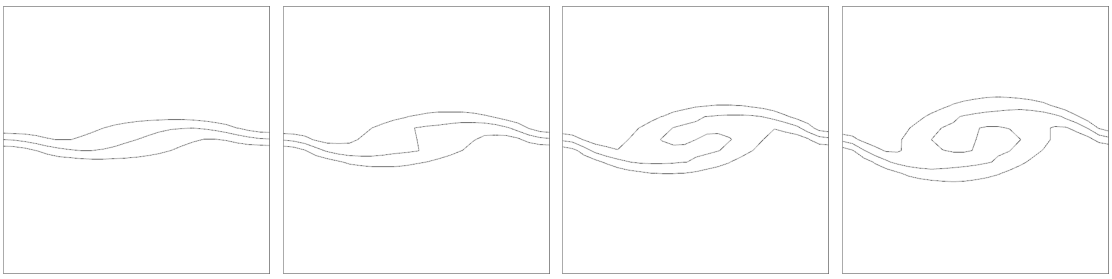

(a) t = 3s **(b)** t = 4s **(c)** t = 5s **(d)** t = 6s

Figure D.13: Contour lines of volume fraction 0.25 to 0.75 for the instability development of the two mode Kelvin–Helmholtz test case captured by compressible flow solver of ANSYS Fluent with explicit time stepping method for Mach number at 0.2 on grid resolution of 24×24

D.2.1.2 Grid resolution 32×32

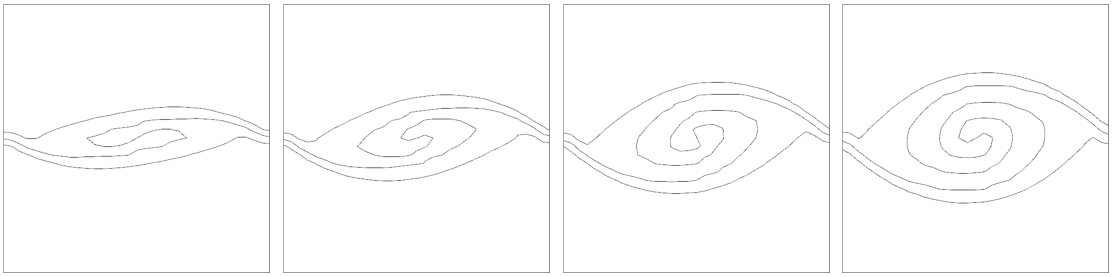

(a) t = 3s **(b)** t = 4s **(c)** t = 5s **(d)** t = 6s

Figure D.14: Contour lines of volume fraction 0.25 to 0.75 for the instability development of the two mode Kelvin–Helmholtz test case captured by compressible flow solver of ANSYS Fluent with explicit time stepping method for Mach number at 0.2 on grid resolution of 32×32

D.2.1.3 Grid resolution 48×48

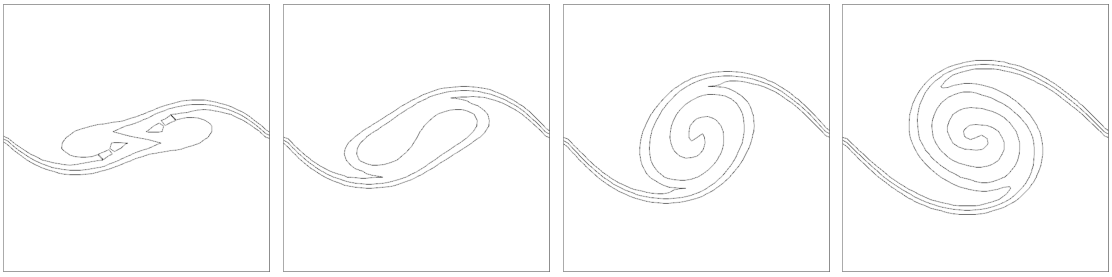

(a) t = 3s **(b)** t = 4s **(c)** t = 5s **(d)** t = 6s

Figure D.15: Contour lines of volume fraction 0.25 to 0.75 for the instability development of the two mode Kelvin–Helmholtz test case captured by compressible flow solver of ANSYS Fluent with explicit time stepping method for Mach number at 0.2 on grid resolution of 48×48

D.2.1.4 Grid resolution 64×64

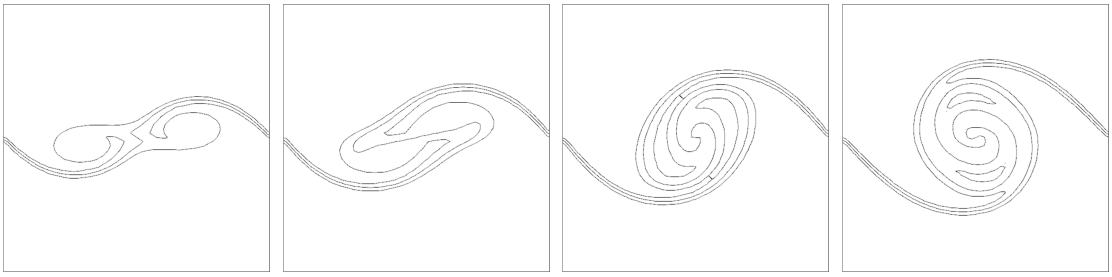

(a) t = 3s **(b)** t = 4s **(c)** t = 5s **(d)** t = 6s

Figure D.16: Contour lines of volume fraction 0.25 to 0.75 for the instability development of the two mode Kelvin–Helmholtz test case captured by compressible flow solver of ANSYS Fluent with explicit time stepping method for Mach number at 0.2 on grid resolution of 64×64

D.2.2 Mach number at 0.02

D.2.2.1 Grid resolution 24×24

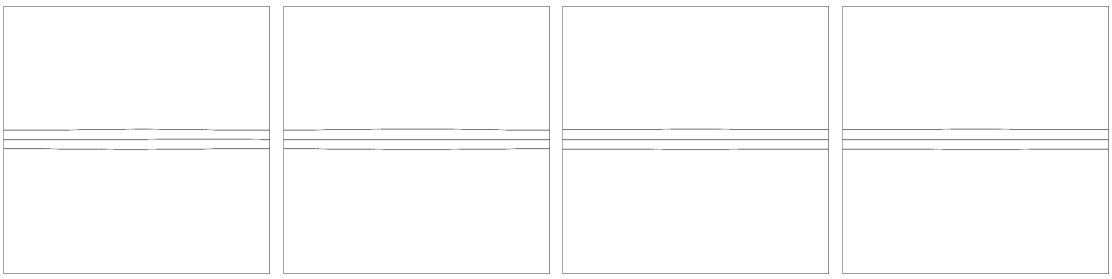

(a) t = 3s **(b)** t = 4s **(c)** t = 5s **(d)** t = 6s

Figure D.17: Contour lines of volume fraction 0.25 to 0.75 for the instability development of the two mode Kelvin–Helmholtz test case captured by compressible flow solver of ANSYS Fluent with explicit time stepping method for Mach number at 0.02 on grid resolution of 24×24

D.2.2.2 Grid resolution 32×32

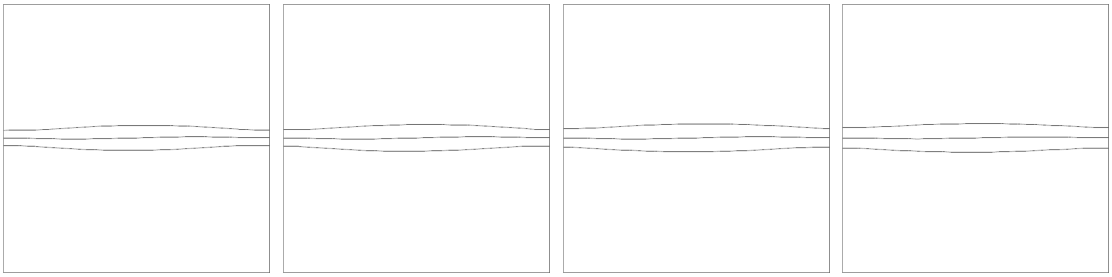

(a) t = 3s **(b)** t = 4s **(c)** t = 5s **(d)** t = 6s

Figure D.18: Contour lines of volume fraction 0.25 to 0.75 for the instability development of the two mode Kelvin–Helmholtz test case captured by compressible flow solver of ANSYS Fluent with explicit time stepping method for Mach number at 0.02 on grid resolution of 32×32

D.2.2.3 Grid resolution 48×48

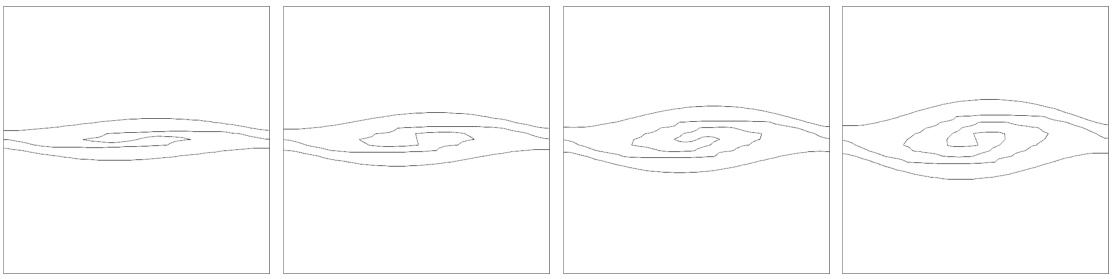

(a) t = 3s **(b)** t = 4s **(c)** t = 5s **(d)** t = 6s

Figure D.19: Contour lines of volume fraction 0.25 to 0.75 for the instability development of the two mode Kelvin–Helmholtz test case captured by compressible flow solver of ANSYS Fluent with explicit time stepping method for Mach number at 0.02 on grid resolution of 48×48

D.2.2.4 Grid resolution 64×64

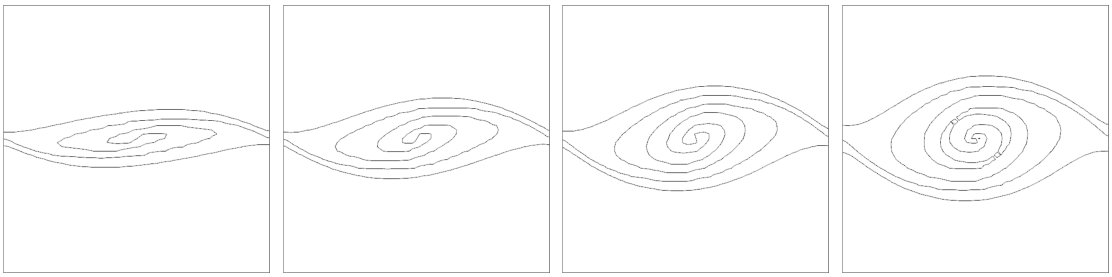

(a) t = 3s **(b)** t = 4s **(c)** t = 5s **(d)** t = 6s

Figure D.20: Contour lines of volume fraction 0.25 to 0.75 for the instability development of the two mode Kelvin–Helmholtz test case captured by compressible flow solver of ANSYS Fluent with explicit time stepping method for Mach number at 0.02 on grid resolution of 64×64

Appendix E

Vortex pairing - TRICLADE

E.1 5^{th} order wave propagation algorithm

The development of the Kelvin–Helmholtz instability captured on all grid resolutions, 24×24, 32×32, 48×48 and 64×64, for all Mach numbers, 0.2, 0.02 and 0.002, by 5^{th} order wave propagation algorithm are included in this section [13].

E.1.1 Mach number at 0.2

E.1.1.1 Grid resolution 24×24

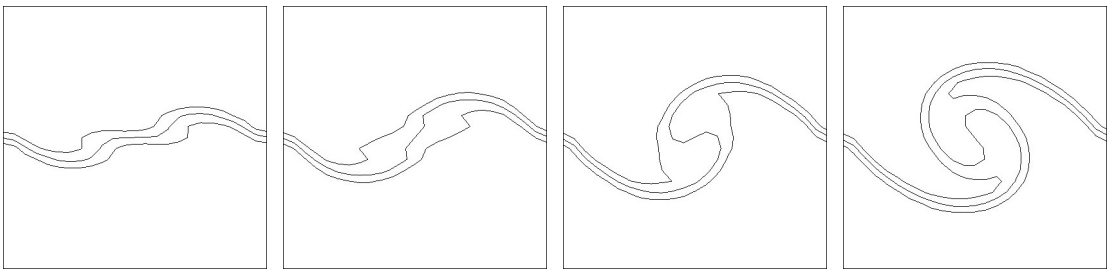

(a) t = 3s **(b)** t = 4s **(c)** t = 5s **(d)** t = 6s

Figure E.1: Contour lines of volume fraction 0.25 to 0.75 for Mach number at 0.2 using `TRICLADE` with WP5 scheme (5^{th} order time-space accuracy, and MP limitation) on grid resolution of 24×24 [13]

E.1.1.2 Grid resolution 32×32

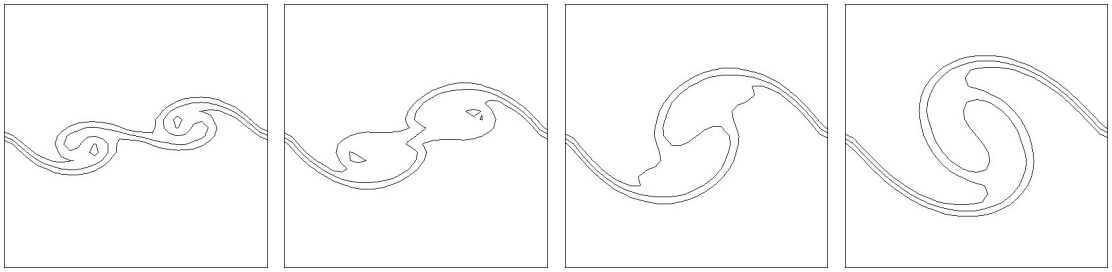

(a) t = 3s **(b)** t = 4s **(c)** t = 5s **(d)** t = 6s

Figure E.2: Contour lines of volume fraction 0.25 to 0.75 for Mach number at 0.2 using `TRICLADE` with WP5 scheme (5^{th} order time-space accuracy, and MP limitation) on grid resolution of 32×32 [13]

E.1.1.3 Grid resolution 48×48

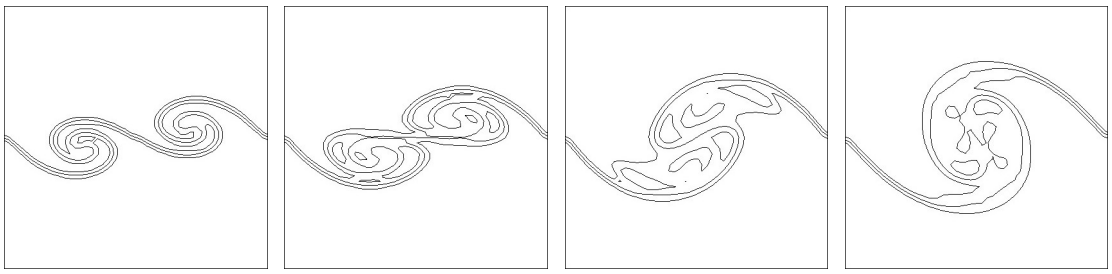

(a) t = 3s **(b)** t = 4s **(c)** t = 5s **(d)** t = 6s

Figure E.3: Contour lines of volume fraction 0.25 to 0.75 for Mach number at 0.2 using `TRICLADE` with WP5 scheme (5^{th} order time-space accuracy, and MP limitation) on grid resolution of 48×48 [13]

E.1.1.4 Grid resolution 64×64

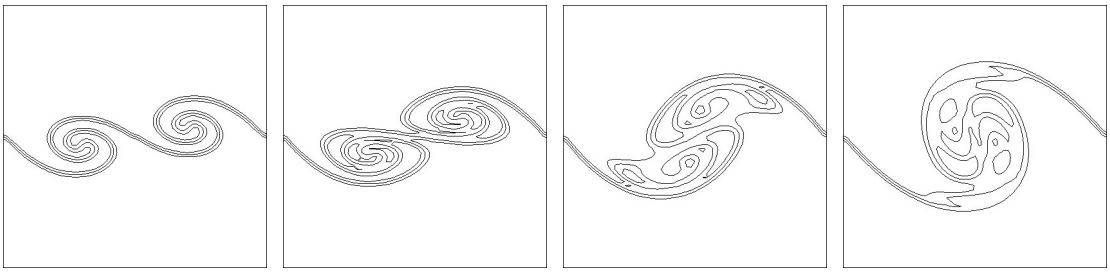

(a) t = 3s **(b)** t = 4s **(c)** t = 5s **(d)** t = 6s

Figure E.4: Contour lines of volume fraction 0.25 to 0.75 for Mach number at 0.2 using TRICLADE with WP5 scheme (5^{th} order time-space accuracy, and MP limitation) on grid resolution of 64×64 [13]

E.1.2 Mach number at 0.02

E.1.2.1 Grid resolution 24×24

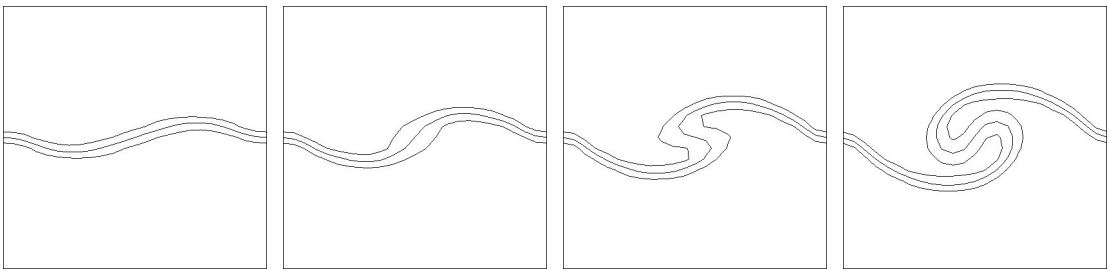

(a) t = 3s **(b)** t = 4s **(c)** t = 5s **(d)** t = 6s

Figure E.5: Contour lines of volume fraction 0.25 to 0.75 for Mach number at 0.02 using TRICLADE with WP5 scheme (5^{th} order time-space accuracy, and MP limitation) on grid resolution of 24×24 [13]

E.1.2.2 Grid resolution 32×32

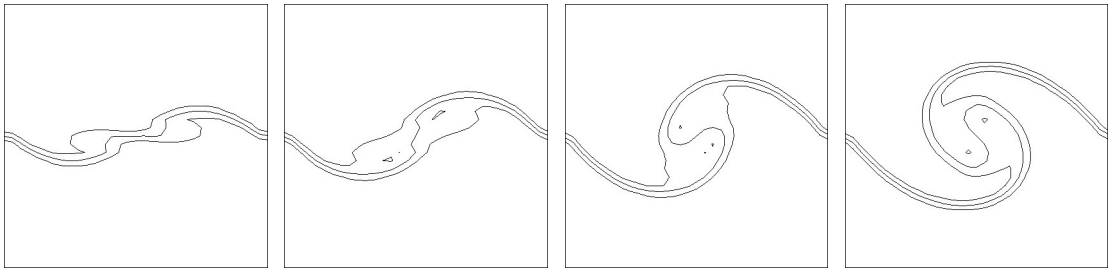

(a) t = 3s **(b)** t = 4s **(c)** t = 5s **(d)** t = 6s

Figure E.6: Contour lines of volume fraction 0.25 to 0.75 for Mach number at 0.02 using `TRICLADE` with WP5 scheme (5^{th} order time-space accuracy, and MP limitation) on grid resolution of 32×32 [13]

E.1.2.3 Grid resolution 48×48

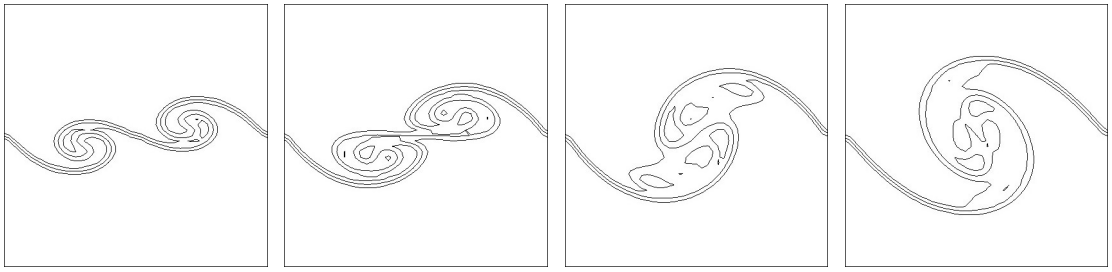

(a) t = 3s **(b)** t = 4s **(c)** t = 5s **(d)** t = 6s

Figure E.7: Contour lines of volume fraction 0.25 to 0.75 for Mach number at 0.02 using `TRICLADE` with WP5 scheme (5^{th} order time-space accuracy, and MP limitation) on grid resolution of 48×48 [13]

E.1.2.4 Grid resolution 64×64

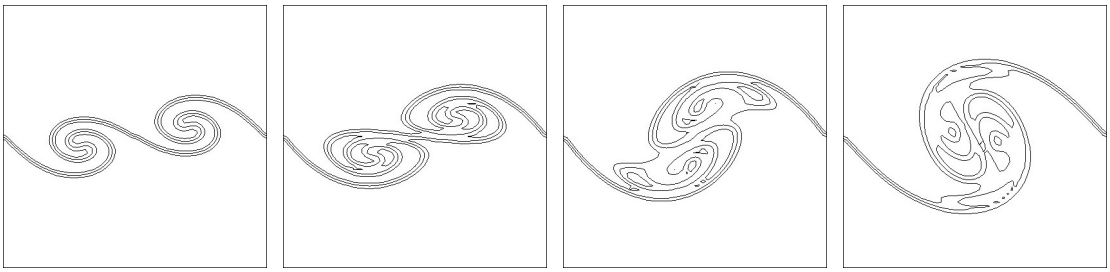

(a) t = 3s **(b)** t = 4s **(c)** t = 5s **(d)** t = 6s

Figure E.8: Contour lines of volume fraction 0.25 to 0.75 for Mach number at 0.02 using TRICLADE with WP5 scheme (5^{th} order time-space accuracy, and MP limitation) on grid resolution of 64×64 [13]

E.1.3 Mach number at 0.002

E.1.3.1 Grid resolution 24×24

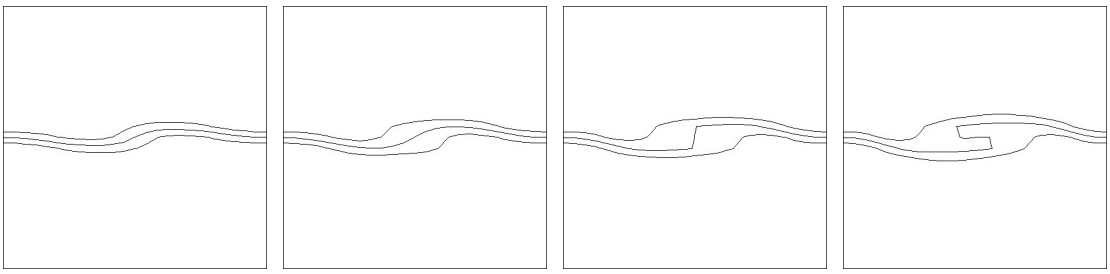

(a) t = 3s **(b)** t = 4s **(c)** t = 5s **(d)** t = 6s

Figure E.9: Contour lines of volume fraction 0.25 to 0.75 for Mach number at 0.002 using TRICLADE with WP5 scheme (5^{th} order time-space accuracy, and MP limitation) on grid resolution of 24×24 [13]

E.1.3.2 Grid resolution 32×32

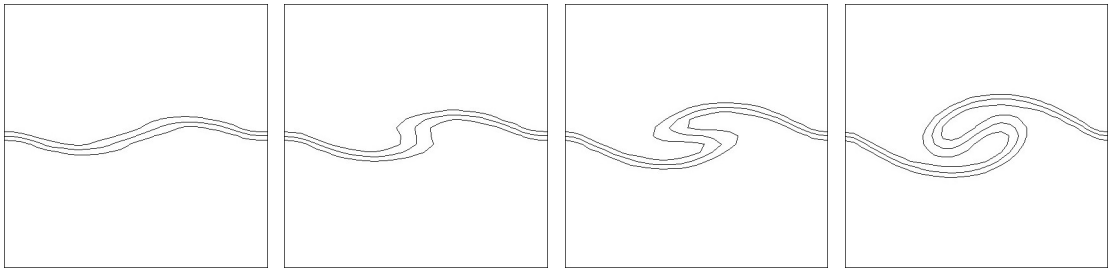

(a) t = 3s **(b)** t = 4s **(c)** t = 5s **(d)** t = 6s

Figure E.10: Contour lines of volume fraction 0.25 to 0.75 for Mach number at 0.002 using `TRICLADE` with WP5 scheme (5^{th} order time-space accuracy, and MP limitation) on grid resolution of 32×32 [13]

E.1.3.3 Grid resolution 48×48

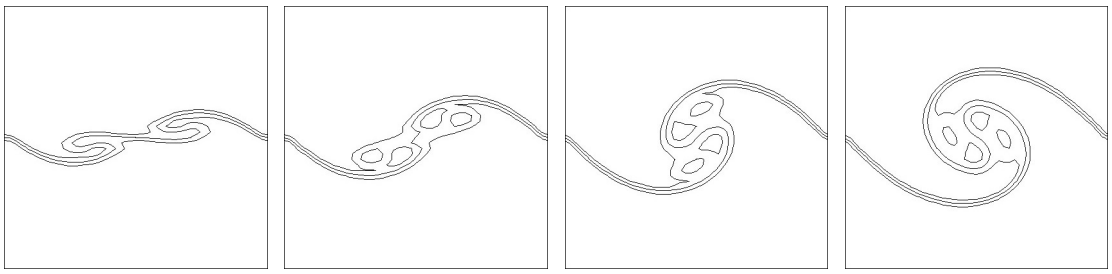

(a) t = 3s **(b)** t = 4s **(c)** t = 5s **(d)** t = 6s

Figure E.11: Contour lines of volume fraction 0.25 to 0.75 for Mach number at 0.002 using `TRICLADE` with WP5 scheme (5^{th} order time-space accuracy, and MP limitation) on grid resolution of 48×48 [13]

E.1.3.4 Grid resolution 64×64

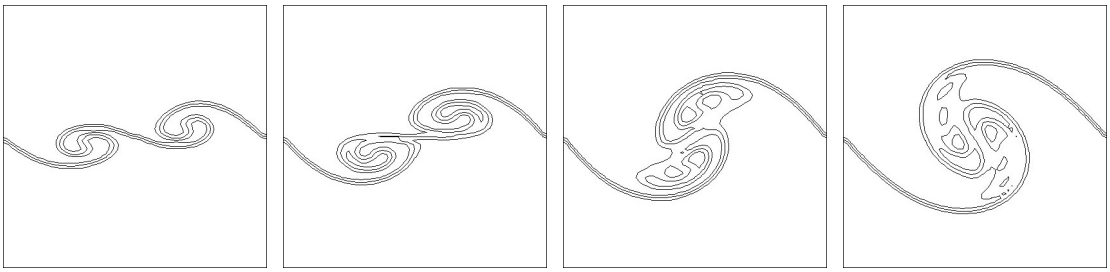

(a) t = 3s **(b)** t = 4s **(c)** t = 5s **(d)** t = 6s

Figure E.12: Contour lines of volume fraction 0.25 to 0.75 for Mach number at 0.002 using `TRICLADE` with WP5 scheme (5^{th} order time-space accuracy, and MP limitation) on grid resolution of 64×64 [13]

Appendix F

Vortex pairing - TRICLADE

F.1 5^{th} order Godunov method with SLAU numerical flux

The development of the Kelvin–Helmholtz instability captured on all grid resolutions, 24×24, 32×32, 48×48 and 64×64, for all Mach numbers, 0.2, 0.02 and 0.002, by 5^{th} order Godunov method with SLAU numerical flux are included in this section [13].

F.1.1 Mach number at 0.2

F.1.1.1 Grid resolution 24×24

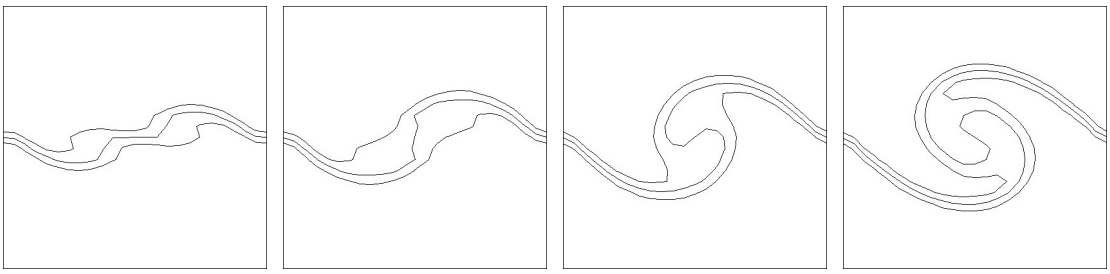

(a) t = 3s **(b)** t = 4s **(c)** t = 5s **(d)** t = 6s

Figure F.1: Contour lines of volume fraction 0.25 to 0.75 for Mach number at 0.2 using `TRICLADE` with WP5 scheme (5^{th} order time-space accuracy, and MP limitation) on grid resolution of 24×24 [13]

F.1.1.2 Grid resolution 32×32

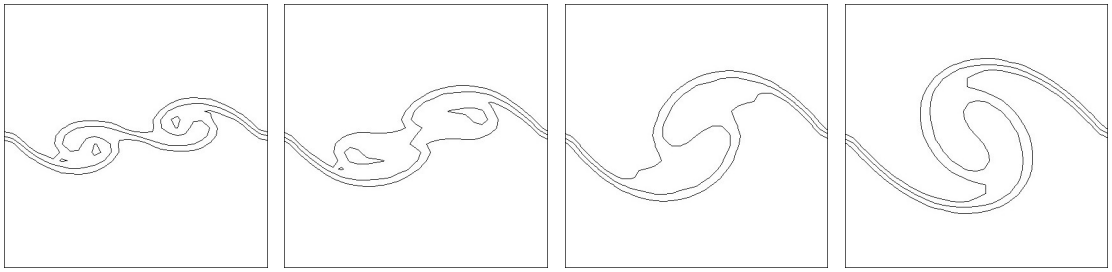

(a) t = 3s **(b)** t = 4s **(c)** t = 5s **(d)** t = 6s

Figure F.2: Contour lines of volume fraction 0.25 to 0.75 for Mach number at 0.2 using TRICLADE with WP5 scheme (5^{th} order time-space accuracy, and MP limitation) on grid resolution of 32×32 [13]

F.1.1.3 Grid resolution 48×48

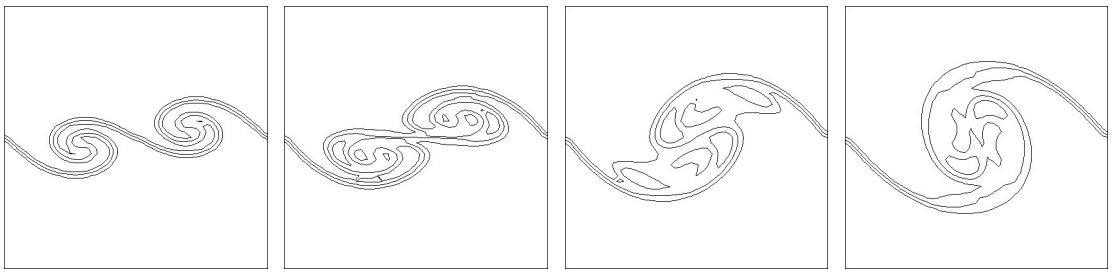

(a) t = 3s **(b)** t = 4s **(c)** t = 5s **(d)** t = 6s

Figure F.3: Contour lines of volume fraction 0.25 to 0.75 for Mach number at 0.2 using TRICLADE with WP5 scheme (5^{th} order time-space accuracy, and MP limitation) on grid resolution of 48×48 [13]

F.1.1.4 Grid resolution 64×64

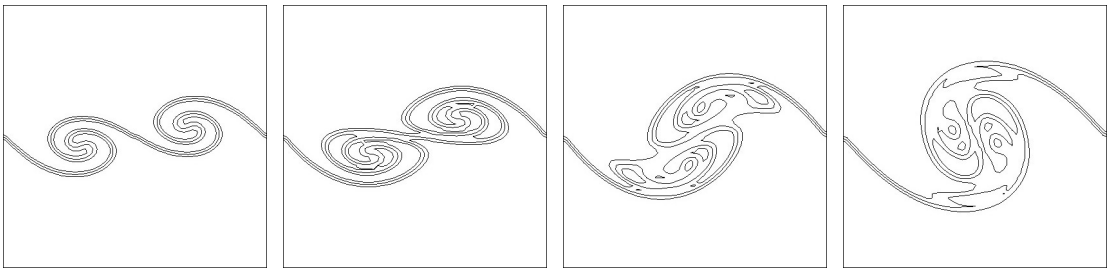

(a) t = 3s **(b)** t = 4s **(c)** t = 5s **(d)** t = 6s

Figure F.4: Contour lines of volume fraction 0.25 to 0.75 for Mach number at 0.2 using TRICLADE with WP5 scheme (5^{th} order time-space accuracy, and MP limitation) on grid resolution of 64×64 [13]

F.1.2 Mach number at 0.02

F.1.2.1 Grid resolution 24×24

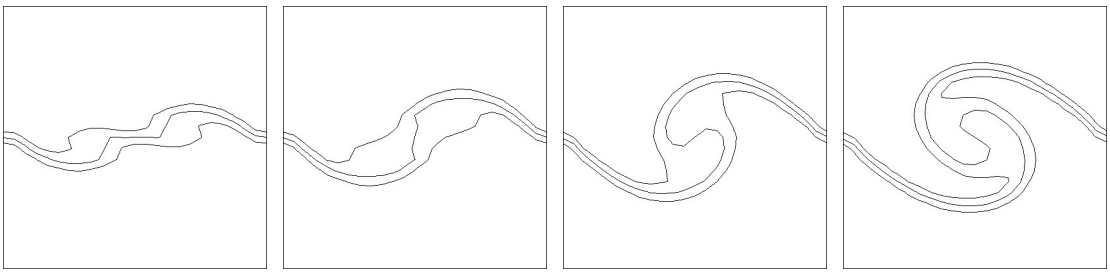

(a) t = 3s **(b)** t = 4s **(c)** t = 5s **(d)** t = 6s

Figure F.5: Contour lines of volume fraction 0.25 to 0.75 for Mach number at 0.02 using TRICLADE with WP5 scheme (5^{th} order time-space accuracy, and MP limitation) on grid resolution of 24×24 [13]

F.1.2.2 Grid resolution 32×32

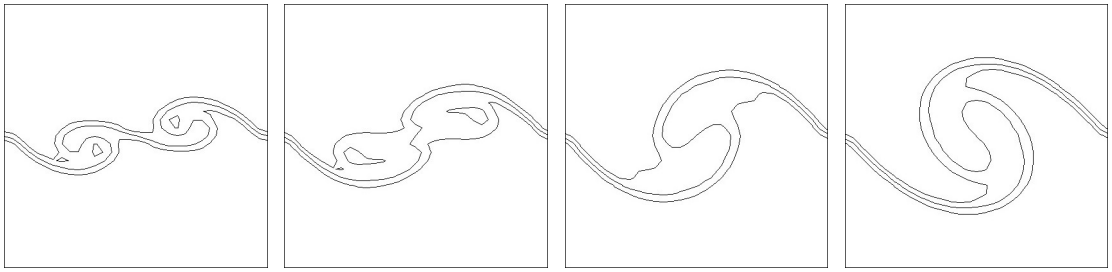

(a) t = 3s **(b)** t = 4s **(c)** t = 5s **(d)** t = 6s

Figure F.6: Contour lines of volume fraction 0.25 to 0.75 for Mach number at 0.02 using TRICLADE with WP5 scheme (5^{th} order time-space accuracy, and MP limitation) on grid resolution of 32×32 [13]

F.1.2.3 Grid resolution 48×48

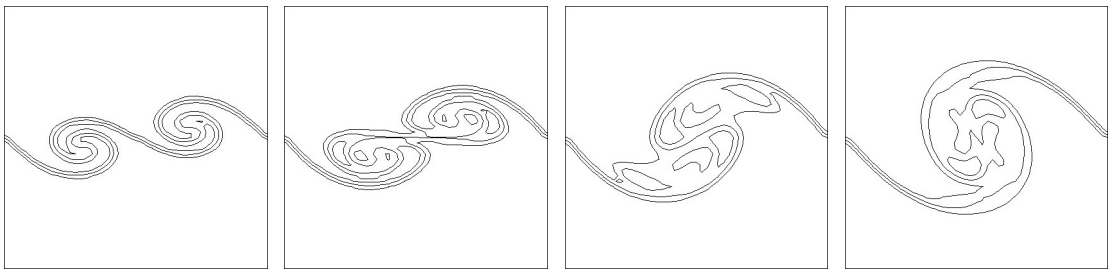

(a) t = 3s **(b)** t = 4s **(c)** t = 5s **(d)** t = 6s

Figure F.7: Contour lines of volume fraction 0.25 to 0.75 for Mach number at 0.02 using TRICLADE with WP5 scheme (5^{th} order time-space accuracy, and MP limitation) on grid resolution of 48×48 [13]

F.1.2.4 Grid resolution 64×64

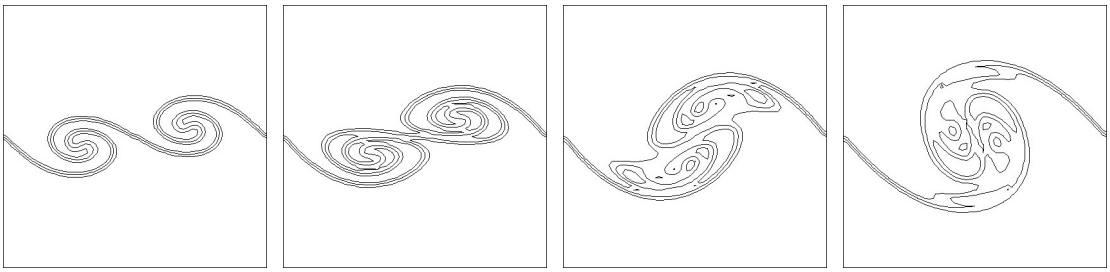

(a) t = 3s **(b)** t = 4s **(c)** t = 5s **(d)** t = 6s

Figure F.8: Contour lines of volume fraction 0.25 to 0.75 for Mach number at 0.02 using TRICLADE with WP5 scheme (5^{th} order time-space accuracy, and MP limitation) on grid resolution of 64×64 [13]

F.1.3 Mach number at 0.002

F.1.3.1 Grid resolution 24×24

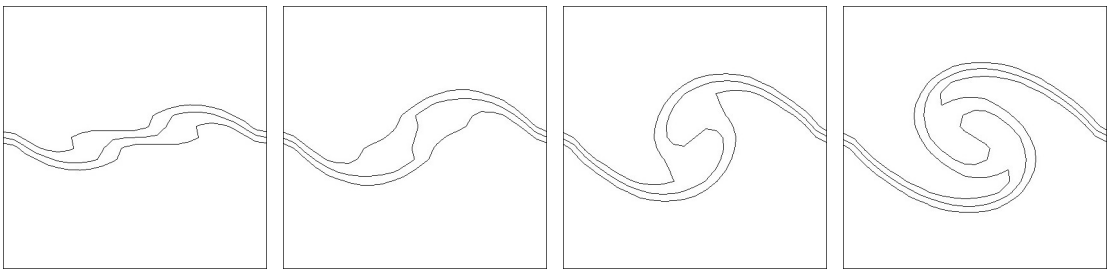

(a) t = 3s **(b)** t = 4s **(c)** t = 5s **(d)** t = 6s

Figure F.9: Contour lines of volume fraction 0.25 to 0.75 for Mach number at 0.002 using TRICLADE with WP5 scheme (5^{th} order time-space accuracy, and MP limitation) on grid resolution of 24×24 [13]

F.1.3.2 Grid resolution 32×32

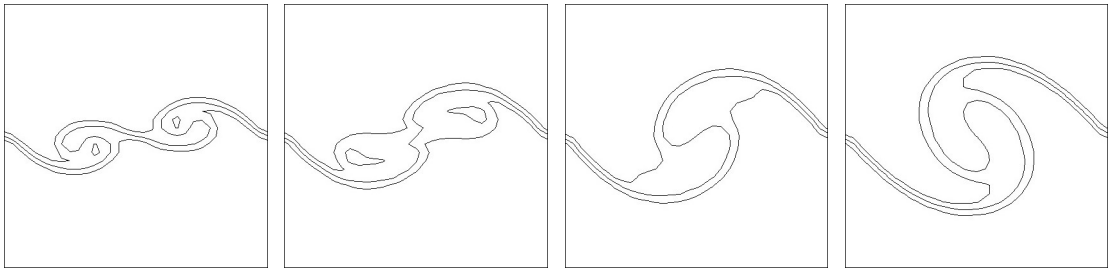

(a) t = 3s **(b)** t = 4s **(c)** t = 5s **(d)** t = 6s

Figure F.10: Contour lines of volume fraction 0.25 to 0.75 for Mach number at 0.002 using `TRICLADE` with WP5 scheme (5^{th} order time-space accuracy, and MP limitation) on grid resolution of 32×32 [13]

F.1.3.3 Grid resolution 48×48

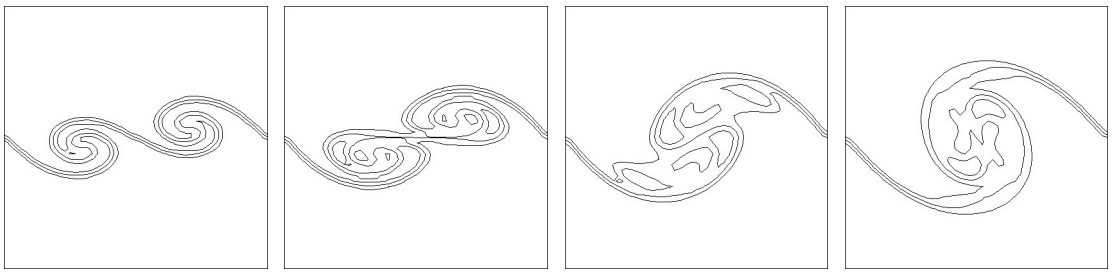

(a) t = 3s **(b)** t = 4s **(c)** t = 5s **(d)** t = 6s

Figure F.11: Contour lines of volume fraction 0.25 to 0.75 for Mach number at 0.002 using `TRICLADE` with WP5 scheme (5^{th} order time-space accuracy, and MP limitation) on grid resolution of 48×48 [13]

F.1.3.4 Grid resolution 64×64

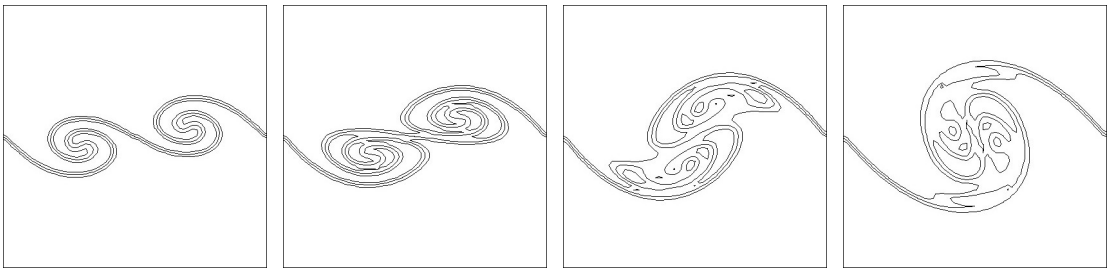

(a) t = 3s **(b)** t = 4s **(c)** t = 5s **(d)** t = 6s

Figure F.12: Contour lines of volume fraction 0.25 to 0.75 for Mach number at 0.002 using `TRICLADE` with WP5 scheme (5^{th} order time-space accuracy, and MP limitation) on grid resolution of 64×64 [13]